Histamine dehydrogenase from *Rhizobium sp. 4-9*: a potential enzyme for histamine biosensing applications

By

Priyanka Goyal

Submitted to the graduate degree program in Department of Molecular Biosciences and the Graduate Faculty of the University of Kansas in partial fulfillment of the requirements for the degree of Doctor of Philosophy.

Chair: Roberto N. De Guzman, Ph.D.
for Mark L. Richter,[+] Ph.D.

Peter A. Petillo, Ph.D.

George S. Wilson, Ph.D.

Krzysztof Kuczera, Ph.D.

Erik Holmstrom, Ph.D.

Cindy L. Berrie, Ph.D.

Date Defended: 28 April 2022

The dissertation committee for Priyanka Goyal certifies that this is the approved version of the following dissertation:

Histamine dehydrogenase from *Rhizobium sp. 4-9*: a potential enzyme for histamine biosensing applications

Chair: Roberto N. De Guzman, Ph.D.

for Mark L. Richter,[+] Ph.D.

Date Approved: May 6 2022

Abstract

Dehydrogenases are enzymes that consist of a flavin cofactor in their catalytic unit and a heme or an Fe_4S_4 cluster in their electron transfer subunit, thereby having the ability to undergo direct electron transfer processes. A significant advantage of using dehydrogenases over oxidases for enzyme-based biosensing applications is the ability to eliminate oxygen dependence. The goal of this dissertation was to investigate one such flavin dependent dehydrogenase (FDD) enzyme, the histamine dehydrogenase from *Rhizobium sp. 4-9* (HaDHR) and determine the protein engineering criteria required of a dehydrogenase enzyme for use in *in vivo* biosensing applications. HaDHR belongs to a small family of dehydrogenases that contains a covalently attached FMN and an Fe_4S_4 as the redox cofactors. HaDHR can convert histamine to imidazole acetaldehyde and ammonia with a release of two electrons and is the only member of this family that does not show substrate inhibition, making HaDHR the best candidate for use in *in vivo* biosensing applications. The crystal structure of HaDHR at a resolution of 2.1 Å was determined, which facilitated elucidation of the internal electron transfer pathway from the active site to the protein's surface. An artificial electron mediator Fc^+ was covalently attached proximal to the exit point of the electron transfer pathway. We demonstrated that even in the absence of any other mediator, an Fc-modified HaDHR could deliver electrons from the enzyme to an electrode surface in the presence of histamine in a dose-dependent manner. We engineered HaDHR with noble metal affinity peptides to orient the enzyme on an electrode surface. Additionally, structural comparisons between HaDHR and other family members was undertaken to probe the origins of substrate inhibition. Together, these results provided a proof of concept that HaDHR is suitable for use in the fabrication of Gen 2.5 and Gen 3 biosensors, thereby contributing significantly to this rapidly evolving field.

Acknowledgments

PhD is a journey, and no two graduate student ever has a similar one. When I first came to USA six years ago, I was excited and nervous at the same time, as I was settling in to embark upon this new journey. The amount of support, help and love I got from those around me in my entire journey is what I had not anticipated before. Foremost among them, was my supervisor, Prof. Mark L. Richter. He had been an amazing mentor, and I am grateful for his patience, optimism, understanding, and constant support in my scientific endeavors. Unfortunately, I lost him during the first wave of COVID-19 and as I am almost at the end of my PhD journey, I dearly miss him around.

I would also like to thank the members of my PhD advisory committee, Prof. Roberto De Guzman for becoming my interim mentor, Dr. Peter A. Petillo (Design-Zyme, LLC) for stepping in and helping me with my further research progress and becoming the corresponding author for my publications. Prof. George S. Wilson for all his valuable inputs in my research and for answering all my electrochemistry related questions. Prof. Krzysztof Kuczera for always supporting me and being the chair of my orals committee. Assoc. Prof. Cindy Berrie for helping me with the AFM studies and always providing valuable inputs. Asst. Prof. Erik Holmstrom for becoming a part of my committee and giving me valuable suggestions.

The work performed in the past six years wouldn't have been possible without the support of my collaborators Dr. Scott Lovell (X-ray crystallopgraphy), Dr. Candan Tamerler (metal affinity peptides) and Dr. Steve Seibold (computational studies). I would like to express my deep gratitude towards my lab members Dr. Dwight Deay, Dr. Kim Colvert, Alex Bowman and Parker Sperstad and my two wonderful undergraduates Zachary Shaw and Halle Arnold for providing collaborative and fun environment in the lab.

A big thank you to all the strangers whom I met in my PhD journey who have truly become my family. My friends in Lawrence helped me in numerous ways and I am really grateful to each one of them for being part of my journey and giving me such wonderful memories to cherish for lifelong.

I am deeply grateful to my parents Mahesh Goyal and Vinita Goyal, my in-laws Col. Bappaditya Dhar and Sanchita Dhar, my aunt Sita Goyal and my entire family for loving me always, believing in my dreams and always cheering and encouraging me to perform good.

Lastly, I would like to thank Rik Dhar for being an extraordinary life-partner. I am grateful to him for always supporting me, believing in my dreams and aspiring me to become a better human.

Six years is a long journey and it is hard to condense all the wonderful moments together but each and every one of you have helped make my PhD journey special and for that I am immensely grateful.

Dedication

This dissertation is dedicated to my late graduate mentor, Dr. Mark L. Richter, and my late uncle Naresh Goyal who passed away from complications of COVID-19 during my doctoral studies.

They will be dearly missed.

This dissertation is also dedicated to all the people who have supported me throughout my education. Thank you for making me see this adventure through to the end.

Table of Contents

List of Figures

List of Tables

List of Abbreviations

ADP: Adenosine Diphosphate

Ag/AgCl: Silver Silver Chloride Electrode

ATP: Adenosine Triphosphate

Au: Gold

cAuBP: Cyclic gold binding peptide

DCIP: Dichlorophenolindophenol

DET: Direct Electron Transfer

DHAP: Dihydroxyacetophenone

DLS: Dynamic Light Scattering

DMADH: Dimethylamine dehydrogenase

DTT: Dithiothreitol

EDTA: Ethylenediaminetetraacetic acid

EPR: Electron Paramagnetic Resonance

ETFDH: Electron transfer flavoprotein

Fc: Ferrocene

Fc^{+}-DM: Ferricenium dimethanol

$Fc^{+}PF_6^{-}$: Ferricenium hexafluorophosphate

Fc-DM: Ferrocenedimethanol

FDD: Flavin dependent dehydrogenase

Fe_4S_4: Iron sulfur cluster

FMN: Flavin mononucleotide

HaDHN: Histamine dehydrogenase from Nocardioides simplex

HaDHR: Histamine dehydrogenase from Rhizobium sp. 4-9

HPLC: High Performance Liquid Chromatography

IUPAC: International Union of Pure and Applied Chemistry

kDa: kilodalton

LB: Luria Bertoni

MALDI: Matrix Assisted Laser Desorption/Ionization

MET: Mediated electron transfer

MOE: Molecular Operating Environment

ND: Not determined

NiNTA: Nickel-charged nitriloacetic acid

PDB: Protein Data Bank

PEG: Polyethylene glycol

PES: Phenazine ethosulfate

PME: Particle mesh Ewald

PMS: Phenazine methosulfate

Pt: Platinum

PtBP: Platinum binding peptide

QCM: Quartz Crystal Microbalance

RCSB: Resource for chemical, biochemical, and structural explorations of large and small biomolecules

RMSD: Root-mean-square deviation

SDS-PAGE: Sodium dodecyl sulfate-polyacrylamide gel electrophoresis

SPR: Surface Plasmon Resonance

TEV: Tobacco Etch Virus

TFA: Trifluoroacetic acid

TMADH: Trimethylamine Dehydrogenase

UV: Ultraviolet

Chapter 1. Introduction

Histamine is an essential biogenic amine that acts as a chemical neurotransmitter in the brain, mediates allergic reactions, and is a key immune signaling molecule (1,2). Histamine is involved in various brain functions (1,3), and through earlier studies in animal models and postmortem studies in humans it has been shown that histamine concentration plays a prominent role in several neurological disorders including sleep-wake disorders, disorders of mood and cognition (schizophrenia, depression, Alzheimer's disease), movement disorders (Parkinson's disease), epilepsy, eating disorders, pain, and addiction (4-9). At present, microdialysis techniques exist that are coupled to high performance liquid chromatography (HPLC) as well as fluorescence, optical density, or electrochemical detection systems help in monitoring brain neurotransmitters. Data obtained help in studying biomarkers and their relationship to diseases. However, the major drawback of these systems is the poor spatial and temporal resolution (10).

Although histamine concentration regulation is so important in the brain, at present there is no biosensor, a specific device or method by which one can accurately measure the levels of histamine in the brain, either as a single point measurement or in real time on a continuous basis. Amperometric biosensors are the most prominent technology available currently to study the fluctuations in the levels of neurotransmitters and neuromodulators that are related to many neurological diseases in the brain (11,12). These biosensors can be implanted directly into the brain and thus can monitor the concentrations of neuroactive substances in real time (13). Such a device would help in early diagnosis of neurological and psychiatric disorders, which after successful testing in animal models, will ultimately aid human patients in health condition management for effective treatment and potential disease prevention. These biosensors can be used in rodents for drug discovery and in cases where biological fluids can be obtained non-invasively

or semi-invasively. While some applications of a histamine biosensor might be employed by the patient themselves, many other applications are possible in urgent care settings where the histamine biosensor is installed and monitored by medical professionals, such as during brain injury or stroke (14-16). A histamine biosensor for use by first responders and in critical care situations may also help improve acute patient morbidity and mortality (15). While long-term biosensor implantation is likely to be too invasive for chronic applications, subcutaneous implantation may be possible to monitor systemic changes in histamine concentration that may reflect underlying brain pathologies.

Biosensors are functional analytical devices that incorporate a biological recognition element, usually an enzyme, to analyze specific quantitative information from complex mixtures such as blood and tissue (17). These devices can harness exquisite sensitivity and specificity coupled with high temporal and spatial resolution (18-21). In the past two decades, growth in the biosensor field has been phenomenal, such that, in last year alone, about 4500 papers on biosensors were published discussing their wide range of functional modalities. Despite their potential use and effectiveness in a wide range of applications, development of biosensors that can continuously in real time monitor analytes *in vivo* for extended, long periods of time is a challenging task and at the present only glucose biosensors are routinely used in humans to monitor glucose levels in real time (22-24).

Enzymes are the most critical component of a biosensor design. The performance of a biosensor device relies ultimately on the suitable activity, selectivity, reproducibility, reliability, and long-term stability of the enzyme for *in vivo* applications. Currently, many biosensors that are capable of real-time measurement of analytes are oxidase enzyme-based amperometric biosensors (25). Other classes of biosensors that have been used to probe brain function are carbon fiber-based

probes that are selective for some neurotransmitters (26-28). Oxidase enzymes have been used extensively in the development and commercialization of biosensors as their family members are known to process a variety of analytes that are important for human health monitoring (21,22). The most widespread used oxidase enzyme is glucose oxidase and due to its high stability and activity profile, is often referred to as "an ideal enzyme" (22). At present there are two FDA approved glucose oxidase-based biosensors that are used for monitoring glucose continuously. One can monitor for 14 days and the other for 10 days continuously and both claim to come pre-calibrated. However, this is often not the case and despite such widespread use they are still not stable enough for long term *in vivo* studies. The problem is not always due to the stability of the enzyme but can also be due to the immune response to the implanted sensor (15,29).

When discussing a peroxide producing enzyme suitable for use in biosensor fabrication, there are two critical parameters: k_{cat} and K_M. The catalytic efficiency of the enzyme is designated as k_{cat}. K_M describes the point at which the reaction velocity of the enzyme starts to plateau and directly influences the *in vivo* linearity of the biosensor. Because the maximum concentration of enzyme that can be practically immobilized on a given biosensor is usually limited by the geometry of the transduction element, k_{cat} is the measure that most directly relates to final sensitivity of the completed biosensor.

Oxidase enzymes require oxygen to function and depending upon the *in vivo* environment the availability of oxygen may directly affect K_M (30). In addition, for biosensors based on an oxidase enzyme the problems of enzyme activity, stability, and availability often dictate the useable lifetime of a biosensor. The activity and stability are usually associated with cofactor residence: how long the FAD or FMN cofactors remain resident inside the enzyme. Additionally, there is a problem of the peroxide capture by the transduction element which is typically very inefficient.

Some studies have determined that over 90% of the peroxide generated by the oxidase enzyme may be lost to the environment and never sensed by the transduction element (31). This phenomenon is partially related to the thickness of the enzyme layer in a biosensor, the importance of peroxide loss is also dependent upon the analyte being measured and the activity of the enzyme (32). For example, peroxide loss may not be as relevant for glucose biosensors because the glucose concentration range is mM, and sufficient signal exists to make reproducible measurements. For sensors measuring analytes at the μM range, for example glutamate, peroxide loss may be more relevant (32).

Dehydrogenases, unlike oxidases, have the potential to directly transfer electrons from the enzyme directly to the transduction element of a biosensor (33). In the absence of direct electron transfer (DET) dehydrogenases can be used in conjunction with artificial mediators, such as, ferrocenes, osmium salts, variety of dyes, quinones and ferri/ferrocyanides (34). Unlike oxidases, dehydrogenases can undergo DET from the enzyme or through a mediator to the electrode surface (35,36). This requires careful attention to the electron transfer pathway through the enzyme from the flavin cofactor to the electrode surface. Application of a flavin dependent dehydrogenase (FDD) enzyme is often limited because the redox catalytic center is buried within the protein structure in combination with the lack of an electron transfer pathway to the electrode surface (37-39). Several of these dehydrogenases often harbor an additional heme prosthetic group, such as a cytochrome domain which acts as a 'built in mediator' that can connect to the flavin domain to undergo DET with electrodes (40,41).

A significant advantage of dehydrogenases over oxidases is that the enzyme response is not dependent on oxygen and can be used for repeated measurements where the oxygen concentration is variable. Use of dehydrogenases would make possible the construction of biosensor arrays that

monitor a range of analytes simultaneously. With oxidases, array construction is difficult, if not impossible, because of the worry about different sensing elements "stealing oxygen" from adjacent elements. For example, when measuring a particular analyte in the brain, a response to a stimulus measured using an oxidase enzyme can simultaneously change the oxygen level as well as the analyte level around the sensing element, which may affect subsequent measurements (42-44).

The diffusion of peroxide away from the biosensor transduction element is not a problem for sensors based on dehydrogenases. If fast response (sub-second) is required, then all the enzyme layers on the sensor surface must be thin. Further, achieving good spatial resolution requires small sensors, namely 10 μm or less. For the purposes of *in vivo* histamine sensing, systemic histamine concentrations range from 4 nM - 240 μM (45) and brain histamine concentrations also fall within this range (46). The concentration of histamine in the brain is also dependent upon the area being probed and different regions of the brain is known to have different concentrations, however, there is a reservoir of histamine in the brain stored in mast cells which may not contribute to any snapshot measure of a histamine concentration (1,47). Regardless, biorecognition elements based on dehydrogenases could offer improved performance and better sensitivity compared to the corresponding oxidase. This is especially true if the dehydrogenase could be leveraged for DET.

Based on oxidase enzyme-based amperometric biosensor studies, efforts have been made earlier to design a biosensor to monitor histamine levels in the brain in real-time by using a histamine oxidase enzyme from *Arthrobacter globiformis* (48). This enzyme was found to be non-specific for histamine and more specific for dopamine or tyramine. Since then, no known histamine oxidase has been identified that is highly specific for histamine. However, there is a histamine dehydrogenase (HaDH) enzyme from two different bacterial species that have been identified. Histamine dehydrogenase from Nocardioides simplex (HaDHN) and histamine dehydrogenase

from Rhizobium sp. 4-9 (HaDHR) (41,42). Studies on HaDHN and HaDHR have shown their successful biosensing application in the food industry (49-53).

In this dissertation, we present data on one such FDD enzyme HaDHR, a histamine dehydrogenase from *Rhizobium sp. 4-9* that is highly specific for histamine and has the appropriate catalytic properties to support its use in the fabrication of a DET type biosensor for use in *in vivo* histamine biosensing applications. HaDHR belongs to a small family of covalently bound 6-S-cysteinyl-FMN enzymes that has only been identified so far in four different bacterial enzymes as shown in Table 1-1 (54-58).

Table 1-1: 6-S-cyteinyl-FMN covalent linkage identified in bacterial enzymes

Enzyme	Source
Histamine Dehydrogenase (HaDHR)	*Rhizobium sp.* 4-9 (54)
Histamine Dehydrogenase (HaDHN)	*Nocardioides simplex* (55)
Trimethylamine dehydrogenase (TMADH)	*Bacterium sp*. W_3A_41 (56)
Dimethylamine dehydrogenase (DMADH)	*Hyphomicrobium X* (58)

Both HaDHR and HaDHN enzyme catalyze the oxidative deamination of histamine to form imidazole acetaldehyde and ammonia (54,59). Each enzyme comprises a Fe_4S_4 iron-sulfur center as a redox active cofactor and an ADP in each subunit of the homodimer. Although both enzymes catalyze histamine, the key difference between the two enzymes is that HaDHR is highly specific for histamine and does not show substrate inhibition at high concentrations of histamine (54). HaDHN, however, shows reasonable selectivity towards histamine with respect to other biogenic amines such as agmatine and putrescine (60) but also shows substrate inhibition (61). HaDHN shows 55% sequence homology with HaDHR and is the best characterized enzyme of the two. Interestingly, both HaDHR and HaDHN enzymes have been used to develop enzyme assays (52,62,63) or for engineering bio-electrochemical sensors (49,53) for detecting histamine in *in vitro* diagnostic methods. However, no attempts have been made yet to engineer these enzymes

for *in vivo* histamine biosensing applications. Since, HaDHR shows higher substrate specificity for histamine and no substrate inhibition and is the least characterized enzyme, this dissertation is focused on understanding the structural and functional aspects of HaDHR, comparing it with the other histamine metabolizing dehydrogenase enzyme HaDHN. Molecular design is then used to optimize DET for *in-vivo* biosensing applications.

In Chapter 2 of this dissertation, we introduce the crystal structure of HaDHR solved at a resolution of 2.1Å (Figure 1-1A). Guided by this 3D-model and its comparison with other dehydrogenases in the family, we identified and mutated several amino acid residues to establish the electron transfer pathway from the Fe_4S_4 cluster to the enzyme surface. We identified Ala437 to be the key surface residue that terminates the electron transfer pathway from the Fe_4S_4 cluster to the surface of HaDHR. We then created a Ser436Cys mutant proximal to Ala437, to which a ferricenium ion (Fc^+) was tethered via standard maleimide chemistry (Figure 1-1B). Using standard electrochemical techniques, we successfully showed that in solution, the tethered Fc^+ accepted electrons from HaDHR when titrated with histamine (Figure 1-2). This study facilitated understanding of the possible electron transfer pathway through the molecule based on the crystal structure and enabled us to propose a bioengineering design for a mediated electron transfer (MET) type biosensor.

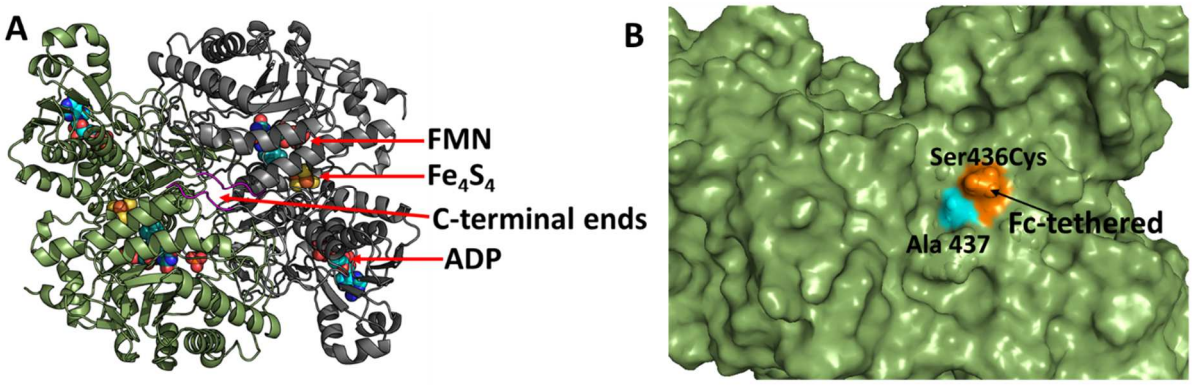

Figure 1-1 Crystal structure of HaDHR, RCSB accession number 6DE6
(A) Crystal structure of HaDHR solved at 2.1 Å resolution, (B) Ala437 (highlighted in cyan) key surface residue identified that exits electron from the HaDHR surface, Ser436Cys (highlighted in orange) mutant created to tether ferrocene for mediated electron transfer studies.

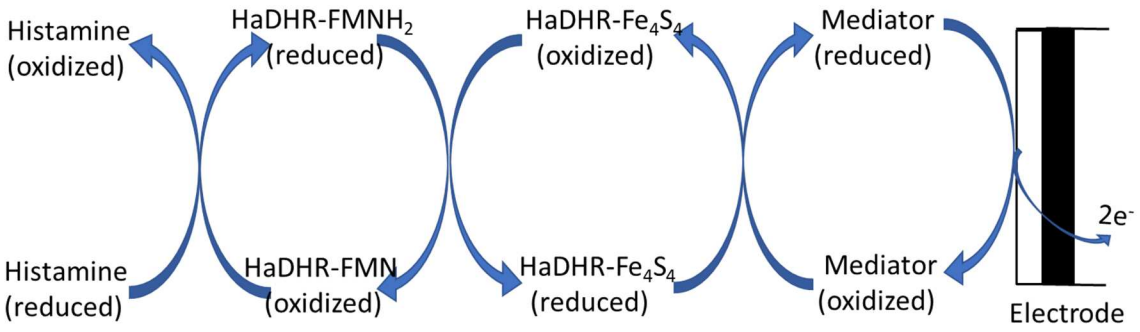

Figure 1-2 Schematic reaction scheme of the HaDHR enzyme system
This schematic presents the underlying chemistry of histamine oxidation by HaDHR that is explored in this dissertation. Histamine in the reduced state interacts with the oxidized form of HaDHR resulting in oxidation of histamine and reduction of the HaDHR-FMN cofactor. Electrons are then internally transferred from FMN to Fe_4S_4 and then to the surface of the protein upon oxidation of the Fe_4S_4 center. Electrons on the surface of the protein can interact with mediators, natural or artificial, which in turn can interact with an electrode to generate an electrochemical signal corresponding to the histamine reduction.

In Chapter 3 of this dissertation, we present detailed mechanistic studies of HaDHR and demonstrate that the enzyme does not show any substrate inhibition that can limit its use in biosensor fabrication. HaDHR is compared structurally and mechanistically to other members of its enzyme family, all of which show substrate inhibition. We suggest a molecular-based model for the absence of substrate inhibition in HaDHR as compared to the other members of the family, including HaDHN its closest homolog. Electron Paramagnetic Resonance (EPR) and stopped-flow measurements, suggested that a cause of inhibition was the binding of histamine to the flavin semiquinone in HaDHN (64). Comparison of the HaDHR and HaDHN active sites led to the hypothesis that substrate inhibition of HaDHN can be explained by the difference in orientation of a single aromatic residue (Phe176 in HaDHR; Tyr181 in HaDHN). A double mutant of HaDHR, F176Y/F131D, designed to mimic the HaDHN active site, resulted in ~50% reduction in k_{cat}. Based upon our analysis of the docking studies, HaDHR is found to be better poised to support hydride transfer from the histamine substrate, but the overall rate of electron transfer may be better optimized in HaDHN. This study enabled us to understand the structural mechanism of substrate inhibition in HaDHN by comparing it with our high-resolution crystal structure of HaDHR. We believe that HaDHR is better enzyme for biosensor fabrication because of its lack of substrate inhibition, which could compromise the fidelity of the measurements in high histramine-producing diseased states.

1.1 Requirements of a biorecognition element for a working DET biosensor fabrication

Traditional enzyme immobilization strategies for a working biosensor fabrication typically employ adsorption and/or cross-linking strategies that often inactivate the biorecognition element. A consequence of this random process, beyond enzyme inactivation, is the lack of orientational control needed to support direct electron transfer applications, including the development of a DET

biosensor. The strategy needed for a complete construction of a DET biosensor fabrication requires the following: (1) a highly active biorecognition element, e.g., an enzyme with an appropriate catalytic efficiency (k_{cat}), for the substrate to be measured, (2) enzyme activity that is not limited by the substrate over the physiologic range to be measured, e.g., K_M is not limiting for the measurement, and K_M is not subject to changes as a result of substrate inhibition (3) a molecular level understanding of the electron transfer pathway from the active site of the enzyme to its surface needed to support DET, (4) a high resolution crystal structure is available, (5) the controlled orientation of the enzyme to the transduction element for an efficient DET process, and (6) a strong association of the enzyme on the transduction element so that the enzyme remains immobilized over the course of the measurement, e.g. equilibrium dissociation constant (K_d) is sufficiently low to allow for DET to occur. The relevance of points (5) and (6) are more fully discussed in Chapter 4.

In Chapter 4 of this dissertation, the use of metal binding peptides is explored to facilitate the binding and orientation of HaDHR to a noble metal transduction element (Figure 1-3). HaDHR was engineered with metal binding affinity tags to target the enzyme to Au and Pt surfaces. These peptides were attached to the N and/or C termini of HaDHR. The interactions of these constructs were probed on gold and platinum surfaces using Surface Plasmon Resonance (SPR), Quartz Crystal Microbalance (QCM), and Dynamic Light Scattering (DLS). This study investigates the utility of using noble metal binding peptides to orient HaDHR on the metal surface of a biosensor's transduction element.

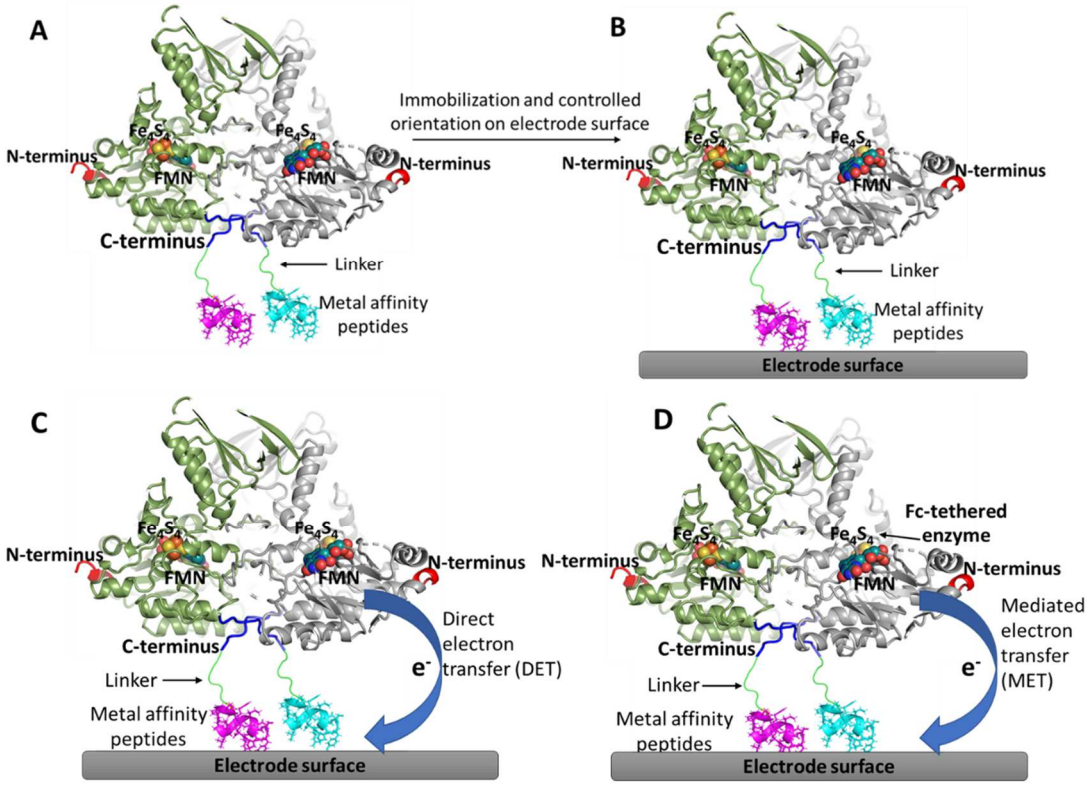

Figure 1-3 Depiction of metal binding peptide modified HaDHR interactions with a noble metal surface

(A) Engineering the enzyme HaDHR with metal affinity peptides for immobilization and controlled orientation on electrode surface, (B) Engineered enzyme attached on the electrode surface, (C) Engineered enzyme might facilitate the possibility of a DET type biosensor, and (D) Fc-tethered enzyme can be engineered for attachment on electrode surface to facilitate the possibility of MET type biosensor.

1.2 References

1. Carthy, E., and Ellender, T. (2021) Histamine, neuroinflammation and neurodevelopment: a review. *Frontiers in Neuroscience*, 870
2. Wada, H., Inagaki, N., Itowi, N., and Yamatodani, A. (1991) Histaminergic neuron system in the brain: distribution and possible functions. *Brain research bulletin* **27**, 367-370
3. Haas, H., and Panula, P. (2003) The role of histamine and the tuberomamillary nucleus in the nervous system. *Nature Reviews Neuroscience* **4**, 121-130
4. Schwartz, J.-C., Arrang, J.-M., Bouthenet, M.-L., Garbarg, M., Pollard, H., and Ruat, M. (1991). in *Histamine and histamine antagonists* (Uvnäs, B. ed.), Springer, Berlin, Heidelberg. pp 191-242
5. Nuutinen, S., and Panula, P. (2010) Histamine in neurotransmission and brain diseases. *Histamine in Inflammation*, 95-107
6. Ishizuka, T., and Yamatodani, A. (2012) Integrative role of the histaminergic system in feeding and taste perception. *Frontiers in systems neuroscience* **6**, 1-9
7. Langlais, P., Zhang, S., Weilersbacher, G., Hough, L., and Barke, K. (1994) Histamine-mediated neuronal death in a rat model of Wernicke's encephalopathy. *Journal of neuroscience research* **38**, 565-574
8. Wada, H. (1992) From biochemistry to pharmacology: the histaminergic neuron system in the brain. *Nihon yakurigaku zasshi. Folia pharmacologica Japonica* **99**, 63-81
9. Onodera, K., Maeyama, K., and Watanabe, T. (1988) Regional changes in brain histamine levels following dietary-induced thiamine deficiency in rats. *The Japanese Journal of Pharmacology* **47**, 323-326
10. Hugo Cifuentes Castro, V., Lucia Lopez Valenzuela, C., Carlos Salazar Sanchez, J., Pardo Pena, K., J Lopez Perez, S., Ortega Ibarra, J., and Morales Villagran, A. (2014) An update of the classical and novel methods used for measuring fast neurotransmitters during normal and brain altered function. *Current neuropharmacology* **12**, 490-508
11. Dale, N., Hatz, S., Tian, F., and Llaudet, E. (2005) Listening to the brain: microelectrode biosensors for neurochemicals. *Trends in biotechnology* **23**, 420-428
12. Ou, Y., Buchanan, A. M., Witt, C. E., and Hashemi, P. (2019) Frontiers in electrochemical sensors for neurotransmitter detection: towards measuring neurotransmitters as chemical diagnostics for brain disorders. *Analytical Methods* **11**, 2738-2755
13. Mirzaei, M., and Sawan, M. (2014) Microelectronics-based biosensors dedicated to the detection of neurotransmitters: A review. *Sensors* **14**, 17981-18008
14. Petillo, P. (2012) A Tissue Implantable Microbiosensor. Health & Environmental Research Online (HERO)
15. Rodrigues, D., Barbosa, A. I., Rebelo, R., Kwon, I. K., Reis, R. L., and Correlo, V. M. (2020) Skin-integrated wearable systems and implantable biosensors: a comprehensive review. *Biosensors* **10**, 79
16. Allioux, C., Meiller, A., Balança, B., and Marinesco, S. (2019) Monitoring Brain Injury With Microelectrode Biosensors. in *Compendium Of In Vivo Monitoring In Real-time Molecular Neuroscience-Volume 3: Probing Brain Function, Disease And Injury With Enhanced Optical And Electrochemical Sensors* (Wilson, G. S., and Michael, A. C. eds.), World Scientific. pp 325-364

17. Liu, H., Ge, J., Ma, E., and Yang, L. (2019) Advanced biomaterials for biosensor and theranostics. in *Biomaterials in translational medicine*, Elsevier. pp 213-255
18. Wilson, G. S., and Gifford, R. (2005) Biosensors for real-time in vivo measurements. *Biosensors and Bioelectronics* **20**, 2388-2403
19. Wilson, G. S., and Johnson, M. A. (2008) In-vivo electrochemistry: what can we learn about living systems? *Chemical reviews* **108**, 2462-2481
20. Wilson, G. S., and Hu, Y. (2000) Enzyme-based biosensors for in vivo measurements. *Chemical reviews* **100**, 2693-2704
21. Naylor, E., Aillon, D., Barett, B., Gabbert, S., Harmon, H., Turek, F., Wilson, G., Johnson, D., and Petillo, P. (2011) Lactate as a Biomarker for Sleep. *Sleep* **35**, 1209-1222
22. Wilson, R., and Turner, A. (1992) Glucose oxidase: an ideal enzyme. *Biosensors and Bioelectronics* **7**, 165-185
23. Chen, C., Xie, Q., Yang, D., Xiao, H., Fu, Y., Tan, Y., and Yao, S. (2013) Recent advances in electrochemical glucose biosensors: a review. *Rsc Advances* **3**, 4473-4491
24. Danne, T., Nimri, R., Battelino, T., Bergenstal, R. M., Close, K. L., DeVries, J. H., Garg, S., Heinemann, L., Hirsch, I., and Amiel, S. A. (2017) International consensus on use of continuous glucose monitoring. *Diabetes care* **40**, 1631-1640
25. Yoo, E.-H., and Lee, S.-Y. (2010) Glucose biosensors: an overview of use in clinical practice. *Sensors* **10**, 4558-4576
26. Hejazi, M., Tong, W., Ibbotson, M. R., Prawer, S., and Garrett, D. J. (2021) Advances in carbon-based microfiber electrodes for neural interfacing. *Frontiers in Neuroscience* **15**, 403
27. Meyyappan, M. (2015) Nano biosensors for neurochemical monitoring. *Nano Convergence* **2**, 1-6
28. Beyene, A. G., Yang, S. J., and Landry, M. P. (2019) Tools and trends for probing brain neurochemistry. *Journal of Vacuum Science & Technology A: Vacuum, Surfaces, and Films* **37**, 040802
29. Rolfe, B., Zhang, B., Campbell, G., Wang, H., Mooney, J., Campbell, J., Huang, Q., Jahnke, S., Le, S.-J., and Chau, Y.-Q. (2011) The fibrotic response to implanted biomaterials: implications for tissue engineering. in *Regenerative Medicine and Tissue Engineering* (Eberli, D. ed.), IntechOpen, University Hospital of Zurich, Switzerland. pp
30. Santos, R. M., and Sirota, A. (2021) Phasic oxygen dynamics confounds fast choline-sensitive biosensor signals in the brain of behaving rodents. *Elife* **10**, e61940
31. Petillo, P., A. (2021).
32. Chen, S., Scherer, A., Adalian, D., Petillo, P., Jilani, M. M., Madero, X. L., and Kumar, D. K. (2021) Method of producing thin enzyme-based sensing layers on planar sensors. Google Patents
33. Schachinger, F., Chang, H., Scheiblbrandner, S., and Ludwig, R. (2021) Amperometric Biosensors Based on Direct Electron Transfer Enzymes. *Molecules* **26**, 4525
34. Chaubey, A., and Malhotra, B. (2002) Mediated biosensors. *Biosensors and bioelectronics* **17**, 441-456
35. Bollella, P., Gorton, L., and Antiochia, R. (2018) Direct electron transfer of dehydrogenases for development of 3rd generation biosensors and enzymatic fuel cells. *Sensors* **18**, 1319

36. Falk, M., Blum, Z., and Shleev, S. (2012) Direct electron transfer based enzymatic fuel cells. *Electrochimica Acta* **82**, 191-202
37. Tasca, F., Zafar, M. N., Harreither, W., Nöll, G., Ludwig, R., and Gorton, L. (2011) A third generation glucose biosensor based on cellobiose dehydrogenase from Corynascus thermophilus and single-walled carbon nanotubes. *Analyst* **136**, 2033-2036
38. Lobo, M. J., Miranda, A. J., and Tuñón, P. (1997) Amperometric biosensors based on NAD (P)-dependent dehydrogenase enzymes. *Electroanalysis* **9**, 191-202
39. Kawai, S., Yakushi, T., Matsushita, K., Kitazumi, Y., Shirai, O., and Kano, K. (2014) The electron transfer pathway in direct electrochemical communication of fructose dehydrogenase with electrodes. *Electrochemistry communications* **38**, 28-31
40. Gorton, L., Lindgren, A., Larsson, T., Munteanu, F., Ruzgas, T., and Gazaryan, I. (1999) Direct electron transfer between heme-containing enzymes and electrodes as basis for third generation biosensors. *Analytica Chimica Acta* **400**, 91-108
41. Ikeda, T., Kobayashi, D., Matsushita, F., Sagara, T., and Niki, K. (1993) Bioelectrocatalysis at electrodes coated with alcohol dehydrogenase, a quinohemoprotein with heme c serving as a built-in mediator. *Journal of Electroanalytical Chemistry* **361**, 221-228
42. Yu, P., and Wilson, G. S. (2000) An independently addressable microbiosensor array: What are the limits of sensing element density? *Faraday Discussions* **116**, 305-317
43. Scherer, A., Petillo Peter, A., and Kishore Kumar, D. (2020) Layered structures for the protection of molecules. in *Google Patents*, California Institute Of Technology CalTech, US
44. Chen, S., Scherer, A., Adalian, D., Petillo, P., Jilani Muhammad, M., Madero Xiomara, L., and Kishore Kumar, D. (2021) Method of producing thin enzyme-based sensing layers on planar sensors. in *Google Patents*, California Institute Of Technology CalTech, US
45. Cash, K. J., and Clark, H. A. (2013) Phosphorescent nanosensors for in vivo tracking of histamine levels. *Analytical chemistry* **85**, 6312-6318
46. Zant, J. C., Rozov, S., Wigren, H.-K., Panula, P., and Porkka-Heiskanen, T. (2012) Histamine release in the basal forebrain mediates cortical activation through cholinergic neurons. *Journal of Neuroscience* **32**, 13244-13254
47. Laurino, A., Landucci, E., Cinci, L., Gencarelli, M., De Siena, G., Bellusci, L., Chiellini, G., and Raimondi, L. (2019) Brain histamine modulates the antidepressant-like effect of the 3-iodothyroacetic acid (TA1). *Frontiers in Cellular Neuroscience* **13**, 176
48. Iwaki, S., Ogasawara, M., Kurita, R., Niwa, O., Tanizawa, K., Ohashi, Y., and Maeyama, K. (2002) Real-time monitoring of histamine released from rat basophilic leukemia (RBL-2H3) cells with a histamine microsensor using recombinant histamine oxidase. *Analytical biochemistry* **304**, 236-243
49. Henao-Escobar, W., Del Torno-de Roman, L., Domínguez-Renedo, O., Alonso-Lomillo, M., and Arcos-Martínez, M. (2016) Dual enzymatic biosensor for simultaneous amperometric determination of histamine and putrescine. *Food chemistry* **190**, 818-823
50. Apetrei, I. M., and Apetrei, C. (2016) Amperometric biosensor based on diamine oxidase/platinum nanoparticles/graphene/chitosan modified screen-printed carbon electrode for histamine detection. *Sensors* **16**, 422
51. Yamada, R., Fujieda, N., Tsutsumi, M., Tsujimura, S., Shirai, O., and Kano, K. (2008) Bioelectrochemical determination at histamine dehydrogenase-based electrodes. *Electrochemistry* **76**, 600-602

52. Sato, T., Horiuchi, T., and Nishimura, I. (2005) Simple and rapid determination of histamine in food using a new histamine dehydrogenase from Rhizobium sp. *Analytical biochemistry* **346**, 320-326
53. Komori, K., Komatsu, Y., Nakane, M., and Sakai, Y. (2021) Bioelectrochemical detection of histamine release from basophilic leukemia cell line based on histamine dehydrogenase-modified cup-stacked carbon nanofibers. *Bioelectrochemistry* **138**, 107719
54. Bakke, M., Sato, T., Ichikawa, K., and Nishimura, I. (2005) Histamine dehydrogenase from Rhizobium sp.: gene cloning, expression in Escherichia coli, characterization and application to histamine determination. *Journal of biotechnology* **119**, 260-271
55. Siddiqui, J. A., Shoeb, S. M., Takayama, S., Shimizu, E., and Yorifuji, T. (2000) Purification and characterization of histamine dehydrogenase from Nocardioides simplex IFO 12069. *FEMS microbiology letters* **189**, 183-187
56. Steenkamp, D. J., McIntire, W., and Kenney, W. C. (1978) Structure of the covalently bound coenzyme of trimethylamine dehydrogenase. Evidence for a 6-substituted flavin. *Journal of Biological Chemistry* **253**, 2818-2824
57. Steenkamp, D. J., and Mallinson, J. (1976) Trimethylamine dehydrogenase from a methylotrophic bacterium. I. Isolation and steady-state kinetics. *Biochimica et biophysica acta* **429**, 705-719
58. Yang, C. C., Packman, L. C., and Scrutton, N. S. (1995) The primary structure of Hyphomicrobium X dimethylamine dehydrogenase: relationship to trimethylamine dehydrogenase and implications for substrate recognition. *European journal of biochemistry* **232**, 264-271
59. Fujieda, N., Satoh, A., Tsuse, N., Kano, K., and Ikeda, T. (2004) 6-S-Cysteinyl flavin mononucleotide-containing histamine dehydrogenase from Nocardioides simplex: molecular cloning, sequencing, overexpression, and characterization of redox centers of enzyme. *Biochemistry* **43**, 10800-10808
60. Limburg, J., Mure, M., and Klinman, J. P. (2005) Cloning and characterization of histamine dehydrogenase from Nocardioides simplex. *Archives of biochemistry and biophysics* **436**, 8-22
61. Tsutsumi, M., Tsuse, N., Fujieda, N., and Kano, K. (2010) Site-directed mutation at residues near the catalytic site of histamine dehydrogenase from Nocardioides simplex and its effects on substrate inhibition. *Journal of biochemistry* **147**, 257-264
62. Lacorn, M., Garrido, G., Reck, B., Sutterlüti, M., Lindeke, S., and Meinhardt, P. (2019) Validation of the R-Biopharm AG RIDASCREEN® histamine (enzymatic) kit: AOAC performance tested methods SM 031901. *Journal of AOAC International* **102**, 1472-1491
63. Yamaguchi, H., Nakata, K., Tatsumi, M., Sugiki, M., Miyano, H., and Mizukoshi, T. (2019) Development of a novel l-histidine assay method using histamine dehydrogenase and a stable mutant of histidine decarboxylase. *Analytical biochemistry* **570**, 13-20
64. Tsutsumi, M., Tsujimura, S., Shirai, O., and Kano, K. (2010) Stopped flow kinetic studies on reductive half-reaction of histamine dehydrogenase from Nocardioides simplex with histamine. *The Journal of Biochemistry* **148**, 47-54

Chapter 2. Structure of Rhizobium sp. 4-9 Histamine Dehydrogenase and Analysis of the Electron Transfer Pathway to Fc^+

2.1 Abstract

Histamine dehydrogenase from the gram-negative bacterium *Rhizobium sp*. 4-9 (HaDHR) is a member of a small family of dehydrogenases containing a covalently attached FMN, and the only member so far identified that does not exhibit substrate inhibition. In this study, we present the crystal structure of HaDHR that was solved to a resolution of 2.1 Å. This new structure allowed for the identification of the internal electron transfer pathway to external artificial ferrocene-based mediators. This study identified alanine 437 as the exit point of electrons from the Fe_4S_4 cluster. HaDHR was reengineered to facilitate the direct attachment of ferrocene proximal to alanine 437 and this construct was shown to be capable of supporting electron transfer from the enzyme to a gold electrode in a histamine dose-dependent manner without the need for any additional electron mediators.

2.2 Introduction

The histamine dehydrogenase from *Rhizobium sp*. 4-9 (HaDHR, UniProtKB: Q60I59_9RHIZ) belongs to a small family of Fe_4S_4 cluster containing amine dehydrogenases with covalently attached FMN co-factors. These enzymes are composed of two identical subunits with average molecular weights of 76-83 kDa, and where co-factor attachment occurs through a conserved cysteine residue in the active site. (1-5) Even though all the enzymes of this family process small amines, the sequence homology within this group is relatively low given the overall functional homology of the family. The best characterized member of the family is the histamine dehydrogenase enzyme from *Nocardioides simplex* (HaDHN, UniProtKB: Q6IWJ5_NOCSI), (2,6,7) which shows reasonable selectivity towards histamine with respect to other biogenic amines. The other two members of the family are dimethylamine dehydrogenase from *Hyphomicrobium sp. (strain x)* (DMADH, UniProtKB: Q48303_HYPSX) and trimethylamine dehydrogenase (TAMDH, UniProtKB: P16099_METME, RCSB:1DJN) from *Methylophilus methylotrophus*.(3,4)

The physiological electron acceptors for HaDHR and HaDHN have not yet been identified, whereas an electron transferring flavoprotein (ETFDH) is the physiological electron acceptor for TMADH, (8) and presumably DMADH. Several artificial electron acceptors such as phenazine methosulfate (PMS) and phenazine ethosulfate (PES) (with dichlorophenolindophenol-DCIP), and ferricenium hexafluorophosphate ($Fc^+PF_6^-$) have been utilized in studies with HaDHN and TMADH in place of the physiological one. (9,10)

HaDHR is the only member of the family that does not exhibit substrate inhibition (1). Many studies have examined the structural and mechanistic details of histamine catalysis in HaDHN, but no consensus for the structural basis of substrate inhibition has emerged (5,10,11). HaDHR has

~55% sequence identity with HaDHN, catalyzing the oxidative deamination of histamine to imidazole acetaldehyde and ammonia (6). HaDHR also shows ~38% sequence identity with DMADH and TMADH. A distinguishing difference between HaDHR and other family members is that HaDHR does not show any substrate inhibition, even at high substrate concentrations, and is, to date, superior to any known dehydrogenase enzyme in terms of histamine specificity and enzyme stability as measured by loss of activity over time (1). HaDHR has been previously cloned and expressed in *E.coli*, purified, but only partially characterized. The lack of a high resolution HaDHR structure has precluded the detailed comparison with HaDHN as part of a broader investigation into the origins of substrate inhibition in the HaDHR enzyme.

In this study, we present the crystal structure of HaDHR at a resolution of 2.1 Å. This new structure enabled a better understanding of the electron transfer pathways in HaDHR to artificial electron mediators such as Fc^+ and provided additional insights into the possible electron transfer pathway to the enzyme's natural acceptors. As part of this study, we mutated a key serine residue known to be involved in electron transfer to a cysteine residue for attachment of ferrocene maleimide as an artificial electron transfer mediator. The electron transfer rates of HaDHR with the conjugated ferrocene were monitored using electrochemistry and are also disclosed as part of this study. This combined structural and electron transfer study demonstrates the promise of HaDHR as the biorecognition element in a histamine biosensor (12,13).

The terms ferrocene and ferricenium will both be used throughout this Chapter. For clarity, note that the difference in spelling of the ferricenium (Fc^+) vs. ferrocene (Fc) is indicative of the oxidation state of ferrocene.

2.3 Experimental Procedures

2.3.1 Materials

Histamine, carbenicillin, chloramphenicol, Sephadex G-50 resin, azurin from *Pseudomonas aeruginosa*, cytochrome c from equine heart, ferredoxin from spinach, N-ferrocenyl-maleimide (Fc-maleimide), ferricenium hexafluorophosphate ($Fc^{+}PF_6^{-}$) and bilirubin oxidase were purchased from Sigma Aldrich. Ferrocenedimethanol (Fc-DM) was purchased from Santa Cruz Biotechnology, and Ni-NTA resin was purchased from Qiagen. DNaseI was purchased from Roche. The primers used in this study were obtained from Integrated DNA Technologies. Gold and platinum electrodes of 2 mm disk OD and 0.5mm Ag/AgCl wire electrodes were purchased from CH Instruments.

2.3.2 Gene construct

DNA encoding the full-length histamine dehydrogenase enzyme from *Rhizobium sp.* 4-9 (protein_id="BAD54700.1") were obtained from Integrated DNA technologies. The genes were cloned into the pMCSG7 vector (14), which incorporated a 6xHis tag on the N-terminus of the protein followed by a tobacco etch virus (TEV) cleavage site, using a ligation independent cloning method (15). The resulting plasmid (Figure 2-1A) was transformed into competent *E.coli* XL10 Gold cells (Agilent Technologies) and the sequence was confirmed commercially (ACGT Inc.).

2.3.3 Protein expression and purification

The sequenced wildtype or mutant plasmid DNA was transformed into the expression host *E. coli* BL21 (DE3)/pRARE and the enzyme was expressed upon addition of isopropyl β-D-1-thiogalactopyranoside to 0.1 mM and incubated overnight at 15 °C in a shaking incubator. Cells were harvested by centrifugation at 5,000 x g for 10 min, frozen at -80 °C overnight, thawed and sonicated for 2 min on ice using an alternating 2 sec on/8 sec off duty cycle at 30% amplitude in Buffer A (50 mM potassium phosphate, pH 7.4, 0.15 M NaCl and 5 mM imidazole) plus 5 U/mL of DNaseI. Insoluble material was removed by centrifugation at 20,000 x g for 60 min at 4 ºC. The soluble cell fraction was applied to a 3 mL of Ni-NTA resin equilibrated in Buffer A and protein eluted in Buffer A containing 250 mM imidazole. At this stage the enzyme was >95% pure as judged by SDS-polyacrylamide gel electrophoresis. Glycerol was added to 20% (v/v) and the protein was snap frozen in liquid nitrogen and stored at -80 ºC. Gel electrophoresis was performed on pre-cast NuPage® 12% acrylamide gels (Invitrogen) under reducing conditions (Figure 2-1B).

Prior to crystallization, the protein was treated with tobacco etch virus (TEV) protease to remove the 6xHis-tag in buffer A containing 5 mM Dithiothreitol (DTT) and 1 mM EDTA, 27.4 mg of HaDHR and 2.7 mg of TEV protease. The reaction mixture was incubated for two days at 4 °C. After desalting to remove the DTT and EDTA, the protein was subjected to reverse Ni^{2+} affinity chromatography. Purified protein from the eluate was incubated with 5 mM FMN for two days at 4 °C followed by size exclusion chromatography on a Superdex 200 Increase GL column equilibrated with 10 mM Tris-HCl buffer, pH 8.0. The protein was concentrated to 10 mg/ml for crystallization screens.

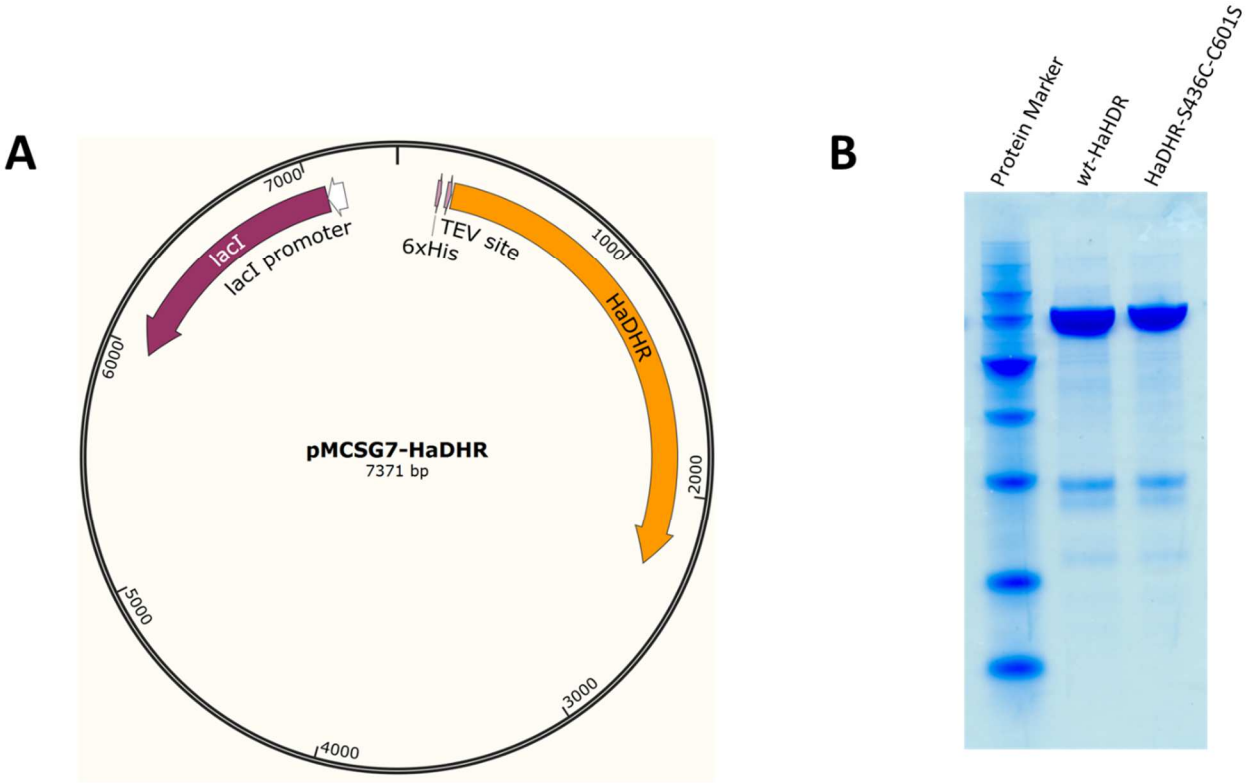

Figure 2-1 Gene Construct and SDS-PAGE

A) The plasmid map showing the HaDHR gene cloned in pMCSG7 vector. B) SDS-PAGE gel image showing *wt*-HaDHR and HaDHR-S436C-C601S double mutant after Ni-NTA column purification. The estimated molecular weight for the *wt*-HaDHR and HaDHR-S436C-C601S is ~76 kDa for each subunit.

2.3.4 Crystallization and data collection

Purified HaDHR, in 10 mM Tris-HCl, pH 8 was concentrated to 10 mg/mL (0.64 mM) for crystallization screening. All crystallization experiments were setup using an NT8 drop-setting robot (Formulatrix Inc.) and UVXPO MRC (Molecular Dimensions) sitting drop vapor diffusion plates at 18 ^{o}C. 100 nL of protein and 100 nL of each crystallization solution from the Proplex HT Screen kit (Molecular Dimensions) were dispensed and equilibrated against 50 µL of the latter. Crystals were obtained from condition F4 (18% (w/v) PEG 12,000, 100 mM HEPES pH 7.0). Samples were transferred to a drop containing 80% crystallant and 20% PEG 200 before storing in liquid nitrogen. X-ray diffraction data were collected at the Advanced Photon Source beamline 17-ID using a Dectris Pilatus 6M pixel array detector.

The diffraction data were integrated using XDS (16) and scaled with AIMLESS from the CCP4 program suite (17,18). The scaled data were used to obtain an initial phasing model via the molecular replacement program Phaser (19) using the histamine dehydrogenase from *Nocardiodes simplex* (PDB accession number 3K30) as the search model (5). Based on the Matthew's coefficient (20) each asymmetric unit contained two molecules (V_m = 2.49 Å^3 Da^{-1}, 51% solvent). The top solution was obtained in the space group $P2_12_12_1$ with two molecules in the asymmetric unit. The model was improved using automated model building with Arp/wARP (21) and Autobuild in Phenix (22). Subsequent refinement and manual model building were conducted with Phenix (22) and Coot (23) respectively. Disordered side chain atoms were truncated to the point where electron density could be observed. Structure validation was conducted with Molprobity (24) and figures were prepared with CCP4mg (25). Relevant crystallographic data are provided in Table 2-3.

2.3.5 Preparation of oxidized ferricenium dimethanol (Fc^+-DM)

Ferrocenedimethanol was oxidized to (Fc^+-DM) before use by treatment with bilirubin oxidase as follows: 0.1 mg of bilirubin oxidase was added to 5 mM of Fc-DM in 0.2 M air-saturated potassium phosphate buffer, pH 5.8 and oxidation of Fc-DM was followed as an increase in absorption at 640 nm (26). The reaction was allowed to continue until the oxidation was complete as indicated by the change in color of the ferrocene solution from yellow to blue. The pH of the solution was adjusted to pH 2.5 by addition of HCl to denature and precipitate the bilirubin oxidase then returned to pH 7.4 by the addition of 1M NaOH.

2.3.6 Electron acceptor-dependent steady-state kinetic assays.

Steady-state kinetic assays were performed to determine the K_M for the natural and artificial acceptors (Table 2-1) under saturating histamine concentration. Assays were performed in a 1 mL reaction volume in a 1 cm pathlength cuvette. Reaction mixtures were comprised of 100 mM potassium phosphate buffer, pH 7.4, 20 nM HaDHR, histamine (10 mM) and varying concentrations of electron acceptors. The reactions were monitored at the appropriate wavelength for each electron acceptor (Table 2-1) in a Cary 50 UV-spectrophotometer. The absorbance versus time at different acceptor concentrations were recorded and the optical velocity was determined by linear regression fit to the steady state data over a time period of 1 min. The optical velocities were converted to chemical velocities by dividing by the extinction coefficient of each acceptor. The apparent K_M and the V_{max} were obtained by fitting the chemical velocity data via non-linear regression to the Michaelis-Menten equation using Graph pad prism software. The apparent k_{cat} for each acceptor was determined by dividing V_{max} by the enzyme concentration. Protein concentrations were determined using the average of three Bradford assays (27). Assays were performed at 25 °C.

Table 2-1: Electron Acceptor Spectral Properties

Electron acceptors	Wavelength (nm)	Extinction coefficient
Cytochrome c	550	29500 M^{-1} cm^{-1}(28)
Ferredoxin	420	9400 M^{-1} cm^{-1} (29)
Azurin	625	3500 M^{-1} cm^{-1}(30)
Ferricenium Hexafluorophosphate($Fc^{+}PF_6^{-}$)	617	410 M^{-1} cm^{-1}(31,32)
Ferricenium dimethanol (Fc^{+}DM)	640	241 $M^{-1}cm^{-1}$

2.3.7 Histamine-dependent steady-state kinetic assays of *wt*-HaDHR and HaDHR mutants with Fc^+DM

Steady-state kinetic assays were performed to determine the K_M for histamine under saturating concentrations of Fc^+-DM. Assays were performed in a 1 mL reaction volume in a 1 cm pathlength cuvette. Reaction mixtures were comprised of 100 mM potassium phosphate buffer, pH 7.4, HaDHR (0.25 μM), varying histamine concentrations (0- 2 mM) and Fc^+-DM (2.5 mM). Assays were performed at 25 °C. Reactions were monitored at 640 nm in a Cary 50 UV-spectrophotometer. Absorbance versus time at different histamine concentrations were recorded and the optical velocity was determined by linear regression fit to the steady state data. The optical velocities were converted to chemical velocities by dividing by the extinction coefficient of Fc^+-DM (ΔA_{640}= 241 $M^{-1}cm^{-1}$). The apparent K_M and the V_{max} were obtained by fitting the chemical velocity data via non-linear regression to the Michaelis-Menten equation using Graph pad prism software. Apparent k_{cat} for histamine oxidation was determined by dividing V_{max} by the enzyme concentration. Protein concentrations were determined using the average of three Bradford assays (27).

2.3.8 Site directed mutagenesis

Mutations informed from the crystal structure of HaDHR were generated in the *wt*-HaDHR expression plasmid ORF by using the Quick-change site directed mutagenesis kit (Agilent Technologies). Plasmid DNA was purified from mutant transformant colonies, and the mutations were validated by Sanger sequencing.

2.3.9 Enzyme conjugation with ferrocene (Fc) maleimide

Conjugation of the HaDHR S436C-C601S double mutant enzyme with Fc-maleimide was done using standard maleimide chemistry (33). A 3.4 mM stock of Fc-maleimide in DMSO was mixed with protein in a 4:1 molar ratio in 100 mM potassium phosphate buffer, pH 7.4 at 25 ºC and

incubated for 15 min. The incubated mixture was then purified twice by gel filtration chromatography using Sephadex G-50 fine desalting columns to remove any free or unconjugated Fc-maleimides. The completeness of the conjugation reaction was assessed by mass spectrometry and by coumarin maleimide challenge of the Fc-maleimide conjugated enzyme. Coumarin maleimide dye was mixed in the same molar ratio as above and the kinetic measurements were measured at excitation 387 nm and emission 470 nm using fluorescence spectroscopy (34). The intensities of the HaDHR enzymes in presence of the coumarin maleimide dye were recorded for 15 min and conjugation verified by mass spectrometry.

2.3.10 Rotating disc electrochemical measurements with Fc^{+}DM in solution

Gold working electrodes were thoroughly cleaned using an electrode polishing kit from Pine Instruments. Chronoamperometry solution measurements were performed on a Model 7104E series Electrochemical analyzer (CH Instruments, Inc.) in 30 mL of 100 mM potassium phosphate buffer, pH 7.4. Solutions were degassed for 15 min prior to measurement. The measurements were done using a rotating ring disc gold electrode of 12 mm OD (Pine Instruments) with 0.5 mm platinum wire as a counter electrode and a 0.5mm Ag/AgCl wire as a reference electrode. A potential of 0.4V vs Ag/AgCl and a rotation speed of 1500 rpm was applied for all measurements.

Chronoamperometry measurements on the *wt*-HaDHR, HaDHR S436C-C601S double mutant and the Fc-tethered HaDHR C601S-S436C enzyme were performed in the presence of Fc^{+}-DM (2.5 mM). The histamine concentration range employed was 1 μM-2 mM. The enzyme concentration for all measurements were kept at 0.25 μM. All measurements were done in triplicates at room temperature.

The resulting currents at varying concentrations of histamine were recorded and the apparent K_M and C_{max} were obtained by fitting the data via non-linear regression to the Michaelis-Menten equation using Graph pad prism software.

2.3.11 Electrochemical measurements of *wt*-HaDHR, HaDHR S436C-C601S and Fc-tethered HaDHR S436C-C601S

Gold working electrodes (2 mm, CH Instruments) were thoroughly cleaned using an electrode polishing kit from Pine Instruments. Chronoamperometry solution measurements were performed on a 6 mL 100 mM potassium phosphate buffer pH 7.4 using a Gamry Interface 1010T potentiostat. Solutions were degassed for 15 min prior to measurement. The measurements were made in a three-electrode electrochemical cell with a platinum wire as a counter electrode and Ag/AgCl wire as a reference electrode, with sintered glass plugs between each cell. A potential of 0.4V vs a Ag/AgCl reference electrode was applied, and the solutions were continuously stirred for all measurements.

Triplicate measurements on the buffer, *wt*-HaDHR, HaDHR S436C-C601S double mutant and the Fc-tethered HaDHR C601S-S436C enzyme were performed in the absence of any artificial mediator. For each experiment, a 10 min run-in period was used prior to the histamine dose response. The histamine concentration range employed was 2-480 µM. The enzyme concentration for all measurements was kept at 2 µM. Data were collected at 10 Hz for 200s per concentration and then averaged. The resulting currents at varying concentrations of histamine were recorded and the apparent K_M and C_{max} were obtained by fitting the data via non-linear regression to the Michaelis-Menten equation using Graph pad prism software.

2.3.12 Calculation of FMN butterfly angle

The butterfly angle for the FMN cofactor was calculated by averaging four dihedral angles about the N5-N10 axis in FMN (Table 2-2). Specifically, the dihedrals defined by C2-N10-N5-C7, C2-N5-N10-C8, N3-N5-N10-C8 and N3-N10-N5-C7 using standard FMN crystallographic numbering were calculated by using Chem 3D (version 16.0) for each molecule of cofactor in HaDHR (PDB ID: 6DE6), HaDHN (PDB ID: 3K30), and TMADH (PDB ID: 1DJN). The individual dihedral angles, each of which represent one calculated value of the putative butterfly angle, were averaged to yield a composite butterfly angle for each enzyme.

Table 2-2: FMN butterfly angle calculations

PDB ID	1DJN (TMADH)		3K30 (HaDHN)		6DE6 (HaDHR)	
	Molecule A	**Molecule B**	**Molecule A**	**Molecule B**	**Molecule A**	**Molecule B**
C2-N10-N5-C7	23.3	23.5	15.8	12.6	18.5	15.1
C2-N5-N10-C8	20.0	19.5	15.9	9.5	15.2	14.5
N3-N5-N10-C8	29.3	28.1	27.3	12.4	19.6	19.1
N3-N10-N5-C7	22.1	21.6	17.5	9.7	14.2	11.9
	23.7	23.2	19.1	11.1	16.9	15.2
Average	**23.4**		**15.1**		**16.0**	

**Molecules A and B refer to the flavin cofactor in subunits A and B, respectively, of each RCSB crystal structures.*

2.3.13 Mass Spectrometry

MALDI samples were prepared by combining one part of the protein, one part of 2',4',-dihydroxyacetophenone (DHAP, 15 mg/mL in ammonium citrate buffer) solution, and one part of 2% Trifluoroacetic acid (TFA). The resulting solution was mixed thoroughly. Once crystallization started, 1µL of the solution was spotted onto a stainless steel MALDI plate then dried before loading the plate into the Bruker Autoflex maX LRF MALDI-TOF mass spectrometer (Bruker Daltonics, Billerica MA). MALDI data were acquired using the linear-positive ion mode with the following acquisition parameters: an IS1 voltage of 19.5 kV, an IS2 voltage of 18.3 kV, a lens voltage of 7 kV, and a delay time of 350 nsec.

2.4 Results

2.4.1 Structural properties of HaDHR

Crystallographic data and crystal properties are described in Table 2-3. HaDHR crystallized as a non-crystallographic dimer with monomers bound in an antiparallel conformation with long (~20 residue) C-terminal loops packed together on the same interface bringing the C-terminal proline residues to within 17 Å of each other (Figure 2-2A). Using the TM-align program (35), alignment of HaDHR revealed an RMSD and TM align scores of 1.10 Å and 0.98 for HaDHN (Figure 2-2B) and 1.70 Å and 0.97 for TMADH. Significant structural differences among the three enzymes do occur and are mainly located in loop segments (Figure 2-3). While no structure has been reported for DMADH, we expect similar structural variations to occur.

The isoalloxazine ring of the FMN of HaDHR is covalently attached to Cys30 within the catalytic pocket. This cofactor has essentially the same bend about the N5-N10 axis of the flavin ring (~16°) as that found in HaDHN (~15°), which are both significantly less extreme than that observed in TMADH (~25°) (Figure 2-2C). In the FMN binding site (Figure 2-2D) of both HaDHN and TMADH structures there is a Tyr-His-Asp triad that has been identified as important for both FMN binding and substrate inhibition (5,10,36). This triad is comprised of Tyr 176, His 179, and Asp270 in HaDHN, and Tyr169, His172, and Asp267 in TMADH close to the pyrimidine moiety of the isoalloxazine ring of the FMN. A homologous triad is present in HaDHR though differing in that Cys266 replaces the Asp residue observed in HaDHN and TMADH. In both HaDHR and HaDHN, modelling suggests substrate binding to Gln60/65, Trp263/267 and Asp354/358 whereas, in TMADH the substrate binds to Tyr60, Trp264 and Trp355 forming the previously proposed “aromatic bowl” (5,37).

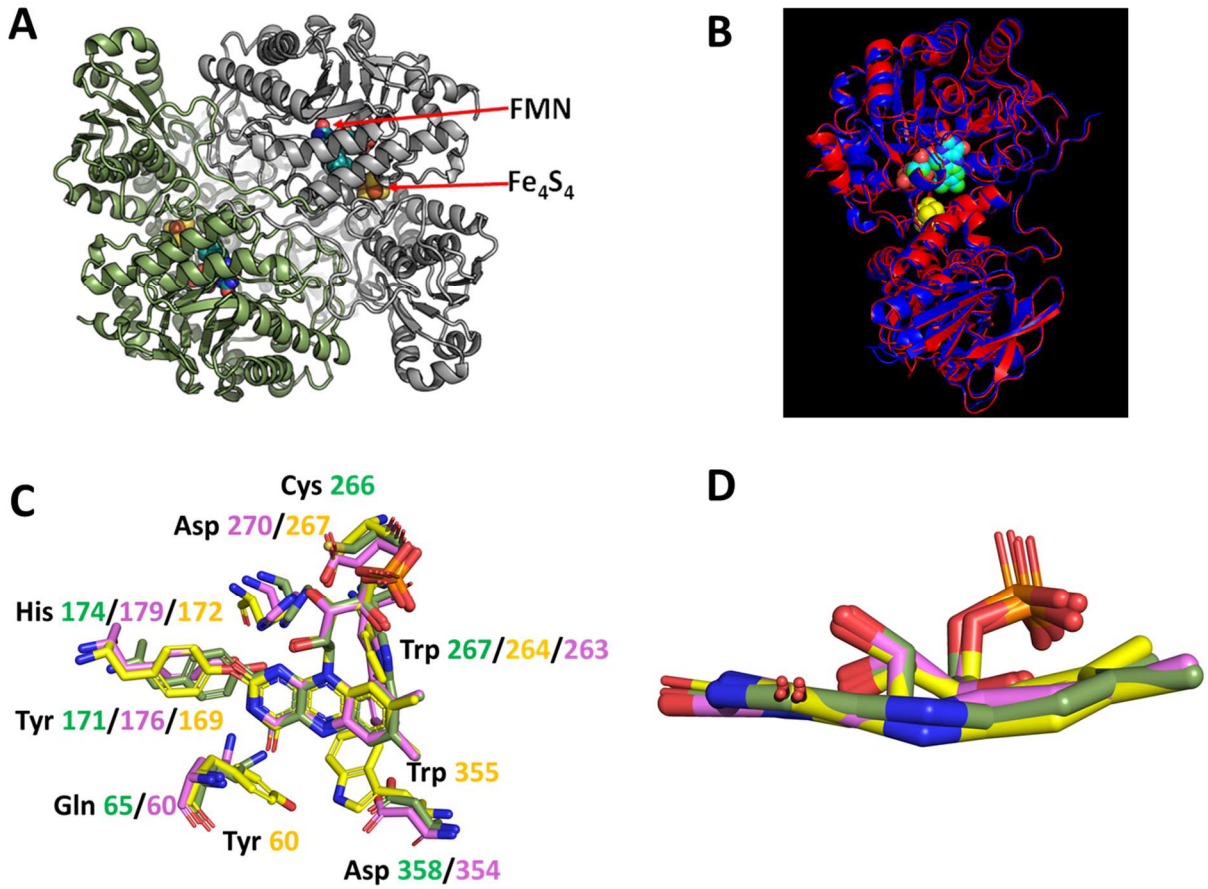

Figure 2-2 Structure of the HaDHR homodimer (RCSB: 6DE6) and its alignment to the closest structural homolog in the PDB, HaDHN (RCSB:3K30) and TMADH (RCSB:1DJN) A) HaDHR crystal structure (RCSB:6DE6) has two subunits that are arranged antiparallel to one another. The positions of the covalently bound FMN and Fe_4S_4 cofactors are indicated with arrows. B) Backbone atom TM alignment of HaDHR and HaDHN (RCSB:3K30). The HaDHR backbone is shown in blue, and the HaDHN backbone is shown in red. The FMN is shown in cyan and the Fe_4S_4 is shown in yellow spheres. C) Superimposed stereo view of the FMN binding site for HaDHR (green), HaDHN (pink) and TMADH (yellow). D) Comparison of the bend in the N5-N10 axis of the flavin ring in HaDHR (green), HaDHN (pink) and TMADH (yellow).

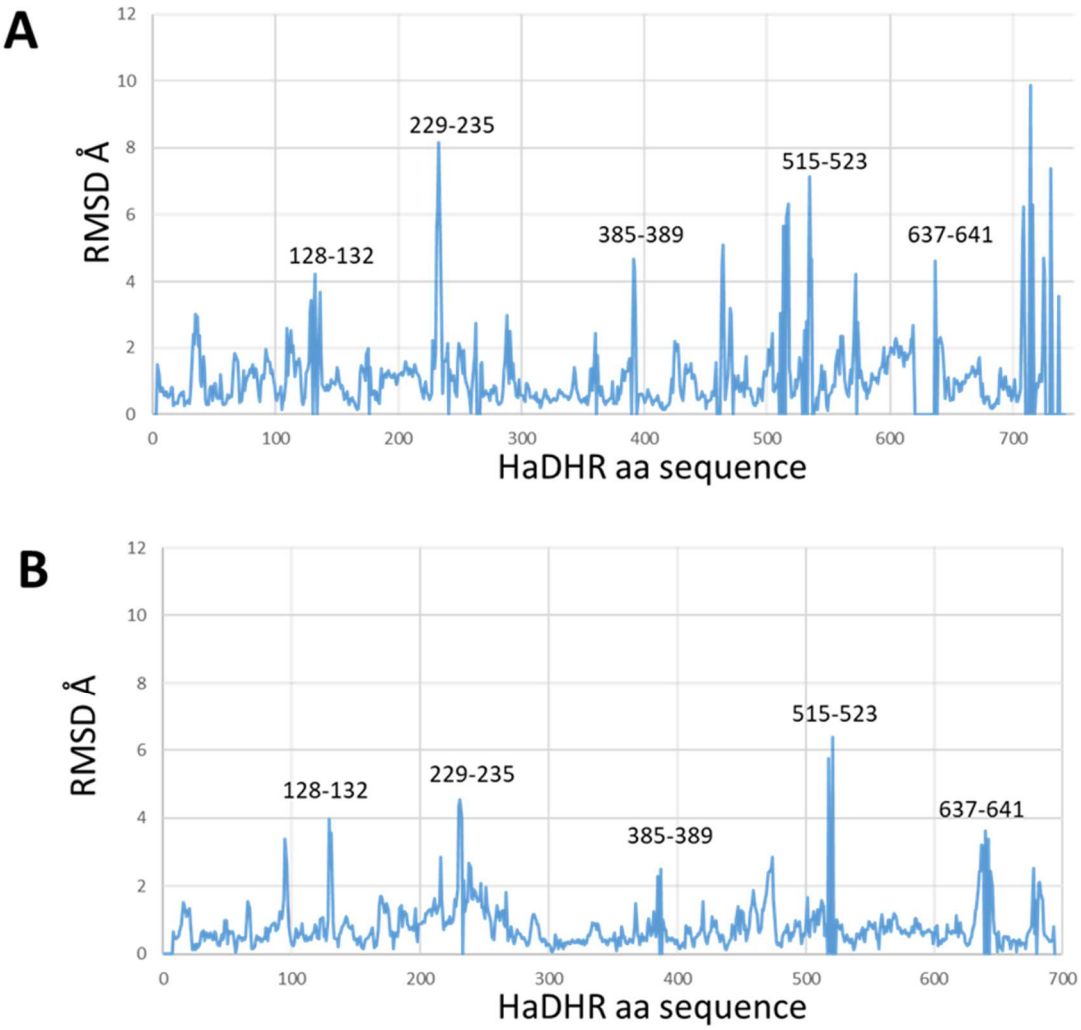

Figure 2-3 Crystallographic alignment of HaDHR with other family members
Superposition of backbone atoms of HaDHR with (A) TMADH and (B) HaDHN. Major variations from backbone RMSD values are mostly in loop sections as indicated by numbering.

Table 2-3: Crystallographic data statistics for Histamine dehydrogenase from *Rhizobium sp.*

	Histamine dehydrogenase (PDB code 6DE6)
Data Collection	
Unit-cell parameters (Å, °)	*a*=103.22, *b*=105.31, *c*=140.04
Space group	$P2_12_12_1$
Resolution (Å)[1]	48.43-2.14 (2.14-2.10)
Wavelength (Å)	1.0000
Temperature (K)	100
Observed reflections	586,744
Unique reflections	89,613
$\langle I/\sigma(I)\rangle$[1]	12.7 (1.7)
Completeness (%)[1]	100 (99.9)
Multiplicity[1]	6.5 (6.5)
R_{merge} (%)[1, 2]	0.106 (1.222)
R_{meas} (%)[1, 4]	0.115 (1.329)
R_{pim} (%)[1, 4]	0.045 (0.519)
$CC_{1/2}$ [1, 5]	0.998 (0.640)
Refinement	
Resolution (Å)	48.43-2.10
Reflections (working/test)	85,051/4,463
R_{factor} / R_{free} (%)[3]	16.4/20.2
No. of atoms (protein/water/6-S-Cys-FMN /4Fe-4S/ADP/PO_4)	10,303/554/62/16/54/5
Model Quality	
R.m.s deviations	
Bond lengths (Å)	0.009
Bond angles (°)	0.998
Average *B* factor (Å^2)	
All Atoms	37.1
Protein	37.1

Water	37.9
6-S-Cys-FMN	34.0
[4Fe-4S]	41.7
ADP	32.0
PO_4	59.7
Coordinate error, maximum likelihood (Å)	0.22
Ramachandran Plot	
Most favored (%)	96.0
Additionally allowed (%)	3.5

1) Values in parenthesis are for the highest resolution shell.
2) $R_{merge} = \Sigma_{hkl}\Sigma_i |I_i(hkl) - \langle I(hkl)\rangle| / \Sigma_{hkl}\Sigma_i I_i(hkl)$, where $I_i(hkl)$ is the intensity measured for the ith reflection and $\langle I(hkl)\rangle$ is the average intensity of all reflections with indices hkl.
3) $R_{\text{factor}} = \Sigma_{hkl} ||F_{\text{obs}}(hkl)| - |F_{\text{calc}}(hkl)|| / \Sigma_{hkl} |F_{\text{obs}}(hkl)|$; Rfree is calculated in an identical manner using 5% of randomly selected reflections that were not included in the refinement.
4) R_{meas} = redundancy-independent (multiplicity-weighted) R_{merge}(17,18). R_{pim} = precision-indicating (multiplicity-weighted) R_{merge} (38);(39)
5) $CC_{1/2}$ is the correlation coefficient of the mean intensities between two random half-sets of data (40);(41)

2.4.2 Catalytic properties of HaDHR with different electron acceptors

The native electron acceptor for HaDHR is unknown. Based on the previously proposed electron acceptors for HaDHN (2,6) and other dehydrogenases (42) we tried the following electron acceptors: cytochrome c, ferredoxin, azurin, phenazine methosulfate/water-soluble tetrazolium salt-8 dye couple (PMS/WST-8), ferricenium hexafluorophosphate ($Fc^+PF_6^-$), and ferricenium dimethanol (Fc^+-DM). Among the protein acceptors, none gave a measurable rate of turnover (Table 2-4). A significant rate was obtained with two artificial mediators, $Fc^+PF_6^-$, and Fc^+-DM. The rate of histamine oxidation observed with Fc^+-DM was similar to that obtained for HaDHN with $Fc^+PF_6^-$ (10). When Fc^+-DM was used as an electron acceptor, HaDHR exhibited Michaelis Menten kinetics with respect to histamine oxidation with no observed substrate inhibition. Unlike HaDHN (2), inhibition by tryptophan was not observed in HaDHR (Figure 2-4).

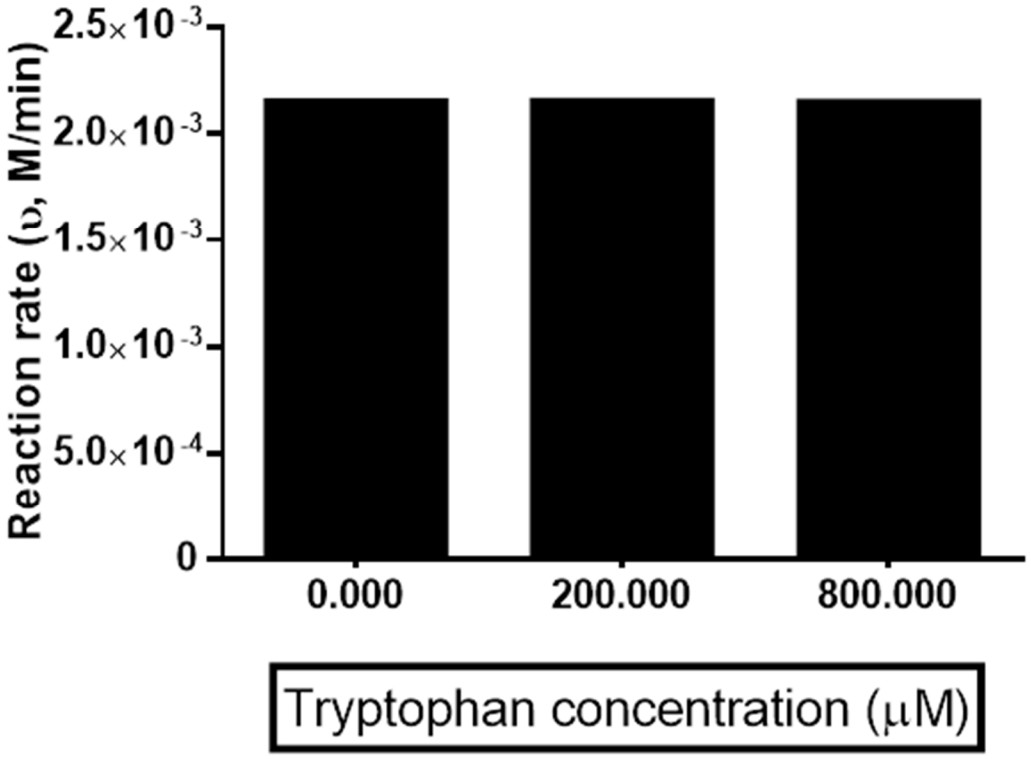

Figure 2-4 Tryptophan inhibition study
Tryptophan inhibition study at fixed HaDHR (1 μM), histamine (2 mM) and $Fc^{+}DM$ (2.5 mM) in absence and presence of tryptophan.

Table 2-4: Apparent turnover rate (k_{cat}) and K_M at saturating histamine concentrations for different electron acceptors.

Electron acceptors	**Apparent k_{cat} (s^{-1})**	**Apparent K_M (μM)**	**E'$_o$ (V)***
Cytochrome c	ND	ND	0.248 (43)
Ferredoxin	ND	ND	-0.42 (44)
Azurin	ND	ND	0.293-0.31 (45)
$Fc^+PF_6^-$	108.6 ± 7.5	532 ± 61.3	0.865 (46)
Fc^+DM	195.4 ± 4.3	690 ± 48.2	0.245

*****E'$_o$ (V) is the midpoint formal potential vs Ag/AgCl electrode*

2.4.3 Probing electron transfer pathway from HaDHR to Fc^+DM

The electron transfer pathway from HaDHR to Fc^+ is unknown. Previous studies on TMADH implicate certain residues as important to the process of shuttling electrons from the Fe_4S_4 cluster to Fc^+ ions in solution (31). Comparison of the HaDHR and HaDHN crystal structures revealed the presence of identical residues in structurally homologous positions (highlighted in Figure 2-5). Reed *et al.* proposed that in HaDHN, electrons transfer from the Fe_4S_4 cluster occurs via Cys348 to Glu347 and exits through Arg444 for natural electron acceptors, whereas for Fc^+, electrons transfer via Cys348 to Ala441 (5).

Based on Reed's observations (5), we investigated the electron transfer pathway of HaDHR to Fc^+-DM in solution. The formal potential in aqueous medium for Fc^+ is 0.255V (47) and 0.245V for Fc^+-DM (Figure 2-6). Mutations (E343A, A437V, A437G and R440Y) were made in HaDHR at positions spatially homologous to residues in HaDHN that were proposed important by Reed *et al*. for electron acceptor reduction (5). Histamine dependent-steady state kinetic analyses revealed a ~51% reduction in k_{cat} for the E343A mutant, a ~59% reduction for the A437V mutant, and a ~96% reduction for the A437G mutant (Table 2-5). By contrast, the R440Y mutant did not show any significant change in turnover, suggesting that this residue is not involved in the electron transfer pathway. The modest change in kinetics observed for the E343A and A437V mutants, and the significant change observed for the A437G mutant suggests involvement of Ala437 in the transfer of electrons from the Fe_4S_4 cluster to the Fc^+-DM artificial mediator in solution.

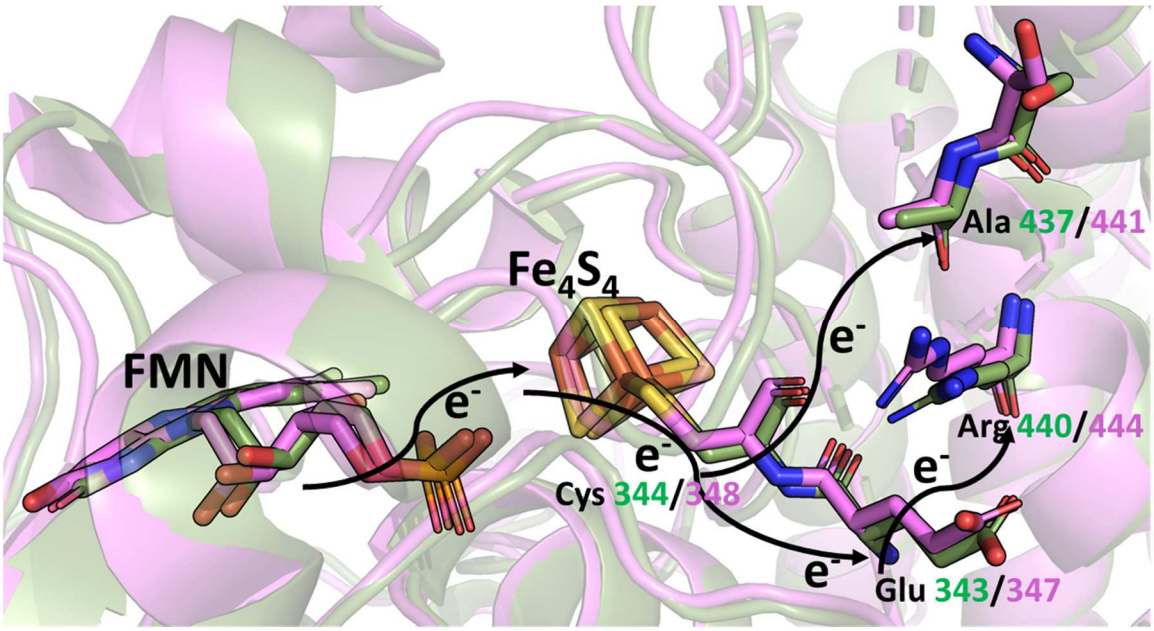

Figure 2-5 Residues proposed for electron transfer pathway in HaDHR based on HaDHN structure

Overlayed structure of HaDHR (green) and HaDHN (pink) showing the putative residues involved in electron transfer pathway. Based on TMADH and HaDHN studies, two electron transfer pathways have been proposed for HaDHR as indicated by arrows. (1) FMN → Fe_4S_4 → Cys344 →Glu343 → Arg440 for natural electron acceptors, (2) FMN → Fe_4S_4 → Cys344 → Ala437 for artificial mediators (Fc^+)

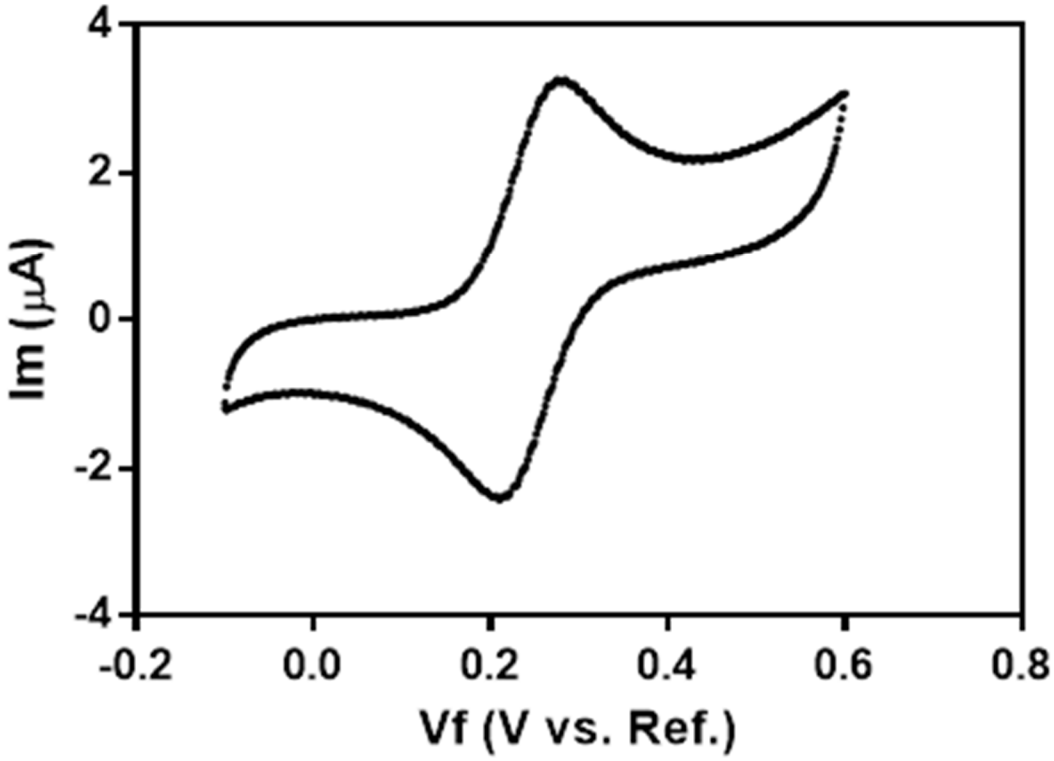

Figure 2-6 Cyclic voltammetry for $Fc^{+}DM$
Cyclic voltammetry for $Fc^{+}DM$ (0.2 mM) in 100 mM potassium phosphate buffer, pH=7.4 at a scan rate of 100 mV/s. The midpoint formal potential for Fc^{+} was calculated to be 0.245V vs the Ag/AgCl reference electrode.

Table 2-5: Spectroscopically determined histamine-dependent steady state kinetic parameters of HaDHR and single point mutant variants putatively involved in the electron transfer pathway to Fc^{+}DM. Standard errors from non-linear regression to the Michaelis-Menten equation are reported.

Protein Construct[1]	k_{cat} (s^{-1})	Reduction in k_{cat} (wt-mut) (s^{-1})	K_M, µM	Reduction in K_M (wt-mut) µM
***wt*-HaDHR**	99.1 ± 5.9	-	695 ± 94.7	-
HaDHR E343A	48.4 ± 3.2	50.7 (~51%)	627 ± 98.4	68 (~10%)
HaDHR R440Y	86.5 ± 8.5	12.6 (~13%)	662 ± 155.3	33 (~5%)
HaDHR A437V	40.6 ± 2.3	58.5 (~59%)	564 ± 94.6	131 (~19%)
HaDHR A437G	4.4 ± 0.5	94.7 (~96%)	332 ± 112.1	363 (~52%)
HaDHR S436C-C601S	90.7 ± 2.6	8.4 (~8.5%)	646 ± 71.1	49 (~7.1%)
HaDHR S436C-C601S with tethered Fc[2]	120.7 ± 5.1	-21.6 (~-17.9%)	632 ± 63.2	63 (~9.1%)

[1]Protein concentration = 0.25 µM, Fc^{+}-DM concentration= 2.5 mM

[2] HaDHR S436C-C601S with tethered Fc is the product of the reaction of HaDHR S436C-C601S conjugated with Fc-maleimide

2.4.4 Electrochemical measurements with Fc^{+}DM in solution

Based on our electron transfer pathway studies with Fc^{+}-DM, we hypothesized that attachment of a Fc-moiety at position 436 (highlighted in orange in Figure 2-7) would be sufficient to support electron transfer without involvement of any other electron acceptor free in solution. We mutated this residue to cysteine to facilitate attachment of ferrocene through standard maleimide chemistry (Figure 2-8,(33)). While HaDHR has a total of ten cysteines, only Cys601 is solvent exposed (Figure 2-7), and this residue was mutated to a serine to simplify the maleimide chemistry. The HaDHR S436C-C601S double mutant was then conjugated with Fc-maleimide, and the modification was confirmed by mass spectrometry (Figure 2-9, Table 2-6). The difference between the observed weight and the accurate weight is within the mass accuracy of MALDI-TOF for larger proteins, i.e., ≤ 500 ppm (48). A 500 ppm error corresponds to a difference 40Da which is greater than the mass difference observed between the theoretical and the actual mass of Fc-maleimide observed using MaLDI-TOF.

The electrochemical evaluation of the unconjugated and conjugated enzymes in the presence of the free Fc^{+}-DM performed under histamine-dependent steady state conditions showed that the maximum currents were all within 20% of the wildtype values (Table 2-7). The electrochemically determined K_M of the unmodified and modified enzyme were similar to values obtained from spectrophotometric steady-state kinetic assays (Table 2-5).

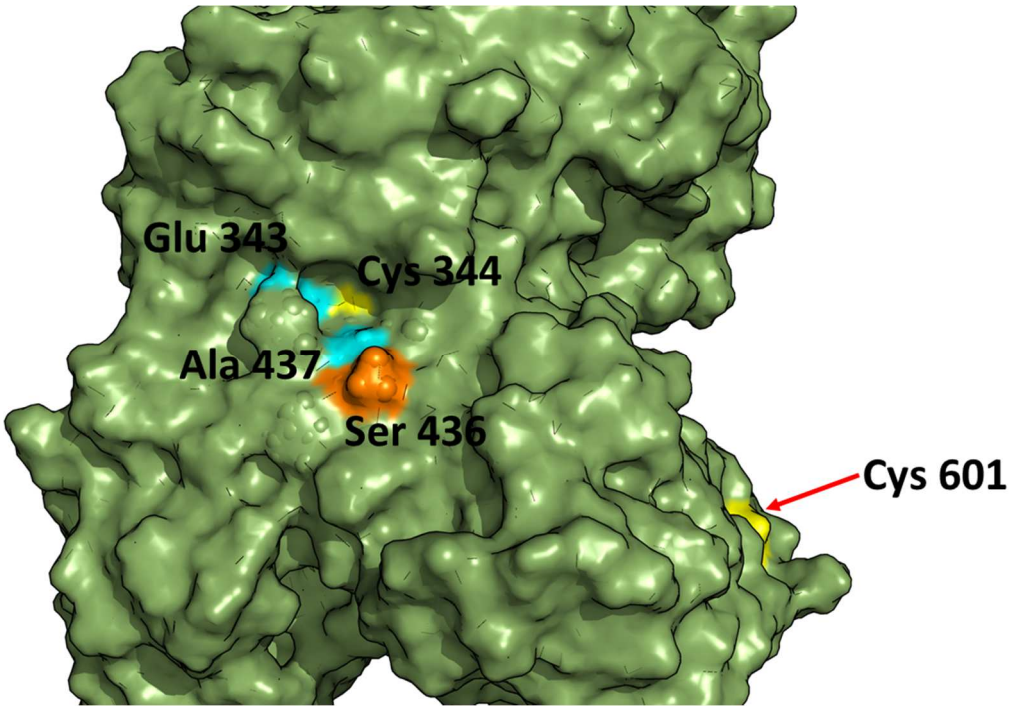

Figure 2-7 Surface model of HaDHR showing Ser436

Ser436 residue proposed to be the attachment site of Fc-maleimide to HaDHR is highlighted in orange. The solvent exposed Cys601 residue that was mutated to Ser is indicated by an arrow and highlighted in yellow. The residues proposed to be involved in electron transfer from the Fe_4S_4 are also highlighted in cyan (Ala437 and Glu343)**.**

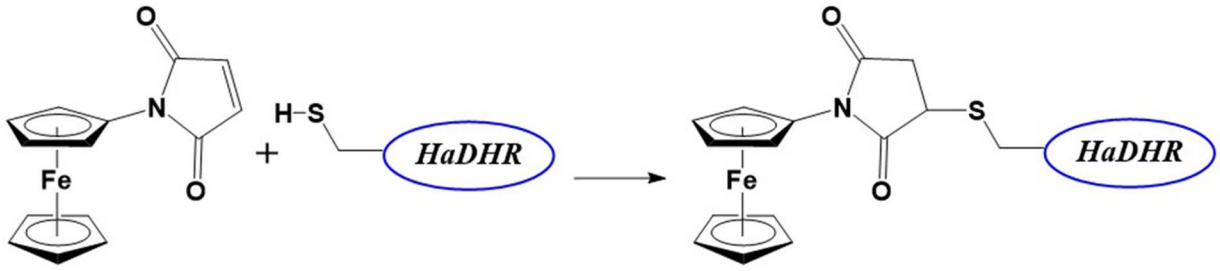

Figure 2-8 Depiction of Fc-maleimide conjugation to HaDHR
The HaDHR S436C-C601S double mutant was conjugated with Fc-maleimide using standard chemistry to tether an artificial ferrocene electron acceptor proximal to the putative exit point of electrons resulting from the oxidation of histamine.

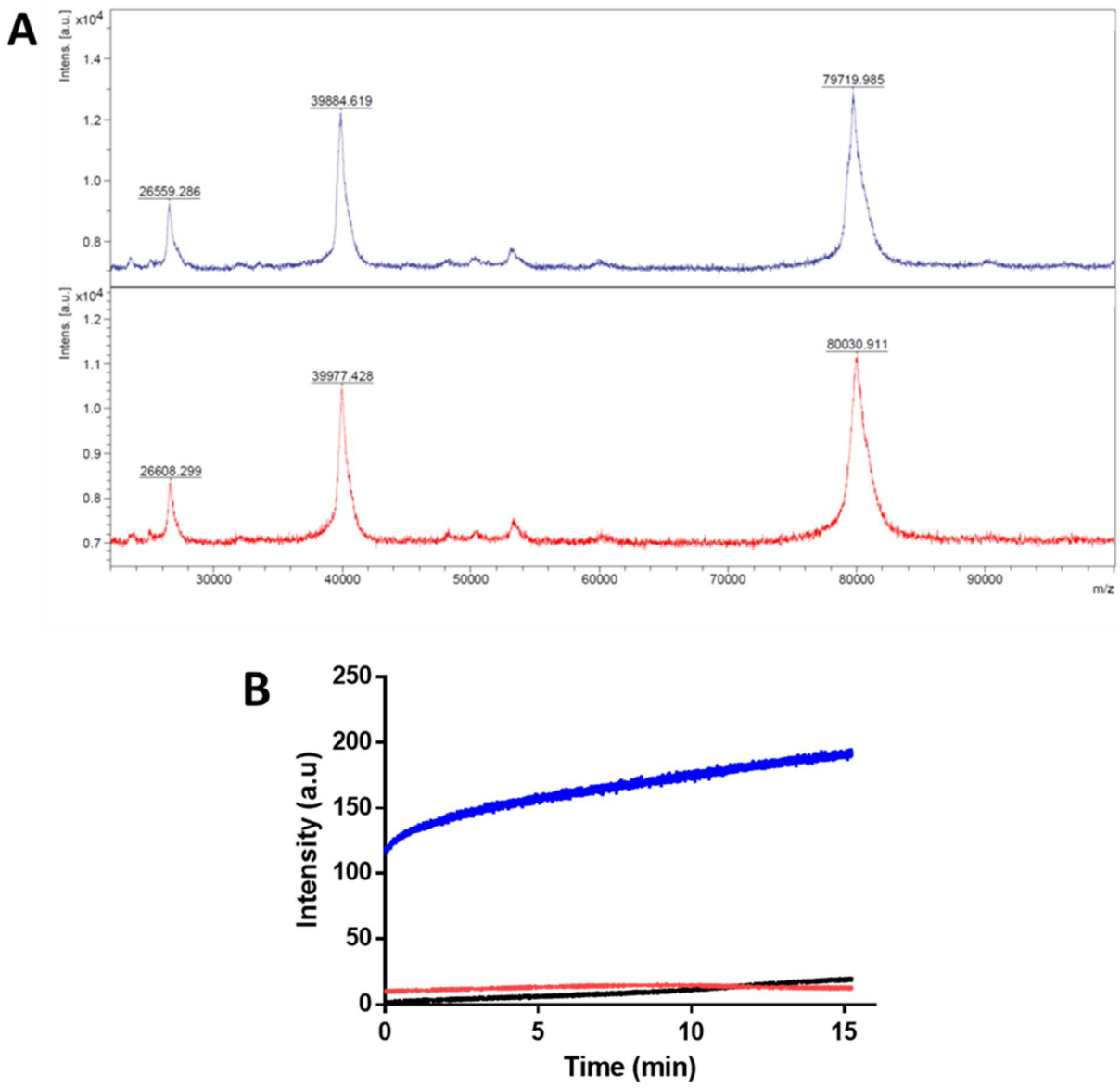

Figure 2-9 Mass Spectrometry and coumarin maleimide study
(A) Mass Spectrometric study of HaDHR S436C-C601S double mutant (blue) and the Fc-conjugated HaDHR S436C-C601S enzyme (red), (B) coumarin maleimide study showing successful attachment of Fc-maleimide. Coumarin maleimide and buffer (black), HaDHR S436C-C601S double mutant (blue) and the Fc-conjugated HaDHR S436C-C601S enzyme (red).

Table 2-6: Mass spectrometric analysis

Construct name	**Molecular weight (Da)**
HaDHR S436C-C601S	Observed weight = 79720
Fc-conjugated HaDHR S436C- C601S	Observed weight = 80031
	$\Delta = 311$
N-Ferrocenyl- maleimide	Calculated weight = 281.09

Note: The difference between the Δ molecular weight (311 Da) and the molecular weight of the N-Ferrocenyl-maleimide is within experimental error of the MALDI-TOF technique used in this study which is ≤ 500 ppm for larger proteins.

Table 2-7: Histamine-dependent steady state kinetic analyses in presence of free Fc^+-DM in solution. Standard errors from non-linear regression to the Michaelis-Menten equation are shown.

Protein Construct[1]	$Current_{max}$ (μA)	K_M (μM)
***wt*-HaDHR**	701 ± 47	950 ± 145
HaDHR S436C-C601S	575 ± 23	682 ± 66
HaDHR S436C-C601S with tethered Fc[2]	666 ± 20.0	714 ± 53

[1]Protein concentration = 0.25 μM, Fc^+-DM concentration= 2.5 mM

[2]HaDHR S436C-C601S with tethered Fc is the product of the reaction of HaDHR S436C-C601S conjugated with Fc-maleimide

2.4.5 Electrochemical measurements of HaDHR, HaDHR S436C-C601S and Fc-tethered HaDHR S436C-C601S

Solution chronoamperometry measurements were performed on the unmodified and modified enzyme in presence of varying concentrations of histamine in the absence of free Fc^+-DM. No background current was detected when histamine was titrated in the presence of *wt*-HaDHR, the HaDHR S436C-C601S double mutant, or buffer. By contrast, when histamine was titrated in the presence of Fc-tethered HaDHR S436C-C601S double mutant, a histamine dependent current was observed (Figure 2-10). The observed $current_{max}$ was 5.1 ± 0.2 nA, and the apparent K_M for this construct under these conditions was 12.7 ± 1.9 μM.

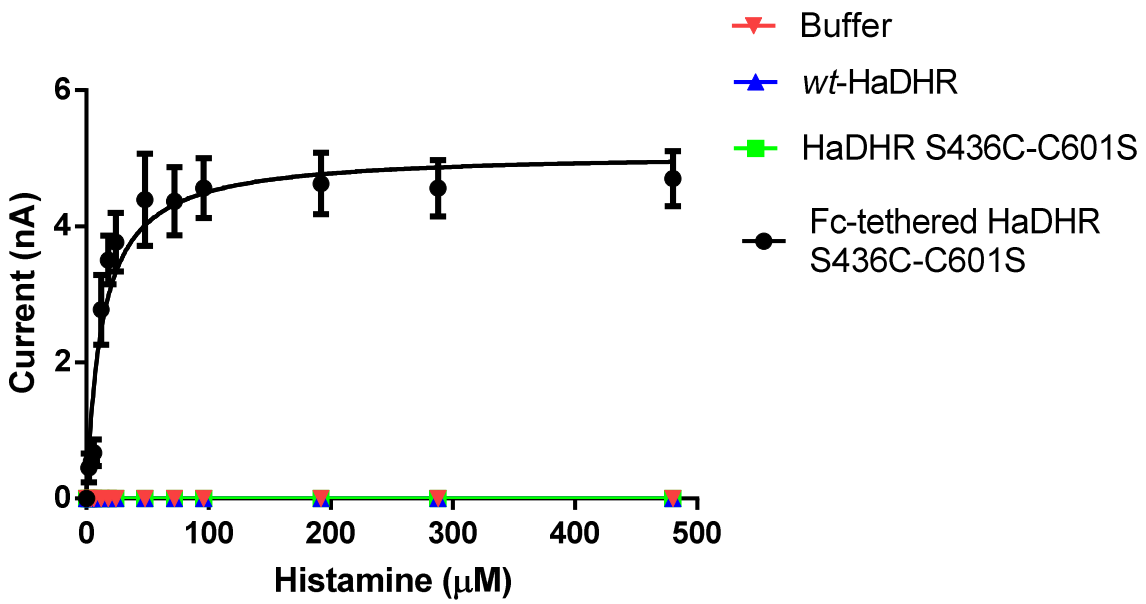

Figure 2-10 Current vs histamine concentration graph
The current vs histamine concentration graph for buffer, *wt*-HaDHR, HaDHR S436C-C601S and Fc-tethered HaDHR S436C-C601S in the presence of varying concentrations of histamine. The assays were performed in 100 mM potassium phosphate buffer, pH 7.4 at 25 ºC. The enzyme concentrations used were 2 μM. No response as a function of histamine concentration was observed for the buffer alone (e.g., no response observed for histamine), the *wt*-HaDHR, and the HaDHR S436C-C601S mutant proteins.

2.5 Discussion

Here we report the crystal structure of HaDHR at a resolution of 2.1 Å (Figure 2-2A). Our structure reveals an enzyme with a covalently attached FMN cofactor and an Fe_4S_4 cluster consistent with other members of the family (Figure 2-2B). HaDHR has ~55% amino acid sequence identity with HaDHN and the overall backbone structure alignment indicated high structural homology between the two enzymes (RMSD and TM align scores of 1.10 Å and 0.98). Interestingly, despite this high level of structural homology, HaDHR does not exhibit substrate inhibition in contrast to HaDHN which shows substrate inhibition at concentrations above 200 μM histamine (10). TMADH, another well characterized member of this flavin dependent amine oxidoreductase enzyme family (EC:1.5.8), has only ~35% amino acid sequence identity with HaDHR (1) but retains a high level of structural homology (RMSD and TM align scores of 1.70 Å and 0.97).

Our structure reveals that the FMN cofactor of HaDHR is covalently linked to Cys30. Mutation of this residue to serine abolished all enzymatic activity despite the fact that flavin was bound to the enzyme, as demonstrated by this mutant's yellow color after purification. This loss of activity is presumably due to the improper orientation of the cofactor with respect to other residues necessary for histamine oxidation. A similar observation was reported for the analogous cysteine in TMADH (49).

HaDHR crystallized as a homodimer. While chain A was well resolved with the exception of the N-terminus, chain B is missing modellable electron density corresponding to residues Leu228-Val242, Gln260-Leu281, Phe299 and Thr300. These missing residues result in the active site model of chain B being incomplete. This suggests that chain B of HaDHR may be more disordered than chain A if this disorder is not a crystallographic artefact. Our structure also revealed the presence of an inorganic phosphate bound to chain B proximal to the loop region in chain A that

is disordered in chain B (Leu228-Val242). The disorder in chain B may contribute to the lack of a second observed phosphate. TMADH also shows the presence of a bound phosphate although it is located in the active site near the FMN binding pocket (49), unlike in HaDHR where it is bound to the surface of the protein.

Each subunit of HaDHR showed the presence of an ADP molecule consistent with that observed in HaDHN and TMADH (5,49). In all three structures, a clearly defined cavity for ADP binding is observed. The addition of ATP or ADP up to 10 mM did not affect Michaelis-Menten kinetics. The importance of this site and its role in mediating the *in vivo* function of the enzyme remains unknown. We speculate that this ADP binding site may be a vestigial pocket derived from an ancestorial FAD binding protein or the site is used to help modulate ATP/ADP levels to maintain cellular energetic homeostasis via ADP allosteric regulation.

The active sites of HaDHR and HaDHN are very similar (Figure 2-2C). One major difference is the presence of an active site cysteine (Cys266) in HaDHR that is an aspartate (Asp270) in HaDHN. This aspartate residue has been proposed earlier to be involved in substrate inhibition aspect of HaDHN (10). Modeling studies performed on HaDHN have suggested that Gln60, Trp263 and Asp354 are involved in binding the substrate; identical residues at the homologous positions are observed in the HaDHR crystal structure (Gln65, Trp267, and Asp358). Similar modeling studies performed on TMADH suggest that the substrate binds to Tyr60, Trp264 and Trp355, forming the previously proposed “aromatic bowl” (5,37).

The natural electron acceptors for HaDHR and HaDHN are unknown, and the only identified natural electron acceptor for TMADH is electron transfer flavoprotein-ubiquinone oxidoreductase (ETFDH, UniProtID: P55931) (8). We surveyed several natural and artificial electron mediators and demonstrated that ferricenium hexafluorophosphate and Fc^{+}-DM can function in this capacity.

Cytochrome c (equine heart), ferredoxin (spinach) and azurin (*Pseudomonas aeruginosa)*, three naturally occurring acceptors for dehydrogenases, failed to accept electrons from HaDHR. A source for ETFDH was unavailable for testing.

An advantage of Fc^+-DM is its water solubility in both the oxidized and reduced forms, the former being readily generated from the latter by the action of bilirubin oxidase. Ferricenium hexafluorophosphate, used as an artificial mediator for studies on other members of the family, is insoluble in buffer at pH=7.4 when reduced and at concentrations above 1 mM, thereby making long term optical measurements or determinations of k_{cat} at higher substrate concentrations difficult. Ferricenium hexafluorophosphate also slowly precipitates in buffer as the hexafluorophosphate counterions slowly hydrolyze. For all these reasons ferricenium hexafluorophosphate proved to be a poor choice as an acceptor for *in vitro* kinetic analysis. The rate observed for the Fc^+-DM/HaDHR couple is comparable to that reported for the ferricenium hexafluorophosphate/HaDHN couple, although the apparent K_M of the former under saturating histamine concentrations is ~10-fold higher (2,5,10). The apparent K_M's were different in two enzymes for Fc most probably due to the insolubility of the ferricenium hexafluorophosphate in physiological buffer which might have made the measurements at high substrate concentartions difficult.

Computational and experimental studies on flavoproteins have suggested that the geometry of the flavin, and in particular the bend about the N5-N10 axis, modulates the formal potential of the cofactor (49-52). A higher bend angle, sometimes referred to as the butterfly angle, has been experimentally associated with an increase in the formal potential of the flavin, meaning more facile thermodynamic reduction (52-54). Free flavin cofactors in solution have a planar isoalloxazine ring system, whereas the reduced cofactors have a significant bend about the N5-

N10 axis (52). Multiple flavin-dependent oxidoreductase enzymes have been observed to induce bending about this axis, conformationally moving the oxidized cofactor along the reaction coordinate towards the reduced state and greatly increasing the formal potential of the flavin. In this way, these enzymes modulate the reactivity of their cofactors for substrate oxidation (52,55).

A structural comparison between HaDHR, HaDHN and TMADH showed that FMN in the HaDHR structure (Figure 2-2D) has a butterfly bend about the N5-N10 axis of ~16°, which is closer to the ~15° reported for HaDHN as compared to the ~25° reported for TMADH (5,49). In principle there are several ways that the butterfly bend can be determined and to our knowledge there is no universally accepted approach to perform this calculation. A variety of atoms about the N5-N10 axis can be used to define the two planes that in turn define the bend angle. This bend angle is more properly referred to as the dihedral angle about the N5-N10 axis. The quality of the model about the cofactor also plays a major role in determining the actual observed bend. We chose to average four key dihedral angles about the N5-N10 axis to determine the bend angle, and this approach should be universal for all flavin cofactors.

For all subsequent analysis related to flavin geometry and flavin related studies only chain A in the HaDHR structure was analyzed, because chain B is incomplete and disordered. Thus, we expect an incomplete picture from the analysis of chain B and the associated flavin. We expect that if a complete, fully formed structure of chain B and the flavin were available, results similar to those from chain A would be observed.

The formal potentials for HaDHN and TMADH for the fully oxidized from to the one electron-reduced form of the flavin moiety have been determined to be +34 mV and +44 mV vs. a Standard Hydrogen Electrode (SHE) respectively. For the one electron-reduced form to the fully reduced form it has been reported to be +30 mV and +36 mV respectively (56-58). Experimental (53,59-

62) and theoretical (50,60,63) studies on flavoproteins have suggested that a higher bend angle of the isoalloxazine ring is often associated with more facile substrate oxidation. While most studies do not relate changes in the bend angle to a formal potential, multiple reports state that flavoprotein catalysis is generally controlled by the potential of the flavin, which in turn, is controlled by the bend angle of the isoalloxazine ring (60,61,64). A higher bend angle increases the relative stability of the fully reduced state with respect to the semiquinone state (50,65,66), a phenomenon that is discussed by Tsutsumi *et al.* during their studies of HaDHN (11). The spectroelectrochemistry of HaDHR was outside the scope of this current study. However, based on the butterfly bend observed for the FMN in HaDHR, we would predict that the formal potential for the fully oxidized form to the one electron-reduced form should be ~+35 mV, and the subsequent reduction to the fully reduced form should occur at ~+30 mV(5,56,57).

For this family of enzymes, electron transfer from the Fe_4S_4 cluster to the surface of the protein is seemingly dependent upon the nature of the acceptor (31,67). Basran *et al.* proposed that in TMADH, the natural acceptor ETFDH accepts electrons from the Fe_4S_4 cluster via the pathway Cys345→Glu439→Tyr442. By contrast, for the artificial acceptor Fc^+, a shorter pathway was proposed involving Cys345→Val344 (5,31). No studies on the electron transfer pathway in HaDHN have been reported, as the pathway was assumed to be conserved within the family (5). If these pathways are correct, the analogous pathways in HaDHR would involve Cys344→Glu343→Arg440 for a natural acceptor, and Cys344→Ala437 for artificial acceptors based on structural homology with TMADH.

Our site-directed mutagenesis/kinetic studies on mutations at Glu343, and Ala437 suggest the importance of these residues in mediating electron transfer to Fc^+, and that Arg440 is not likely

involved in transferring electrons for the artificial mediator. These studies also suggest that the electron transfer pathway for Fc^+ may be from Fe_4S_4 to Cys344 to Ala437 via Glu343.

The distance between the closest atom of the flavin ring system (C8) and Fe_4S_4 (Fe_2) is 5.6 Å and the distance between Fe_4S_4 and the residues that are involved in transferring electrons to Fc^+ is ~5 Å for (Fe4S4 → Cys344 → Ala437) to ~8 Å (Fe4S4 → Cys344 → Glu343 → Ala 437) (Figure 2-5). Consistent with the model proposed for TMADH, a significant decrease in the catalytic rate was observed for the A437G surface mutation, thereby suggesting that electrons exit the protein from this residue to be accepted by Fc^+-DM in solution.

We leveraged the identification of Ala437 as the exit point for electrons from the protein to tether an artificial Fc^+ mediator proximal to this site. We hypothesized that Ser436, which is adjacent to Ala437, could be used to tether a ferrocene molecule to the protein. Ser436 was mutated to a cystine to accept ferrocene maleimide, a commercially available reagent that readily reacts with thiols. Cys601, the only solvent exposed cystine on the surface of the protein, was simultaneously mutated to a serine to prevent any unwanted ferrocene attachment. A coumarin maleimide fluorescence study was performed to confirm the attachment of ferrocene moiety. Coumarin maleimide shows very little fluorescence in solution, but strongly fluoresces upon reaction with a thiol group. Prior to conjugation, the S436C-C601S double mutant strongly fluoresced in the presence of coumarin, and no fluorescence was observed after conjugation with ferrocene maleimide. A MALDI mass spectrum of the ferrocene maleimide conjugate showed a molecular ion corresponding to the mass of a single tethered ferrocene maleimide, and no molecular ions corresponding to multiple conjugations was observed (Figure 2-9, Table 2-6).

To verify the spectroscopic studies presented in Table 2-5, a corresponding electrochemical study in presence of Fc^+-DM in solution was performed. The goal was to determine if the tethered Fc

construct is electrochemically active in the presence of an artificial mediator in solution. Comparing the currents of the *wt*-HaDHR with the tethered Fc constructs, similar activities were observed (Table 2-7). These results suggested that the constructs were electrochemically active, and further suggested that tethered Fc is not restricting the flow of electrons to the free mediator. The current observed for HaDHR-S436C-C601S double mutant is slightly lower than the tethered Fc construct, thereby further suggesting that the presence of Fc is somehow enhancing the electron transfer process and is not inhibitory.

Rotating disc electrochemical studies on the tethered Fc-enzyme system in presence of Fc^+-DM showed higher currents compared to *wt*-HaDHR and the unmodified double mutant (Table 2-7). This demonstrated that the tethered Fc-enzyme system was active and further confirmed the attachment of the ferrocene maleimide to the enzyme surface. Given the observed currents, most of the contribution of the tethered Fc- enzyme system is presumably from the reduction of the soluble (untethered) Fc^+-DM in solution. Comapring the K_{cat} values for *wt*-HaDHR, HaDHR-S436C-C601S, and HaDHR-S436C-C601S with tethered Fc (Table 2-5), it appears that the tethered Fc is actually enhancing the overall catalytic rate with Fc^+-DM in solution. Regardless for this explanation for this observation, these data show that the tethered Fc does not materially interfere with the overall enzyme kinetics. A possible explanation for the observed enhancement of catalysis could be the high local concentration of Fc due to the tether.

The observed increase in k_{cat} for the tethered-Fc HaDHR S436C-C601S compared to *wt*-haDHR in solution with Fc^+-DM, might be explained in two ways (Table 2-5). First, the surface mutations might result in an internal electron transfer pathway that bypasses the Fe_4S_4 cluster. Alternatively, the presence of the tethered-Fc HaDHR S436C-C601S might facilitate better electron transfer to the Fc^+-DM in solution either by removing steric occlusions that might slow down the process or

by protecting the electrons to be transferred to the Fc^{+}-DM in the tethered Fc. The contribution of the current from the tethered Fc is negligible in this experiment, suggesting that the tethered Fc may enhance the interaction of Ala437 with free Fc-DM in solution. This is suggested by the increase in current from the mutant to the tethered mutant which cannot be explained by the contribution to the total current due to the tethered Fc (Table 2-7).

Solution chronoamperometry studies showed that the tethered Fc-enzyme system was able to transfer electrons to an electrode surface in the absence of any other mediator in a histamine dose-dependent manner (Figure 2-10). The currents obtained in this modality were low, presumably due to slow diffusion of the tethered system in solution. Nonetheless, we conclude that the tethered system is capable of undergoing electron transfer in the absence of any other mediator. We hypothesized that the HaDHR enzyme, if properly oriented on the surface of the electrode, might be capable of undergoing direct electron transfer as part of the construction of a Gen 2.5 or Gen 3 biosensor (see Chapter 4 of this dissertation). These studies are currently underway.

In conclusion, the crystal structure of HaDHR solved at 2.1 Å resolution allowed for the structural comparison with other members of its family. The combined structural and solution electrochemical studies presented here offer new insights into engineering this enzyme for use in a histamine biosensor for *in vivo* biosensing applications. A distinguishing feature of HaDHR, unlike other histamine dehydrogenases, is the normal Michaelis-Menten kinetics, and its performance is not compromised by substrate inhibition. The natural electron acceptor has yet to be identified for HaDHR, and evaluation of several common natural electron acceptors for other dehydrogenases failed for this enzyme. Artificial ferrocene-based acceptors were shown to be capable of a high rate of histamine oxidation, which was verified by standard optically based Michaelis-Menten kinetics and by electrochemical chronoamperometry measurements. Kinetic

analysis of a series of structure guided mutations involved in the HaDHR electron transfer pathway showed it to be similar to that proposed for TMADH. Based upon this analysis, the exit point of electrons from the Fe_4S_4 cluster to the surface of the protein was identified, which in turn facilitated the reengineering of the enzyme to harness its electron transfer properties. The enzyme proved capable of delivering electrons to ferrocenes both in solution and tethered to the protein, the latter being a necessary first step in using HaDHR as the biorecognition element in a Gen 2.5 or Gen 3 biosensor.

2.6 References

1. Bakke, M., Sato, T., Ichikawa, K., and Nishimura, I. (2005) Histamine dehydrogenase from Rhizobium sp.: gene cloning, expression in Escherichia coli, characterization and application to histamine determination. *Journal of biotechnology* **119**, 260-271
2. Siddiqui, J. A., Shoeb, S. M., Takayama, S., Shimizu, E., and Yorifuji, T. (2000) Purification and characterization of histamine dehydrogenase from Nocardioides simplex IFO 12069. *FEMS microbiology letters* **189**, 183-187
3. Steenkamp, D. J., and Beinert, H. (1982) Mechanistic studies on the dehydrogenases of methylotrophic bacteria. 2. Kinetic studies on the intramolecular electron transfer in trimethylamine and dimethylamine dehydrogenase. *Biochemical Journal* **207**, 241-252
4. Steenkamp, D. J., and Mallinson, J. (1976) Trimethylamine dehydrogenase from a methylotrophic bacterium. I. Isolation and steady-state kinetics. *Biochimica et biophysica acta* **429**, 705-719
5. Reed, T., Lushington, G. H., Xia, Y., Hirakawa, H., Travis, D. M., Mure, M., Scott, E. E., and Limburg, J. (2010) Crystal structure of histamine dehydrogenase from Nocardioides simplex. *Journal of Biological Chemistry* **285**, 25782-25791
6. Fujieda, N., Satoh, A., Tsuse, N., Kano, K., and Ikeda, T. (2004) 6-S-Cysteinyl flavin mononucleotide-containing histamine dehydrogenase from Nocardioides simplex: molecular cloning, sequencing, overexpression, and characterization of redox centers of enzyme. *Biochemistry* **43**, 10800-10808
7. Limburg, J., Mure, M., and Klinman, J. P. (2005) Cloning and characterization of histamine dehydrogenase from Nocardioides simplex. *Archives of biochemistry and biophysics* **436**, 8-22
8. Huang, L., Rohlfs, R. J., and Hille, R. (1995) The Reaction of Trimethylamine Dehydrogenase with Electron Transferring Flavoprotein (∗). *Journal of Biological Chemistry* **270**, 23958-23965
9. Falzon, L., and Davidson, V. L. (1996) Kinetic model for the regulation by substrate of intramolecular electron transfer in trimethylamine dehydrogenase. *Biochemistry* **35**, 2445-2452
10. Tsutsumi, M., Tsuse, N., Fujieda, N., and Kano, K. (2010) Site-directed mutation at residues near the catalytic site of histamine dehydrogenase from Nocardioides simplex and its effects on substrate inhibition. *Journal of biochemistry* **147**, 257-264
11. Tsutsumi, M., Tsujimura, S., Shirai, O., and Kano, K. (2010) Stopped flow kinetic studies on reductive half-reaction of histamine dehydrogenase from Nocardioides simplex with histamine. *The Journal of Biochemistry* **148**, 47-54
12. Hatada, M., Loew, N., Inose-Takahashi, Y., Okuda-Shimazaki, J., Tsugawa, W., Mulchandani, A., and Sode, K. (2018) Development of a glucose sensor employing quick and easy modification method with mediator for altering electron acceptor preference. *Bioelectrochemistry* **121**, 185-190
13. Thévenot, D. R., Toth, K., Durst, R. A., and Wilson, G. S. (2001) Electrochemical biosensors: recommended definitions and classification. *Biosensors and bioelectronics* **16**, 121-131

14. Stols, L., Gu, M., Dieckman, L., Raffen, R., Collart, F. R., and Donnelly, M. I. (2002) A new vector for high-throughput, ligation-independent cloning encoding a tobacco etch virus protease cleavage site. *Protein expression and purification* **25**, 8-15
15. Qin, H., Hu, J., Hua, Y., Challa, S. V., Cross, T. A., and Gao, F. P. (2008) Construction of a series of vectors for high throughput cloning and expression screening of membrane proteins from Mycobacterium tuberculosis. *BMC biotechnology* **8**, 51
16. Kabsch, W. (2010) Integration, scaling, space-group assignment and post-refinement. *Acta Crystallographica Section D: Biological Crystallography* **66**, 133-144
17. Winn, M. D., Ballard, C. C., Cowtan, K. D., Dodson, E. J., Emsley, P., Evans, P. R., Keegan, R. M., Krissinel, E. B., Leslie, A. G., and McCoy, A. (2011) Overview of the CCP4 suite and current developments. *Acta Crystallographica Section D: Biological Crystallography* **67**, 235-242
18. Evans, P. (2006) Scaling and assessment of data quality. *Acta Crystallographica Section D: Biological Crystallography* **62**, 72-82
19. McCoy, A. J., Grosse-Kunstleve, R. W., Adams, P. D., Winn, M. D., Storoni, L. C., and Read, R. J. (2007) Phaser crystallographic software. *Journal of applied crystallography* **40**, 658-674
20. Matthews, B. W. (1968) Solvent content of protein crystals. *Journal of molecular biology* **33**, 491-497
21. Langer, G., Cohen, S. X., Lamzin, V. S., and Perrakis, A. (2008) Automated macromolecular model building for X-ray crystallography using ARP/wARP version 7. *Nature protocols* **3**, 1171-1179
22. Adams, P. D., Afonine, P. V., Bunkóczi, G., Chen, V. B., Davis, I. W., Echols, N., Headd, J. J., Hung, L.-W., Kapral, G. J., and Grosse-Kunstleve, R. W. (2010) PHENIX: a comprehensive Python-based system for macromolecular structure solution. *Acta Crystallographica Section D: Biological Crystallography* **66**, 213-221
23. Emsley, P., Lohkamp, B., Scott, W. G., and Cowtan, K. (2010) Features and development of Coot. *Acta Crystallographica Section D: Biological Crystallography* **66**, 486-501
24. Chen, V. B., Arendall, W. B., Headd, J. J., Keedy, D. A., Immormino, R. M., Kapral, G. J., Murray, L. W., Richardson, J. S., and Richardson, D. C. (2010) MolProbity: all-atom structure validation for macromolecular crystallography. *Acta Crystallographica Section D: Biological Crystallography* **66**, 12-21
25. McNicholas, S., Potterton, E., Wilson, K., and Noble, M. (2011) Presenting your structures: the CCP4mg molecular-graphics software. *Acta Crystallographica Section D: Biological Crystallography* **67**, 386-394
26. Swearingen, C., Wu, J., Stucki, J., and Fitch, A. (2004) Use of ferrocenyl surfactants of varying chain lengths to study electron transfer reactions in native montmorillonite clay. *Environmental science & technology* **38**, 5598-5603
27. Bradford, M. M. (1976) A rapid and sensitive method for the quantitation of microgram quantities of protein utilizing the principle of protein-dye binding. *Analytical biochemistry* **72**, 248-254
28. Van Gelder, B., and Slater, E. (1962) The extinction coefficient of cytochrome c. *Biochimica et biophysica acta* **58**, 593-595

29. Mayhew, S. G., Petering, D., Palmer, G., and Foust, G. P. (1969) Spectrophotometric titration of ferredoxins and Chromatium high potential iron protein with sodium dithionite. *Journal of Biological Chemistry* **244**, 2830-2834
30. Naro, F., Tordi, M. G., Giacometti, G. M., Tomei, F., Timperio, A. M., and Zolla, L. (2000) Metal binding to Pseudomonas aeruginosa azurin: a kinetic investigation. *Zeitschrift für Naturforschung C* **55**, 347-354
31. Wilson, E. K., Mathews, F., Packman, L. C., and Scrutton, N. S. (1995) Electron tunneling in substrate-reduced trimethylamine dehydrogenase: Kinetics of electron transfer and analysis of the tunneling pathway. *Biochemistry* **34**, 2584-2591
32. Lehman, T. C., Hale, D. E., Bhala, A., and Thorpe, C. (1990) An acyl-coenzyme A dehydrogenase assay utilizing the ferricenium ion. *Analytical biochemistry* **186**, 280-284
33. Moore, J., and Ward, W. (1956) Cross-linking of bovine plasma albumin and wool keratin. *Journal of the American Chemical Society* **78**, 2414-2418
34. Liu, G., Abramson, J. J., Zable, A. C., and Pessah, I. N. (1994) Direct evidence for the existence and functional role of hyperreactive sulfhydryls on the ryanodine receptor-triadin complex selectively labeled by the coumarin maleimide 7-diethylamino-3-(4'-maleimidylphenyl)-4-methylcoumarin. *Molecular pharmacology* **45**, 189-200
35. Zhang, Y., and Skolnick, J. (2005) TM-align: a protein structure alignment algorithm based on the TM-score. *Nucleic acids research* **33**, 2302-2309
36. Basran, J., Jang, M.-H., Sutcliffe, M. J., Hille, R., and Scrutton, N. S. (1999) The role of Tyr-169 of trimethylamine dehydrogenase in substrate oxidation and magnetic interaction between FMN cofactor and the 4Fe/4S center. *Journal of Biological Chemistry* **274**, 13155-13161
37. Lim, L., Shamala, N., Mathews, F., Steenkamp, D., Hamlin, R., and Xuong, N. H. (1986) Three-dimensional structure of the iron-sulfur flavoprotein trimethylamine dehydrogenase at 2.4-A resolution. *Journal of Biological Chemistry* **261**, 15140-15146
38. Diederichs, K., and Karplus, P. A. (1997) Improved R-factors for diffraction data analysis in macromolecular crystallography. *Nature structural biology* **4**, 269-275
39. Weiss, H., Hampel, F., Donaubauer, W., Grundl, M. A., Bats, J. W., Hashmi, A. S. K., and Schindler, S. (2001) The First Crystal Structure of a Nickel Cyclopropene Complex. *Organometallics* **20**, 1713-1715
40. Karplus, P. A., and Diederichs, K. (2012) Linking crystallographic model and data quality. *Science* **336**, 1030-1033
41. Axford, D., Owen, R. L., Aishima, J., Foadi, J., Morgan, A. W., Robinson, J. I., Nettleship, J. E., Owens, R. J., Moraes, I., and Fry, E. E. (2012) In situ macromolecular crystallography using microbeams. *Acta Crystallographica Section D: Biological Crystallography* **68**, 592-600
42. Henriksson, G., Johansson, G., and Pettersson, G. (2000) A critical review of cellobiose dehydrogenases. *Journal of biotechnology* **78**, 93-113
43. Myer, Y. P., Saturno, A. F., Verma, B., and Pande, A. (1979) Horse heart cytochrome c. The oxidation-reduction potential and protein structures. *Journal of Biological Chemistry* **254**, 11202-11207

44. Tagawa, K., and Arnon, D. I. (1968) Oxidation-reduction potentials and stoichiometry of electron transfer in ferredoxins. *Biochimica et Biophysica Acta (BBA)-Bioenergetics* **153**, 602-613
45. Gray, H. B., Malmström, B. G., and Williams, R. (2000) Copper coordination in blue proteins. *JBIC Journal of Biological Inorganic Chemistry* **5**, 551-559
46. Sanchís, C., Salavagione, H. J., and Morallón, E. (2008) Ferrocenium strong adsorption on sulfonated polyaniline modified electrodes. *Journal of Electroanalytical Chemistry* **618**, 67-73
47. Neghmouche, N., and Lanez, T. (2013) Electrochemical properties of ferrocene in aqueous and organic mediums at glassy carbon electrode. *Recent Trends in Physical Chemistry: An International Journal* **1**, 1-3
48. Signor, L., and Erba, E. B. (2013) Matrix-assisted laser desorption/ionization time of flight (MALDI-TOF) mass spectrometric analysis of intact proteins larger than 100 kDa. *JoVE (Journal of Visualized Experiments)*, e50635
49. Trickey, P., Basran, J., Lian, L.-Y., Chen, Z.-w., Barton, J. D., Sutcliffe, M. J., Scrutton, N. S., and Mathews, F. S. (2000) Structural and biochemical characterization of recombinant wild type and a C30A mutant of trimethylamine dehydrogenase from Methylophilus methylotrophus (sp. W3A1). *Biochemistry* **39**, 7678-7688
50. Walsh, J. D., and Miller, A.-F. (2003) Flavin reduction potential tuning by substitution and bending. *Journal of Molecular Structure: THEOCHEM* **623**, 185-195
51. Ghisla, S., Massey, V., Lhoste, J.-M., and Mayhew, S. G. (1974) Fluorescence and optical characteristics of reduced flavines and flavoproteins. *Biochemistry* **13**, 589-597
52. Kar, R. K., Miller, A. F., and Mroginski, M. A. (2021) Understanding flavin electronic structure and spectra. *Wiley Interdisciplinary Reviews: Computational Molecular Science*, e1541
53. Haynes, C. A., Koder, R. L., Miller, A.-F., and Rodgers, D. W. (2002) Structures of nitroreductase in three states: effects of inhibitor binding and reduction. *Journal of Biological Chemistry* **277**, 11513-11520
54. Lyubimov, A. Y., Heard, K., Tang, H., Sampson, N. S., and Vrielink, A. (2007) Distortion of flavin geometry is linked to ligand binding in cholesterol oxidase. *Protein Science* **16**, 2647-2656
55. Li, X.-L., and Fu, Y. (2008) Theoretical study of reduction potentials of substituted flavins. *Journal of Molecular Structure: THEOCHEM* **856**, 112-118
56. Tsutsumi, M., Fujieda, N., Tsujimura, S., Shirai, O., and Kano, K. (2008) Thermodynamic redox properties governing the half-reduction characteristics of histamine dehydrogenase from Nocardioides simplex. *Bioscience, biotechnology, and biochemistry* **72**, 786-796
57. Pace, C. P., and Stankovich, M. T. (1991) Oxidation-reduction properties of trimethylamine dehydrogenase: effect of inhibitor binding. *Archives of biochemistry and biophysics* **287**, 97-104
58. Barber, M. J., Pollock, V., and Spence, J. T. (1988) Microcoulometric analysis of trimethylamine dehydrogenase. *Biochemical Journal* **256**, 657-659
59. Werther, T., Wahlefeld, S., Salewski, J., Kuhlmann, U., Zebger, I., Hildebrandt, P., and Dobbek, H. (2017) Redox-dependent substrate-cofactor interactions in the Michaelis-complex of a flavin-dependent oxidoreductase. *Nature communications* **8**, 1-8

60. Murthy, Y. V., and Massey, V. (1998) Synthesis and properties of 8-CN-flavin nucleotide analogs and studies with flavoproteins. *Journal of Biological Chemistry* **273**, 8975-8982
61. Bonomi, F., and Iametti, S. (2021) Redox titration of flavoproteins: An overview. *Flavins and Flavoproteins*, 119-133
62. Anusevičius, Ž., Misevičienė, L., Medina, M., Martinez-Julvez, M., Gomez-Moreno, C., and Čėnas, N. (2005) FAD semiquinone stability regulates single-and two-electron reduction of quinones by Anabaena PCC7119 ferredoxin: NADP+ reductase and its Glu301Ala mutant. *Archives of biochemistry and biophysics* **437**, 144-150
63. Kılıç, M., and Ensing, B. (2013) First and Second One-Electron Reduction of Lumiflavin in Water · A First Principles Molecular Dynamics Study. *Journal of Chemical Theory and Computation* **9**, 3889-3899
64. Senda, T., Senda, M., Kimura, S., and Ishida, T. (2009) Redox control of protein conformation in flavoproteins. *Antioxidants & redox signaling* **11**, 1741-1766
65. Zheng, Y.-J., and Ornstein, R. L. (1996) A theoretical study of the structures of flavin in different oxidation and protonation states. *Journal of the American Chemical Society* **118**, 9402-9408
66. Dixon, D., Lindner, D., Branchaud, B., and Lipscomb, W. (1979) Conformations and electronic structures of oxidized and reduced isoalloxazine. *Biochemistry* **18**, 5770-5775
67. Basran, J., Chohan, K. K., Sutcliffe, M. J., and Scrutton, N. S. (2000) Differential coupling through Val-344 and Tyr-442 of trimethylamine dehydrogenase in electron transfer reactions with ferricenium ions and electron transferring flavoprotein. *Biochemistry* **39**, 9188-9200

Chapter 3. Active Site Residues Critical to Substrate Inhibition of Bacterial Histamine Dehydrogenase

3.1 Abstract

Histamine dehydrogenase from the gram-negative bacterium *Rhizobium sp. 4-9* (HaDHR) is a member of a small family of dehydrogenases containing a covalently attached FMN, and the only member so far identified that does not exhibit substrate inhibition. In this study, the structure of HaDHR solved to a resolution of 2.1 Å in Chapter 2, was compared to that of the closely related (~55% identity) histamine dehydrogenase from *Nocardioides simplex* (HaDHN). The backbone structures aligned well with an overall RMSD of 1.10 Å. Comparison of the active sites suggested that substrate inhibition of HaDHN can be explained by the difference in orientation of a single aromatic residue (Phe176 in HaDHR; Tyr181 in HaDHN). The hydroxyl of Tyr181 (HaDHN) forms a hydrogen bond with a proximal Asp136, promoting a π-stacking interaction between the tyrosine aromatic ring and the imidazole ring of histamine modeled into the active site. Both positions in HaDHR are occupied by Phe residues, precluding the hydrogen bonding interaction and allowing Phe176 (HaDHR) to adopt a conformation that is more favorable for catalysis. A double mutant of HaDHR, F176Y/F131D, designed to mimic the HaDHN active site, resulted in ~50% reduction in kcat. Based upon our analysis of the docking studies, HaDHR is found to be better poised to support hydride transfer from the histamine substrate, but the overall rate of electron transfer is better optimized in HaDHN. Note that hydride trasnfer and electron transfer are bothe elements of the catalytic process, and that neither are fully optimized. Short molecular dynamic simulations of the two wildtype enzymes and the HaDHR double mutant suggested that forming the hydrogen bond between the Tyr and Asp residues promotes ring stacking with substrate and results in an inhibited conformational state of the bound substrate.

3.2 Introduction

The *Rhizobium sp.4-9* histamine dehydrogenase (HaDHR, UniProtKB: Q60I59_9RHIZ, RCSB: 6DE6) is a member of a small family of oxidoreductases (Figure 3-1) that are responsible for the catabolism of low molecular weight amines. The enzymes are typically homodimeric, contain a covalently attached 6-S cysteinyl flavin mononucleotide (FMN), an Fe_4S_4 cluster, and with the exception of HaDHR, exhibit substrate inhibition (1). Other family members include a related histamine dehydrogenase enzyme from *Nocardioides simplex* (HaDHN, UniProtKB: Q6IWJ5_NOCSI, RCSB:3K30), trimethylamine dehydrogenase (TAMDH, UniProtKB: P16099_METME, RCSB:1DJN) from *Methylophilus methylotrophus* and dimethylamine dehydrogenase from *Hyphomicrobium sp. (strain x)* (DMADH, UniProtKB: Q48303_HYPSX) (2-6). Members of this family continue to be of interest as model systems for biological electron transfer (7) due to the presence of multiple redox-active sites, i.e., covalently bound flavin, and the Fe_4S_4 cluster (8-10). The redox properties of these enzymes are also of interest for use as the biological recognition element in the construction of an amperometric biosensor, wherein the enzyme may support the direct electron transfer to the biosensor's transduction element (11-14).

The substrate inhibition observed for HaDHN, TMADH and DMADH has limited their use for non-biological applications (11,13-15). The mechanism of substrate inhibition for HaDHN and TMADH has been examined in detail (16,17). Even though loss of substrate inhibition for both enzymes was observed by mutating active site residues to be similar to HaDHR, no consensus structural basis for substrate inhibition has emerged (16,17). HaDHR has ~55% sequence homology with HaDHN, and ~38% sequence homology with TMADH and DMADH which is relatively low given the overall functional homology of the family. Until now, the lack of a high-resolution X-ray structure of HaDHR has precluded a detailed comparison with other family

members, most especially HaDHN, which is its closest homolog (18-20). We discussed the crystal structure of HaDHR in Chapter 2, where we identified the key residues involved in electron transfer to artificial mediators. A detailed analysis of the crystal structure of HaDHR and HaDHN has allowed us to investigate the structural basis for the lack of substrate inhibition in HaDHR and further refine the structural model of substrate inhibition in other family members.

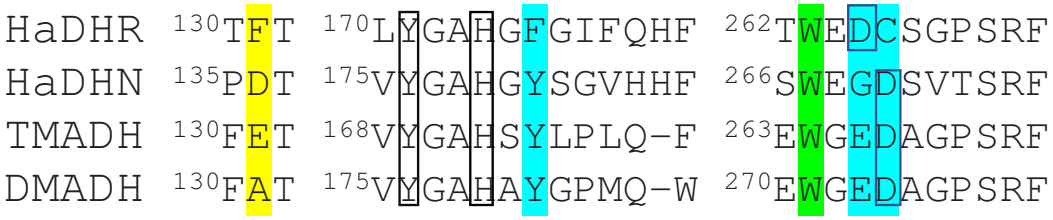

Figure 3-1 Key sequence alignments for enzyme family members.
Alignment of partial sequences from histamine dehydrogenases from *Rhizobium sp.4-9* (HaDHR), *Nocardiodes simplex* (HaDHN) and trimethylamine (TMADH) and dimethylamine (DMADH) dehydrogenases from *Methylophilus methylotrophus* and *Hyphomicrobium sp.* respectively. Residues considered important for substrate inhibition are highlighted in cyan (9). Residues proposed to be involved in a putative catalytic triad are boxed. Conserved tryptophan that forms part of the substrate-binding hydrophobic bowl is shown in green. The residue proposed to be forming a hydrogen bond to Tyr181 in HaDHN and likely responsible for the presence of substrate inhibition in HaDHN is highlighted in yellow along with the aligned residues in other enzymes.

The kinetic properties of HaDHR are similar to those of HaDHN even though the *Nocardioides* enzyme is inhibited by histamine with an apparent K_i of ~580 μM. Based on sequence alignments and homology modeling, Tsutsumi *et al*. (17), identified three important differences between HaDHN and HaDHR within an otherwise highly conserved region near the substrate binding site previously identified in the homologous TMADH structure (Figure 3-1). Tsutsumi reasoned that one or more of these residues were likely responsible for conferring substrate inhibition. Mutant forms of the HaDHN were prepared to test this hypothesis by substituting the three residues for their spatial homologs from HaDHR; Y181F, the double mutant G269D/D270C, and the triple mutant, Y181F/G269D/D270C (positions 176, 265 and 266 respectively in HaDHR). The single Y181F mutation significantly reduced substrate inhibition, increasing the apparent K_i for histamine from $5.8x10^2$ μM to $8.3x10^2$ μM. By contrast, the triple mutant completely abolished substrate inhibition, but resulted in an enzyme with a 40% lower V_{max} and a 5-fold higher apparent K_M (17). A single Y169F mutation in TMADH essentially eliminated substrate inhibition (21).

The subsequent solution of the three-dimensional structure of HaDHN at 2.7 Å resolution, together with substrate docking studies, suggested that Tyr181 is directly involved in substrate binding by engaging in a π-stacking interaction with the imidazole ring of histamine (19). The structure analysis of HaDHN did not provide insights into the role of Gly269 and Asp270 in substrate inhibition. The side chains of these residues do not contact the substrate directly and are located within a short helical element proximal to the FMN moiety. Based on the structure, Asp270 seems to interact with the phosphoribosyl moiety of FMN.

A distinguishing feature of this family of enzymes is the covalently attached FMN cofactor that is involved in catalyzing the oxidation chemistry of the bound substrate. For HaDHR and HaDHN,

the substrate is histamine. The geometry of the isoalloxazine ring, the part of the cofactor involved in electron transfer, has a bearing on the rate of oxidation of histamine.

The structure of FMN consists of three main parts, the isoalloxazine ring, the ribitol group and a phosphate as shown in Figure 3-2. The isoalloxazine ring of FMN has three different states: a hydroquinone state where the flavin is reduced directly to its two-electron reduced form, or the semiquinone state where the flavin is reduced by one electron, and an oxidized state (Figure 3-2). In oxidized form the flavin ring is usually in a planar form whereas in the reduced state the geometry of the flavin ring is typically bent (22). Studies have suggested that bending of the isoalloxazine ring favors reduction to the fully reduced form. Thus, the bend of the isoalloxazine ring dominates the chemistry of the cofactor. In Chapter 2 of this dissertation, we discussed our structural analysis of the isoalloxazine rings in HaDHR and HaDHN. In both crystal structures, the isoalloxazine ring is bent, with HaDHR displaying only ~1° more bending than that observed in HaDHN.

The geometry of the isoalloxazine ring has a bearing on substrate binding and substrate inhibition, but the changes in geometry of the cofactor are only part of a more complex set of interactions that control substrate interactions in the active site. For example, studies on cholesterol oxidase showed that in the substrate bound crystal structure, the flavin geometry is distorted upon substrate binding, thereby affecting the catalysis (23). This study also showed that the aromatic residues around the flavin also affect the geometry of the cofactor and play a role in controlling the oxidation-reduction state of flavin. Overall, the way substrate binds and interacts at the active site, and the aromatic residues surrounding the flavin all contribute to regulating the oxidation state of the flavin. In turn, these interactions all play a role in regulating any substrate concentration dependent inhibition mechanisms.

Studies designed to characterize the isoalloxazine ring redox chemistry can be difficult to perform and require advanced techniques such as electron paramagnetic resonance spectroscopy (EPR), stopped-flow kinetic analyses, changes in geometry as revealed by crystallography, Raman spectroscopy and UV-vis spectroscopy. Many of these techniques have been used to probe the active sites of the HaDHR enzyme family. In this Chapter, we have relied heavily on UV-vis spectroscopy and the associated spectral signatures of the different oxidation states of FMN. We were able to leverage the previous studies on the relationship between the spectroscopic signatures and the observed catalysis to allow us to develop a model for the comparison of the geometry of the isoalloxazine ring and the lack of substrate inhibition in HaDHR with HaDHN.

For the purpose of this Dissertation Chapter, we will use the current IUPAC nomenclature for the individual atoms in histamine as shown in Figure 3-3 (24).

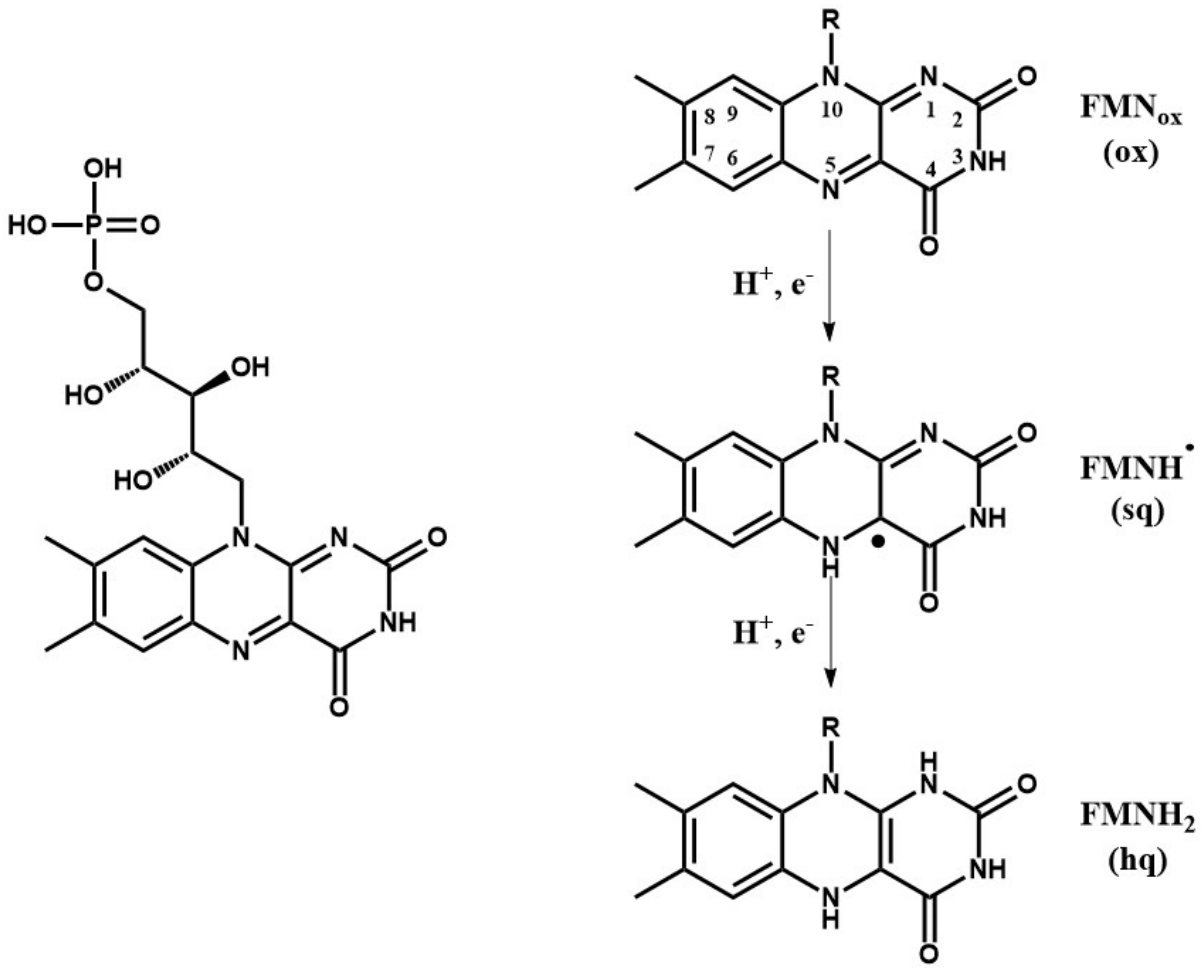

Figure 3-2 The structure of FMN and different states
The isoalloxazine ring of FMN has three different states: a hydroquinone (hq) state where the flavin is reduced to its two-electron reduced form, or the semiquinone (sq) state where the flavin is reduced to its one-electron reduced state, and the oxidized (ox) state. The "R" group is as shown in the diagram on the left.

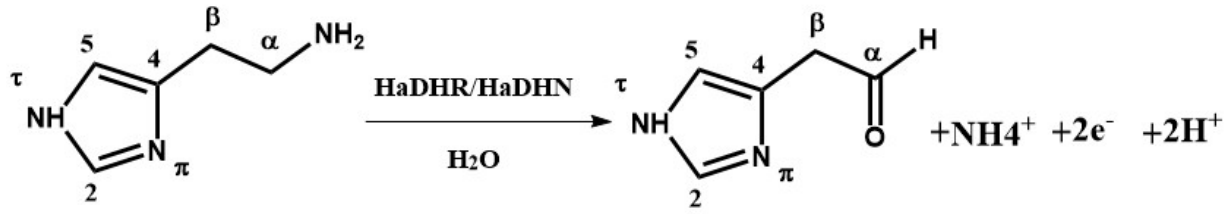

Figure 3-3 IUPAC labelling of histamine backbone.
Oxidative deamination pathway of histamine catalyzed by histamine dehydrogenases (HaDHR/HaDHN). Atom labels of histamine, as shown, conform to the latest IUPAC recommendations (24). Histamine gets converted to imidazole acetaldehyde, ammonia with a release of two electrons.

The work reported in this Chapter provides new insights as to why HaDHR lacks substrate inhibition in contrast to other family members, especially HaDHN. The lack of substrate inhibition in HaDHR makes this enzyme an unique member of its family and makes it suitable for use in histamine biosensing applications. Alignment and comparison of the crystal structures of HaDHR and HaDHN revealed several differences in the active sites (Figures 3-4 and 3-5). Among the key differences, is the availability of an active site aromatic residue in HaDHN, Tyr181 which forms a hydrogen bond with Asp136.

The presence of Tyr181-Asp136 hydrogen bond in HaDHN, resulted in a marked difference in the orientation of the lowest energy docked histamine structure. By contrast, the homologous residue in HaDHR (Phe176) is not able to form a hydrogen bond. While Tsutsumi *et al.* observed that it is possible to reduce or remove substrate inhibition in HaDHN and TMADH with simple mutations that are "HaDHR-like" (17), we were unable to introduce substrate inhibtion in HaDHR by introducing "HaDHN-like" mutations (Table 3-1). These insights, built upon the work of Tsutsumi *et al*, provide a better understanding of why these two enzymes behave differently even though their backbone structures align closely with one another (T_m align score= 0.98, RMSD=1.10 Å) (25).

3.3 Experimental procedures

3.3.1 Materials

Histamine, carbenicillin, chloramphenicol, Sephadex G-50 resin, and bilirubin oxidase were purchased from Sigma Aldrich. Ferrocenedimethanol was purchased from Santa Cruz Biotechnology, and Ni-NTA resin was purchased from Qiagen. DNaseI was purchased from Roche. The primers used in this study were obtained from Integrated DNA Technologies.

3.3.2 Gene constructs and mutagenesis

DNA encoding the full-length histamine dehydrogenase enzyme from *Rhizobium sp.* 4-9 (protein_id="BAD54700.1") were obtained from Integrated DNA technologies. The genes were cloned into the pMCSG7 vector (26), which incorporated a His_6 tag on the N-terminus of the protein followed by a tobacco etch virus (TEV) cleavage site, using a ligation independent cloning method (27). The resulting plasmid was transformed into competent *E.coli* XL10 Gold cells (Agilent Technologies) and the sequence was confirmed by Sanger sequencing (ACGT Inc.).

DNA encoding the F176Y mutant enzyme was generated by introducing the mutation in the *wt*-HaDHR expression plasmid ORF by using the Quick-change site directed mutagenesis kit (Agilent Technologies). The F176Y/F131D double mutant and the F176Y/D256G/C266D triple mutant were prepared by using F176Y mutant plasmid DNA as a template using the Quick-change method. The T130P/F176Y/F131D triple mutant was prepared in the similar manner by using F176Y/F131D plasmid DNA as the template. Plasmid DNA was purified from transformant colonies, and the mutations were validated by Sanger sequencing (ACGT Inc.).

3.3.3 Protein expression and purification

The plasmid was transformed into the expression host *E. coli* BL21 (DE3)/pLysS and an isolated colony was inoculated in a 10 mL Luria Bertoni (LB) starter culture supplemented with carbenicillin (100 µg/mL) and chloramphenicol (34 µg/mL). The culture was then incubated overnight in a shaker incubator (37 °C/250 rpm). Large scale expression was performed by inoculating the overnight 10 mL culture into 1L LB supplemented with carbenicillin (100 µg/mL). Cultures were grown in a shaker incubator (37 °C/250 rpm) until the OD_{600} reached ~0.6-0.8. The enzyme expression was induced with the addition of isopropylthiogalactoside to 0.1 mM and the incubator temperature was reduced to 15 °C. Expression was allowed to proceed overnight for ~22 h. Cell pellets were harvested by centrifugation at 5,000 x g for 10 min, resuspended in 80 mL of lysis buffer (50 mM potassium phosphate, pH 7.4, 5 mM imidazole) and frozen at -80 °C overnight. The cell suspension was thawed, 5 U/mL of DNaseI was added, and the suspension sonicated for 2 min in an ice water bath using an alternating 8 sec on/8 sec off duty cycle in using a Branson 400-Watt sonicator. Insoluble material was removed by centrifugation at 20,000 x g for 60 min at 4 ºC. The soluble cell fraction was applied to a 3 mL NiNTA column equilibrated with binding buffer (50 mM potassium phosphate, pH 7.4, 0.15 M NaCl and 5 mM imidazole). The column was washed with 20 column volumes of binding buffer supplemented with 15 mM imidazole and the protein was eluted with binding buffer supplemented with 245 mM imidazole. Glycerol was added to 20% (v/v) and the protein was snap-frozen and stored at -80 ºC. Gel electrophoresis was performed on pre-cast NuPage® 12% acrylamide gels (Invitrogen) under reducing conditions. At this stage the enzyme was estimated to be >95% pure as judged by SDS-polyacrylamide gel electrophoresis.

3.3.4 Steady-state kinetic assays

The rate of reduction of ferriceniumdimethanol (Fc^+-DM) was followed. Ferrocenedimethanol was oxidized to (Fc^+-DM) before use by treatment with bilirubin oxidase as follows: 100 µL of bilirubin oxidase (1 mg/mL) were added to 5 mM of Fc-DM in 0.2 M air saturated potassium phosphate buffer, pH 5.8 and formation of Fc^+-DM was followed as an increase in absorption at 640 nm (28). The reaction was continued until the reduction was complete as indicated by the change in color of the ferrocene solution from yellow to blue. The pH of the solution was reduced to 2.5 by addition of HCl to denature and inactivate the bilirubin oxidase then returned to pH 7.4 by adding 1M NaOH.

Steady state kinetic assays were performed in a 1 mL reaction volume comprised of 100 mM potassium phosphate buffer, pH 7.4, HaDHR (0.25 µM), varying histamine concentrations (1 µM-2mM) and Fc^+DM (2.5 mM). Fc^+DM reduction was followed in a Cary-50 UV Spectrophotometer at 640 nm at 25 ºC. The initial optical velocities of the assays was determined by linear regression fit to the kinetics data. The chemical velocities of the reactions were calculated by dividing the optical velocities by the extinction coefficient of Fc^+-DM (ΔA_{640} = 241 M^{-1} cm^{-1}). The unimolecular rate of turnover (k_{obs} s^{-1}) at each histamine concentration was determined by dividing the total enzyme concentration. The kinetic data were fit by a non-linear regression to the Michaelis-Menten equation. k_{cat} and K_M are reported in Table 3-1. Protein concentrations were determined using the average of three Bradford assays (29).

3.3.5 UV-vis spectroscopy

Measurements were performed with UV-plastic cuvettes of a 1cm light path at a final volume of 1 mL at room temperature. UV-vis spectra were obtained on a Cary 50 UV-vis spectrophotometer (Agilent Technologies, Varian Inc.). The scan was performed from 200 nm-800 nm. *wt*-HaDHR

and the mutant solutions were prepared at a concentration of 5 μM in 100 mM potassium phosphate buffer, pH 7.4. The spectra of the reduced forms were taken by adding 100 μM of histamine to each sample.

3.3.6 Histamine docking

Substrate docking was performed using the Molecular Operating Environment (MOE) software from the Chemical Computing Group (30). The crystal structures of HaDHR (RCSB: 6DE6) and HaDHN (RCSB: 3K30) were used as the starting scaffolds for ligand docking. The structures of the unprotonated form and the α-N protonated form of histamine were created *in silico* using MOE and optimized *in vacuo* using the Merck force field (30). Both forms of histamine were docked into the active site of HaDHR, whereas only the protonated form of histamine was docked into the HaDHN active site. Reed *et al.* had previously shown that the unprotonated form of histamine bound with a higher overall energy in HaDHN compared to the protonated form of the ligand (19) and was not examined in this study.

Substrate docking by MOE was initiated by manually placing the histamine form to be examined into the active site proximal to the oxidized form of the isoalloxazine ring of the FMN cofactor. A spherical search grid, centered at the manually placed substrate, was defined by selecting enzyme atoms within 4.5 Å of the substrate and the selection was expanded to include the whole residue side chains. A wall potential was applied to the search grid to bias the docking routine towards poses where the substrate is proximal to the isoalloxazine ring of the FMN cofactor (30). Atomic charges were assigned using the Merck force field implemented by MOE.

The docking algorithm randomly generated multiple substrate poses which were scored using the affinity ΔG scoring function in MOE. The resulting conformations were then categorized from the best fit (lowest binding energy) to poorest fit (highest binding energy). The structures of the ten

lowest energy substrate-enzyme complexes were then minimized using the Merck force field. A single conformation emerged that had the lowest energy and where the substrate was in a catalytically competent conformation so that the hydride could be transferred from histamine (Figure 3-3) to the proximal N5 of the isoalloxazine ring of the FMN cofactor (Figure 3-2).

3.3.7 Molecular dynamic simulations

Simulations were performed using the NAMD 2.12 package (31) and CHARMM36 force field (32) for the proteins, water, and ions, and with the CHARMM general force field (33) for the histamine substrates. The FMN was simulated using the parameters described by Freddolino *et al* (34). All simulations were performed using periodic boundary conditions. The Van der Waals and the short-range electrostatics were employed with a smooth cutoff of 12 Å using a switching function starting at 10 Å. Long-range electrostatic interactions were calculated by the Particle mesh Ewald (PME) method with a grid point density of 1 per Å. Constant temperature (300 K) was enforced using Langevin dynamics with a coupling factor of 1 ps. Constant pressure was obtained using the Nosé-Hoover Langevin piston method. The TIP3P (transferable intermolecular potential with 3 points) explicit water model was used with a box size resulting in a protein box-edge distance of at least 10 Å. This resulted in an NPT ensemble, wherein the number of particles, pressure, and temperature were all constant.

Each system was first minimized by constraining the protein and relaxing the solvent for 5,000 steps. This was followed by removal of all restraints, except for the Fe_4S_4 cluster, the C6 of the FMN and the sulfur atom on Cys35 in HaDHN and Cys30 in HaDHR, for an additional 10,000 steps. Each system was then equilibrated for 2 ns, followed by a 10 ns production run with a harmonic distance restraint on the C6 carbon of FMN (Figure 3-2) and the Sγ atom of Cys35 in

HaDHN and Cys30 in HaDHR. The Fe_4S_4 cluster was treated as an unbound neutral complex with the appropriate metal Van der Waals radii.

3.4 Results

3.4.1 Active site residues involved in substrate inhibition

The organization of residues within the catalytic pocket of HaDHR is similar to that of HaDHN, and the differences are important in understanding the lack of substrate inhibition in HaDHR. The relative positions of the residues identified by Tsutsumi *et al*. (17) that contribute to substrate inhibition in HaDHN are highlighted in Figure 3-1 and shown in Figures 3-4 and 3-5.

Each member of this enzyme family has a "hydrophobic bowl" that forms part of the substrate binding pocket that is proximal to the isoalloxazine ring of the FMN cofactor. The hydrophobic bowl is anchored by a tryptophan residue that is conserved across the family (Figure 3-1). The importance of some other hydrophobic bowl residues was first identified in TMADH as important for substrate binding (35), which were subsequently thought to be distinct from the hydrophobic bowl residues important for substrate inhibition (17). This latter set of residues is highlighted in Figure 3-1 and shown in Figures 3-4 and 3-5 for HaDHR and HaDHN.

In HaDHR, the hydrophobic bowl has two phenylalanine residues that do not undergo any hydrogen bonding interactions, in contrast to TMADH and HaDHN. In HaDHN, Tyr181 (which corresponds to Phe176 in HaDHR), forms a hydrogen bond with Asp136 (which corresponds to Phe131 in HaDHR). This results in a very different side-chain orientation as compared to Phe176 and Phe131 in HaDHR (Figure 3-4). Compared to the orientation of Phe176, the sidechain of Tyr181 is different in two key aspects: first, Tyr181 shows an angular rotation of ~77^{o} around the β carbon of the aromatic ring, and second, the positioning of the aromatic ring of Phe176 is translated by 0.8 Å relative to the aromatic ring of Tyr181. Together, these side-chain interactions and orientational differences likely contribute to the lack of substrate inhibition in HaDHR.

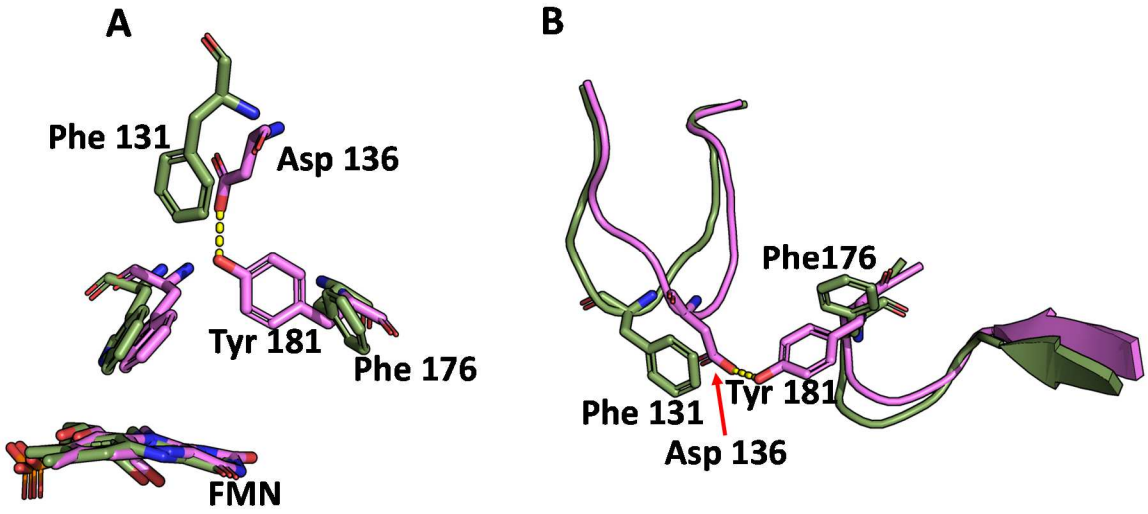

Figure 3-4 Active site residues in HaDHN and HaDHR involved in substrate inhibition. (A) In HaDHN (pink), Tyr181 forms a hydrogen bond with Asp136 relative to the isoalloxazine ring of the covalently attached FMN. The equivalent residues in HaDHR (green), Phe131 and Phe176, are more distant and do not interact in any meaningful manner. (B) In HaDHR(green)/HaDHN (pink) residues at positions 131/136 and 176/181 are both located on flexible loop segments. The hydrogen bond between Asp136-Tyr181 in HaDHN stabilizes the sidechains, whereas the corresponding sidechains in HaDHR (Phe176/Phe131) are more flexible.

Figure 3-5 shows another view of the location and side-chain orientation of all residues considered to be important for substrate inhibition in HaDHN and the relationship of the corresponding residues in HaDHR (17). The conserved Trp263 in the active site is also shown in these two panels. Figure 3-5A shows the overlayed structure of the two enzymes at the active site, and Figure 3-5B shows a 90° rotated view, where the conserved Trp 263/267 is shown to be right above the FMN and the surrounding residues. Both enzymes feature a short four-residue helical element of similar conformation that interacts with the phosphoribosyl moiety of the flavin. The residues that interact with the FMN cofactor are quite distinct for HaDHR compared to other family members.

The orientation of Asp265 in HaDHR was unexpected, as sequence alignment suggested an equivalent role as for Asp270 in HaDHN (Figures 3-5C and 3-5D, respectively). Prior to this work, these Asp residues were thought to be structurally conserved among the members of this family (17). Cys266 (HaDHR) occupies the same position as Asp270 in HaDHN, the latter forming a hydrogen bond to the hydroxyl group on the C13' position of the phosphoribosyl moiety of FMN (Figure 3-2). This aspartate in TMADH was proposed to form part of the putative "catalytic triad" composed of Tyr169-His172-Asp267 (6,21) that was thought to stabilize the semiquinone form of 6-S-Cys-FMN and the reduced $[4Fe\text{-}4S]^{+}$ in TMADH (21). In HaDHR, the catalytic triad is Tyr171-His174-Cys266, which influences the geometry of the flavin and its spectral characteristics (*vide infra*).

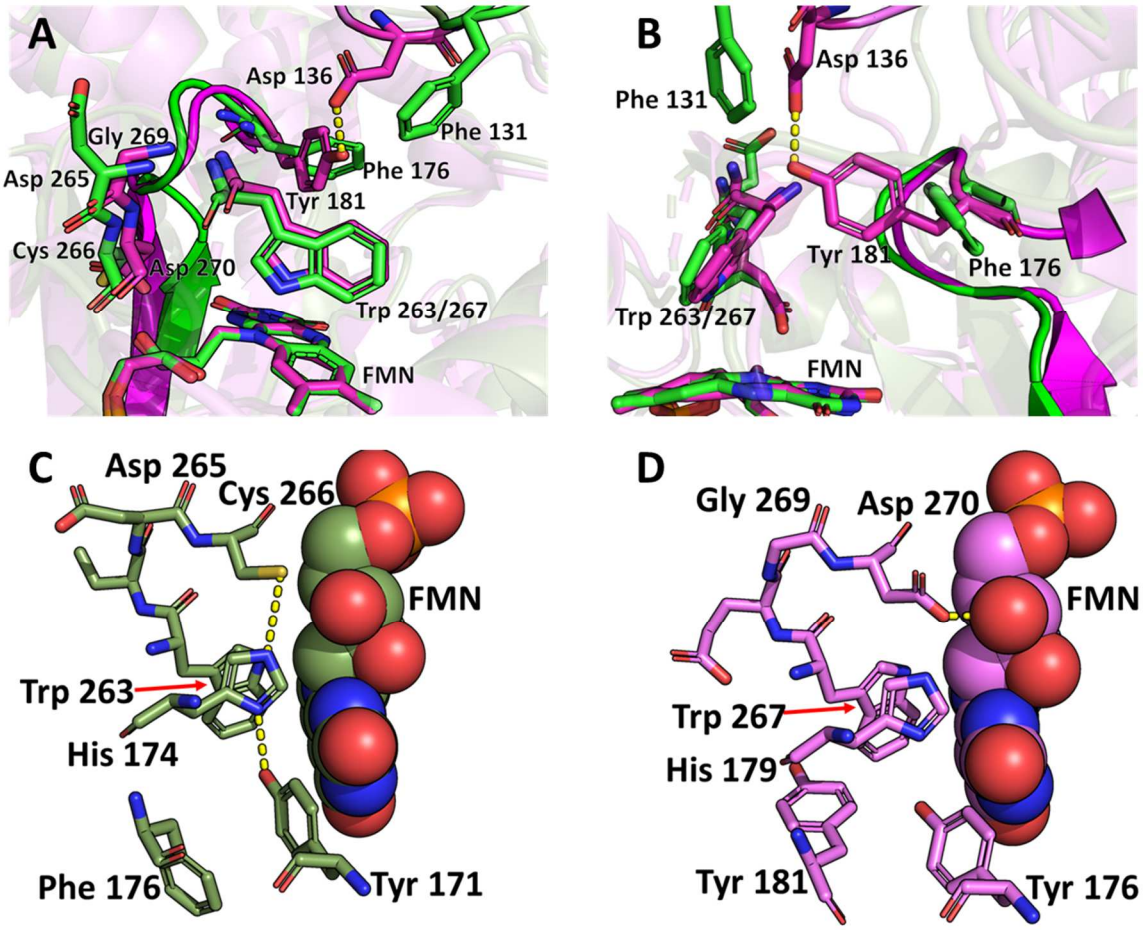

Figure 3-5 Overlay of key active site residues in HaDHR and HaDHN.
Overlayed structure of (A) HaDHR (green) and HaDHN (pink) at the active site showing all the residues involved in substrate inhibition, (B) 90° rotated view. Comparison of (C) residues Asp265 and Cys266 in HaDHR and (D) Gly269 and Asp270 in HaDHN. These residues are part of a short loop segment connecting the conserved Trp at position 263 and 267, respectively to the phosphoribosyl component of the FMN. In HaDHR the sulfhydryl moiety of Cys266 forms a hydrogen bond with His174 which also hydrogen bonds to Tyr171. In HaDHN, Asp270 forms a direct hydrogen bond to the C13' hydroxyl group of FMN.

3.4.2 The influence of HaDHN-like mutations on HaDHR kinetics

Comparison of the HaDHR and HaDHN active sites suggested that the Asp136-Tyr181 hydrogen bonding interaction in HaDHN likely plays a major role in substrate inhibition. To further probe this hypothesis, Phe176 and Phe131 in HaDHR were mutated to the corresponding Tyr and Asp residues in HaDHN. Three mutant versions of wt-HaDHR were made – a F176Y single mutant, a F176Y/F131D double mutant and a F176Y/D265G/C266D triple mutant.

The F176Y mutant was examined first to assess if just mutation to a tyrosine would be sufficient to cause substrate inhibition, presumably by causing a rotation of the tyrosine sidechain in a manner similar to that observed in HaDHN. The F131D mutant was not examined because we believed that this mutation was less important, and in the absence of a formal hydrogen bonding partner, e.g., Y176, this mutation would not be informative.

The triple mutant was designed to induce substrate inhibition to wt-HaDHR by making all the key changes suggested by Tsutsumi *et al.* (17). Indeed, this mutational study is similar to that performed by Tsutsumi *et al.* (17) that was discussed in the introduction to this Chapter. Tsutsumi *et al.* (17) showed that 50-80% of substrate inhibition could be overcome by converting Tyr181 into a phenylalanine. This mutation is reasonably expected to eliminate the key Tyr181-Asp136 hydrogen bond identified earlier (vide supra).

The results of the mutational analysis and the effects of each set of mutations on K_M (more properly referred to as K_{50} values in this study) and k_{obs} are summarized in Table 3-1 and Figure 3-6. None of the mutants showed any influence on substrate inhibition out to a histamine concentration of 2 mM. The k_{obs} of the F176Y single mutant decreased relative to that of the wt-HaDHR by ~41%, and the F176Y/F131D double mutant showed a similar decrease in k_{obs} of ~54% (Table 3-1). The apparent K_M values of the mutants increased suggesting a decreased affinity for substrate, with the

double mutant yielding a ~4-fold increase in K_M compared to *wt*-HaDHR. By contrast, the F176Y/D265G/C266D triple mutant showed a significant decrease in kobs, although the apparent K_M values were not significantly changed compared to *wt*-HaDHR The mutants were also insensitive to addition of tryptophan to a final concentration of 4 mM.

Table 3-1: $Fc^{+}DM$ reduction by HaDHR mutants.

HaDHR	$^{1}K_{50}$ (µM)	k_{obs} (s^{-1})
wt	695 ± 94.7	99.1 ± 5.9
F176Y	961 ± 56.9	58.5 ± 1.6
F176Y/F131D	2938 ± 710.0	45.9 ± 7.5
F176Y/D265G/C266D	622 ± 166.9	0.34 ± 0.04

[1]Substrate concentration giving half maximum velocity measured at 25 °C in a 100 mM potassium phosphate buffer, pH 7.4.

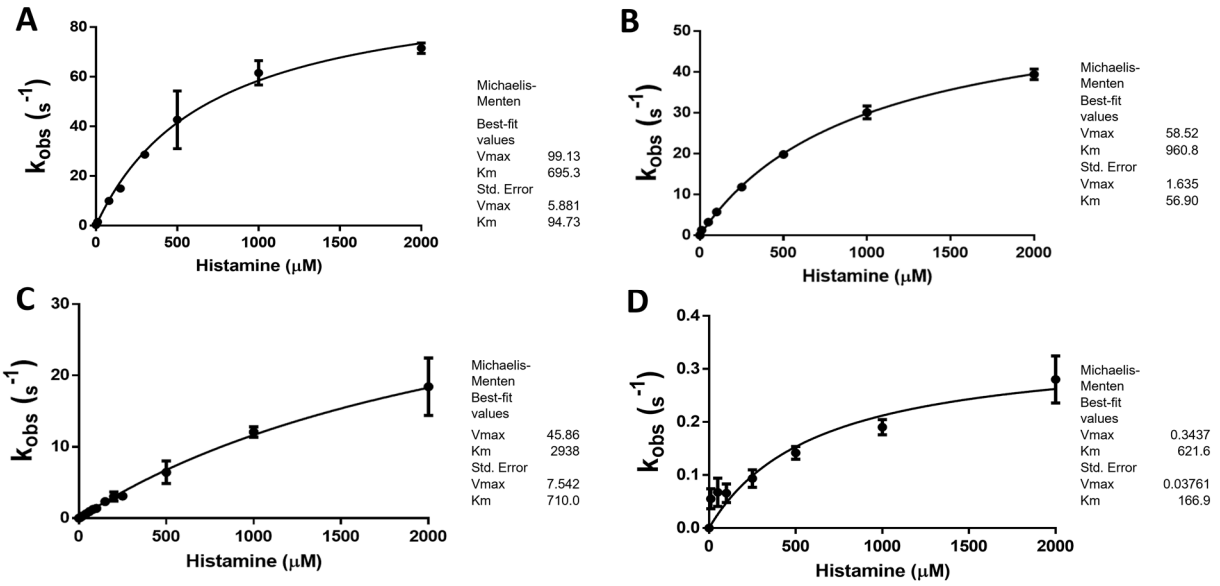

Figure 3-6 Michaelis-Menten kinetics curves for *wt*-HaDHR and mutants from Table 3-1. (A) *wt*-HaDHR, (B) HaDHR F176Y, (C) HaDHR F176Y/F131D and (D) HaDHR F176Y/D265G/C266D.

3.4.3 The effects of HaDHN-like mutations on HaDHR UV-vis spectra

The UV-vis spectra of these FMN containing enzymes can be generally recorded under oxidized conditions. FMN shows a distinct peak at 450 nm. Under substrate-reduced conditions the FMN in the semiquinone form shows a distinct peak at 365 nm. The hydroquinone form shows a more flattening peak at 365 nm (Figure 3-7). The ensuing discussion will employ the following shorthand: FMNsq and FMN_R refer to the semiquinone and reduced states of FMN, respectively, as shown in Figure 3-2. FeS_R and FeS_O refer to the reduced and oxidized states of Fe_4S_4 cluster, respectively.

Tsutsumi *et al.* detailed how flavin oxidation state affected the corresponding UV-vis spectra of substrate-reduced *wt*-HaDHN and its mutants with respect to histamine concentration (17). Tsutsumi *et al.* concluded that the spectral features at 365 nm are indicative of the existence of substrate inhibition, providing what is seemingly a simple and straightforward method to assess the role of flavin oxidation state on catalysis.

We similarly performed UV-vis studies on the wt-HaDHR and *wt*-HaDHN. The UV-Vis spectra of the substrate-reduced forms of *wt*-HaDHR and *wt*-HaDHN are different, whereas the spectra of the oxidized forms of the two enzymes were essentially equivalent (Figure 3-7). For *wt*-HaDHR, the peak at 365 nm is replaced by a "ledge" in the spectrum, where this flattening of the spectrum corresponds to a decrease of the semiquinone form of the FMN, which in turn is representative of the reaction coordinate becoming more "product" like (Figures 3-7A and 3-7B). The UV-vis spectrum for the *wt*-HaDHR was similar to that observed by Tsutsumi *et al.* for the HaDHN triple mutant, which does not show substrate inhibition, and has a flattened spectrum at 365 nm. For *wt*-HaDHN, we observed a similar distinct peak at 365 nm corresponding to an increase of the semiquinone form of the FMN (Figures 3-7C and 3-7D) as observed by Tsutsumi *et al.* (17).

A similar UV-vis spectral analysis was performed on the mutations presented in Table 3-1 (Figure 3-8). We had hypothesized that our single or double mutant UV-vis spectra would show an increase in the semiquinone formation by the presence of a distinctive peak at 365 nm. Interestingly, our single mutant (Figure 3-8A) showed similar peak like the *wt*-HaDHR in the substrate-reduced form, whereas we observed a further flattening of the 365 nm peak for our double mutant (Figure 3-8B). Similarly, we expected that the spectral signature for the F176Y/D265G/C266D triple mutant (Figure 3-8C) would correspond to the pure semiquinone state of the reduced flavin, as this is the prevalent species in *wt*-HaDHN and mutants that exhibit substrate inhibition. Interestingly, neither the semiquinone peak, a distinct feature at 365 nm, nor substrate inhibition, was observed for this mutant. The UV-vis spectra for all of the mutants in the oxidized form were similar to those observed for *wt*-HaDHR.

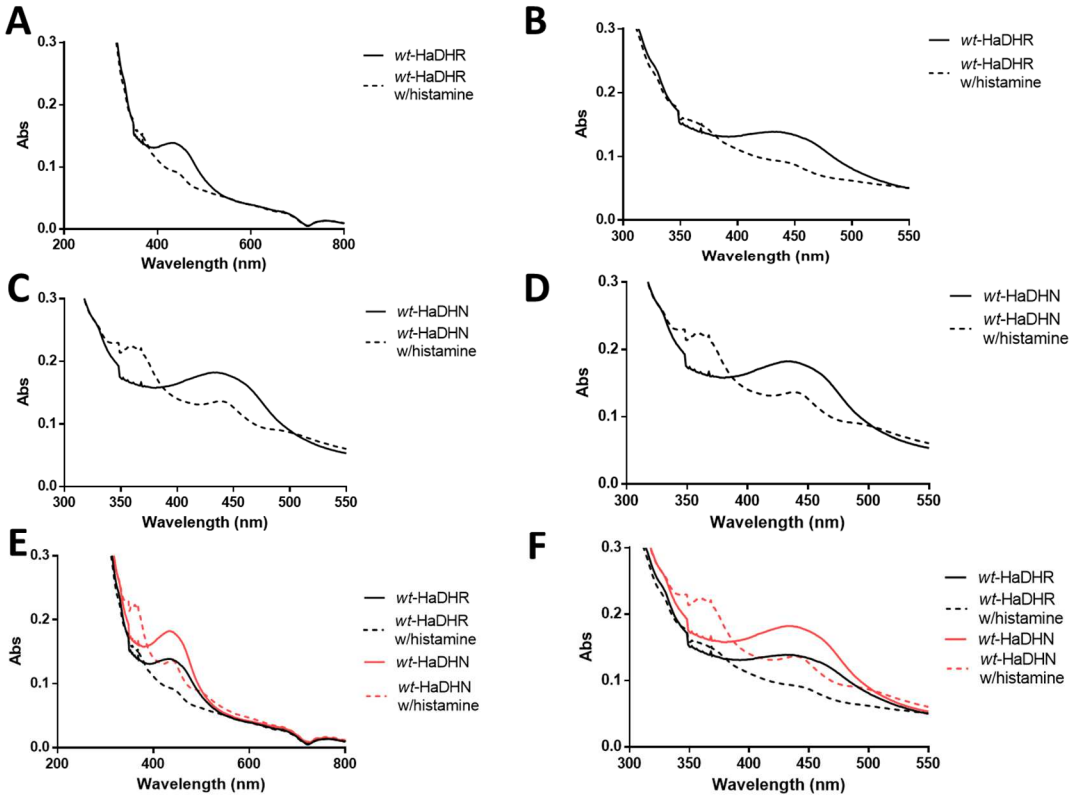

Figure 3-7 UV-vis spectra of *wt*-HaDHR and *wt*-HaDHN in absence and presence of histamine.

Peak at 450 nm corresponds to oxidized form of FMN and peak at 365 nm corresponds to semiquinone form of FMN. (A) and (B) *wt*-HaDHR and *wt*-HaDHR w/histamine, (C) and (D) *wt*-HaDHN and *wt*-HaDHN w/histamine, (E) and (F) Overlayed spectra for HaDHR (black) and HaDHN (red). Spectra of oxidized-form (indicated by a solid line) and the substrate-reduced form (indicated by a dotted line) in a 100 mM potassium phosphate buffer, pH=7.4, respectively. Figure 3-7F is an expansion of Figure 3-7E, allowing for a different view of the features at 365 nm.

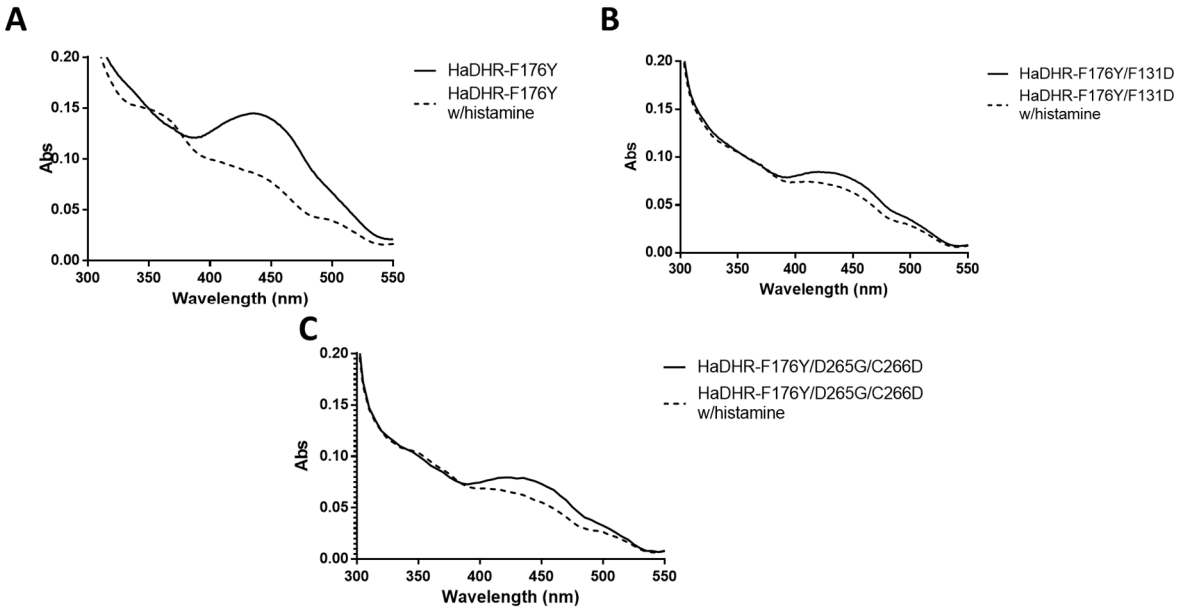

Figure 3-8 UV-vis spectra of HaDHR mutants from Table 3-1.
(A) HaDHR F176Y, (B) HaDHR F176Y/F131D and (C) HaDHR F176Y/D265G/C266D. Spectra of oxidized-form (indicated by a solid line) and the substrate-reduced form (indicated by a dotted line) in a 100 mM potassium phosphate buffer, pH=7.4, respectively.

3.4.4 Surface substrate entry channels for HaDHR and HaDHN

We further compared the surface models of the HaDHR and HaDHN (Figure 3-9) and this comparison suggested that the substrate entry channel is wider and less restricted in HaDHR (Figure 3-9A) as compared to HaDHN (Figure 3-9B). Pro135 and Asp136 in HaDHN (Thr130 and Phe131 in HaDHR) are present at the substrate entry site and together could also possibly play a role in substrate inhibition. These two residues in HaDHN seemingly occlude the channel thereby restricting the substrate entry and show some steric hindrance. We observed that the Thr130 sidechain, located at the mouth of the active site channel of HaDHR, is pulled out of the channel via a hydrogen bond to the carbonyl of Phe131.

We hypothesized that the T130P/F176Y/F131D triple mutant might also induce substrate inhibition in HaDHR. This set of mutations was designed to mimic the occlusion of the substrate entry channel in HaDHN. This HaDHR triple mutant was essentially inactive, and the UV-vis spectrum of this mutant did not show any difference between the oxidized and reduced forms of the flavin (Figure 3-10).

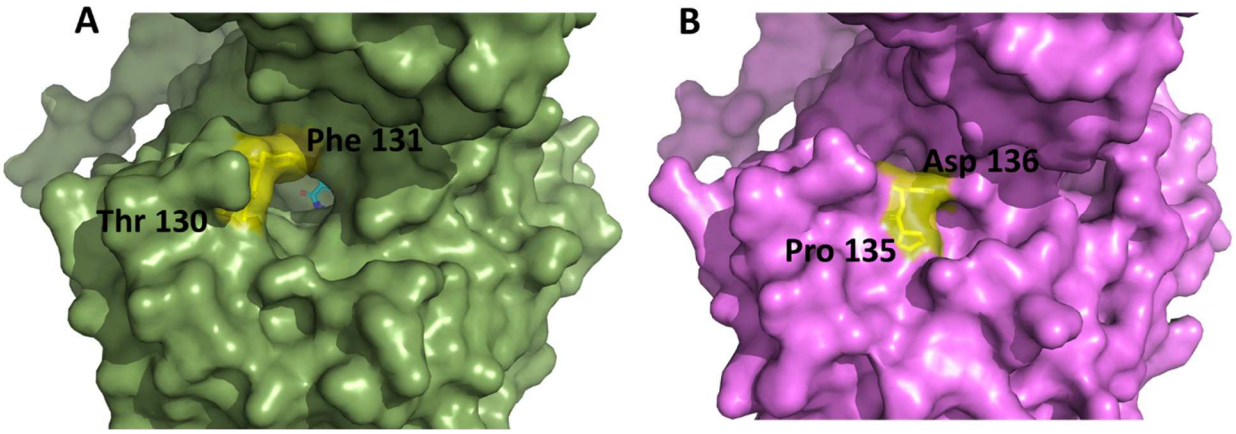

Figure 3-9 Comparison of surface model of (A) HaDHR and (B) HaDHN.
In HaDHR (green), Thr130 and Phe131 are present at the substrate entry site, whereas Pro135 and Asp136 are present at the substrate entry site in HaDHN (pink).

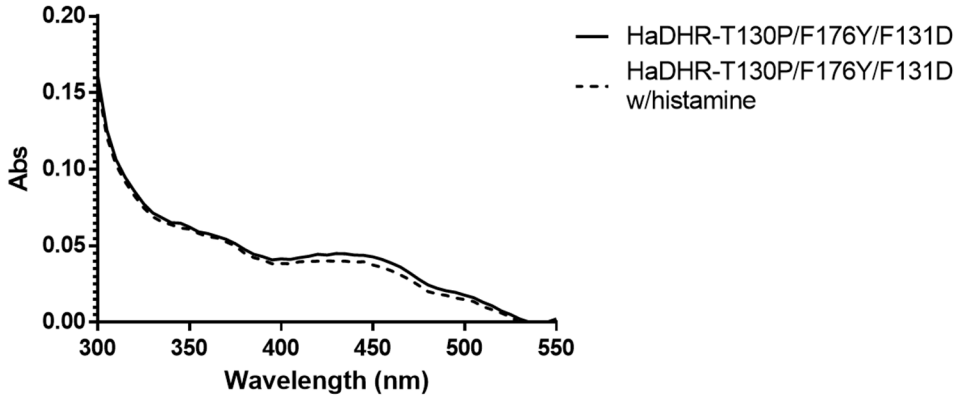

Figure 3-10 UV-vis spectra of T130P/F176Y/F131D HaDHR mutant.
Spectra of oxidized-form (indicated by a solid line) and the spectra of substrate-reduced form (indicated by a dotted line) in a 0.1M phosphate buffer, pH=7.4.

3.4.5 Histamine docking

Given that crystal structures of histamine+HaDHR/HaDHN were unavailable, docking and molecular dynamic simulations were performed to give insights into the orientation of histamine in the active site of these enzymes. The mode of binding of histamine in the active site and its influence on substrate inhibition, was studied using the MOE program suite on HaDHR and HaDHN. In the docked structure of HaDHR, the imidazole ring of histamine was found to be sandwiched between the sidechain of Trp263 and Phe176 (Figure 3-11A). In this complex, the hydride to be transferred from the Cα atom of histamine was positioned 4.0 Å from the N5 hydride acceptor on the isoalloxazine ring (36-38). Additionally, the imidazole ring of histamine was positioned within the pocket of the aforementioned hydrophobic bowl (Figure 3-11A).

Compared to HaDHR, the docked structure of HaDHN (Figure 3-11B) revealed a different orientation for the imidazole ring of histamine substrate. In HaDHN, a single π-stacking interaction between Tyr181 and the substrate's imidazole ring was observed, which is consistent with the results of Reed *et al.* (19). A second, potential cation π-interaction between the protonated nitrogen attached to Cα and Trp267 may also be present. The distance between the Cα of the bound histamine (Figure 3-3) and the N5 of the isoalloxazine ring of the FMN cofactor (Figure 3-2) was observed to be 5.3 Å.

In the lowest free energy substrate-enzyme complexes of both proteins (Figures 3-11A and 3-11B), the substrate was found to be directly adjacent to the FMN. When protonated, the amine moiety formed favorable electrostatic interactions with the sidechain carboxyl oxygens of Glu74 and Asp354 in HaDHR, and Glu79 and Asp358 in HaDHN. In both docked structures, a conserved glutamic acid residue (Glu74 in HaDHR and Glu79 in HaDHN) were found to be positioned to act as a catalytic base and facilitate substrate deprotonation. This is consistent with mechanistic studies

on cholesterol oxidase where an acidic sidechain helped deprotonate the substrate during catalysis (39).

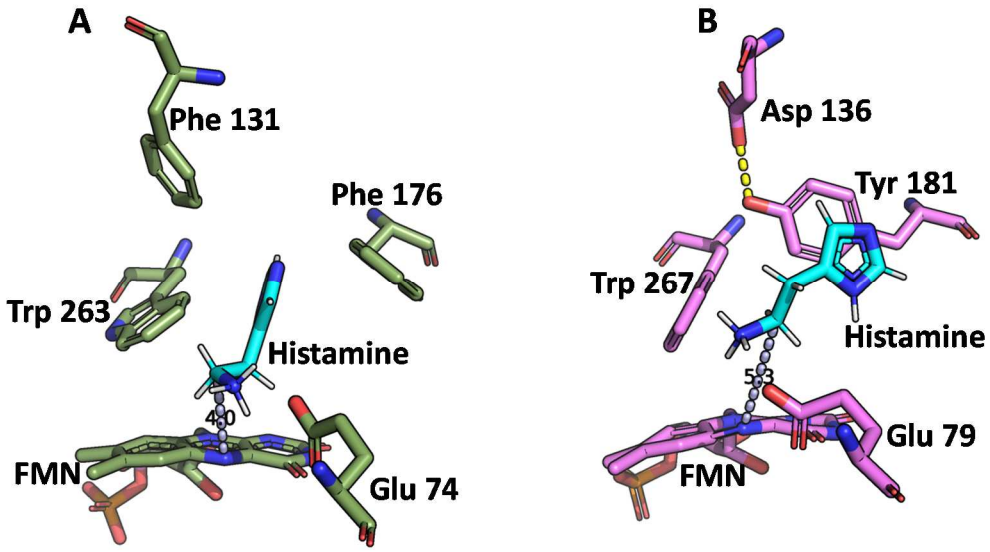

Figure 3-11 Models of histamine binding to the active sites of (A) HaDHR and (B) HaDHN. In HaDHR, histamine bound in the most favorable conformation is sandwiched between Trp263 and Phe176 with the Cα of histamine (as shown in Figure 3-4) positioned 4 Å from the N5 of the isoalloxazine ring of FMN. In HaDHN, the imidazole ring of histamine is stacked upon the aromatic ring of Tyr181 such that the Cα of histamine is >5 Å from the N5 of the isoalloxazine ring.

3.4.6 Molecular dynamic simulations of histamine in the HaDHR and HaDHN active site

The orientation of histamine in the HaDHR active site was further investigated with the aid of short molecular dynamic simulations of substrate bound *wt*-HaDHR and of a F176Y/F131D-HaDHR. Simulations were performed using the NAMD 2.12 package (31) and CHARMM36 force field (32) for the proteins, water, and ions, and with the CHARMM general force field (33) for the histamine substrates.

The initial orientation of histamine in the active site relative to the FMN cofactor was a docked structure as shown in Figure 3-11A (or Figure 3-12A). Even in a relatively short time (10 ns) unconstrained molecular dynamic simulations showed significant changes in the orientation of several key residues within the catalytic pocket of HaDHR (Figures 3-12B). Surprisingly, during this period, Phe176 in HaDHR reoriented away from the bound histamine substrate (Figure 3-12B). Concomitantly, the highly conserved His174 repositioned to form a hydrogen bond between the π-NH sidechain moiety and the τ-nitrogen of the histamine imidazole ring (Figure 3-3). Gln57 reoriented to form an additional hydrogen bond between its backbone carbonyl oxygen and the π-NH of the histamine imidazole ring as indicated in Figure 3-12B.

The histamine substrate in HaDHR repositioned so that the imidazole ring was stacked upon the isoalloxazine ring of the FMN. The Cα of histamine moved ~1 Å closer to the reactive N5 of the isoalloxazine ring to within ~3 Å (Figure 3-12C). This motion brings the hydride to be transferred close enough to the N5 to be effectively abstracted by FMN. The protonated α-N hydrogen also formed a hydrogen bond to the O4' carbonyl oxygen of FMN, as did a second hydrogen bond between the sidechain carboxyl oxygen of Glu74 and the α-N of histamine. This latter hydrogen bond is critical for properly orienting the substrate for hydride transfer. A space-filling model (Figure 3-12D) shows the tight packing interaction between histamine and the isoalloxazine ring

of the FMN. The model also shows the location of Cys30 that is covalently attached to the FMN, and which sterically limits the position of the substrate. In the absence of substrate, the orientation of the residues within the active site did not undergo significant reorientation during a similar 10 ns simulation.

The simulation for the F176Y/F131D double mutant of HaDHR in the presence of the bound substrate (Figure 3-14C), resulted in a shorter stable interaction between the Asp131 and Tyr176 compared to that seen for the corresponding HaDHN residues (*vide infra)*. The simulation of the HaDHR double mutant also showed that the hydrogen bond between the two mutated residues occasionally broke and reformed during the early stages of the simulations before finally breaking and leading to a reorientation of the two residues. The simulation results indicated that even though a hydrogen bond is formed, its lifetime is shorter in duration and subject to breaking and reforming. This process does not influence substrate inhibition in the HaDHR double mutant. Proper histamine orientation with respect to the isoalloxazine ring of the FMN is not restricted. These changes did affect the catalytic efficiency of the enzyme compared to *wt*-HaDHR, as was observed from our kinetic analysis. Each of the simulations was repeated three times and essentially the same trajectories were observed in each case.

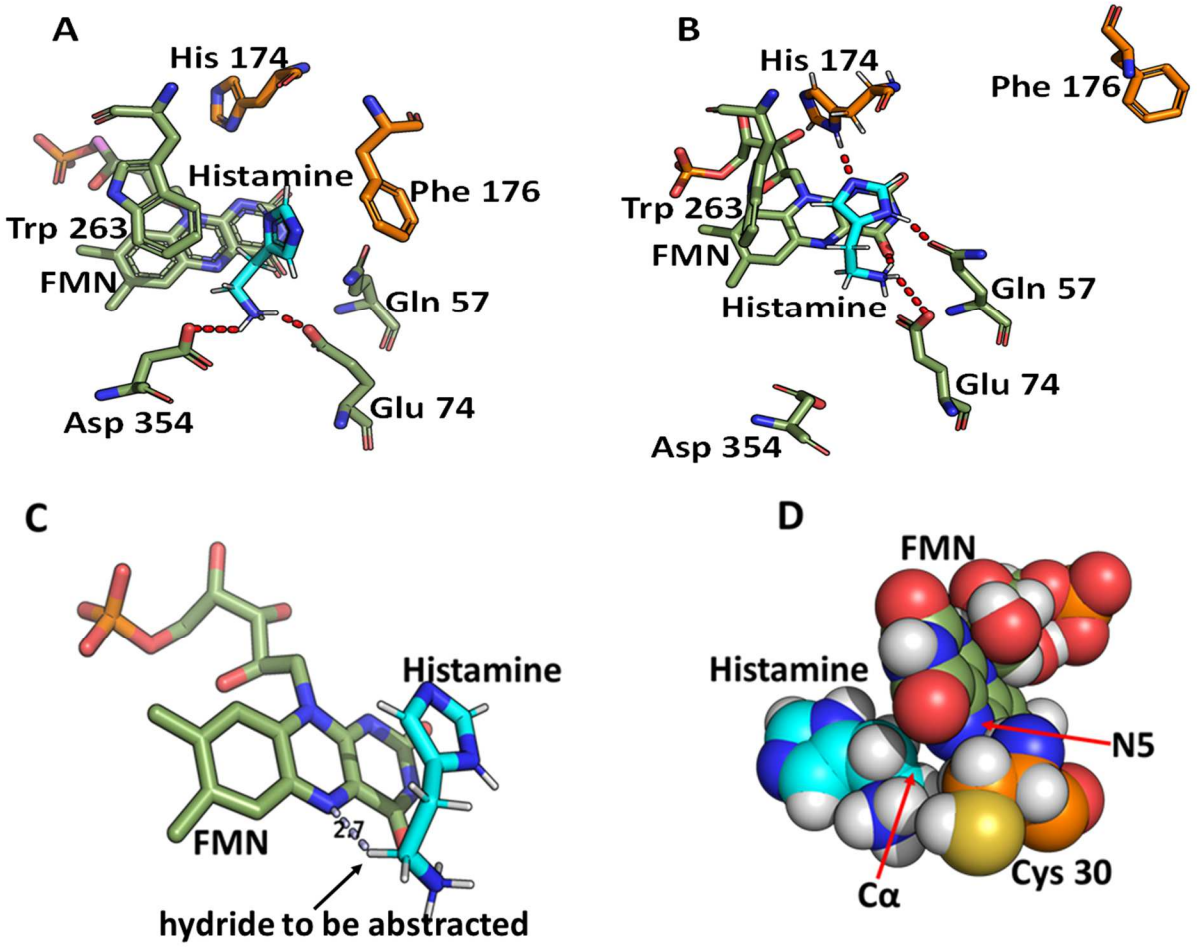

Figure 3-12 Molecular dynamic simulations of HaDHR in the presence of bound histamine. (A) The structural organization of HaDHR at the beginning of the simulation following docking of histamine and relaxation as described in the *Materials and Methods.* (B) The same structure after 10 ns of MD simulation. (C) The distance between Cα of histamine and N5 of the isoalloxazine ring after 10 ns MD simulation (D)Space-filling model of histamine bound in the active site following the MD simulation indicating the positions of Cys30 that is covalently linked to FMN, the N5 nitrogen of FMN, and the Cα of histamine.

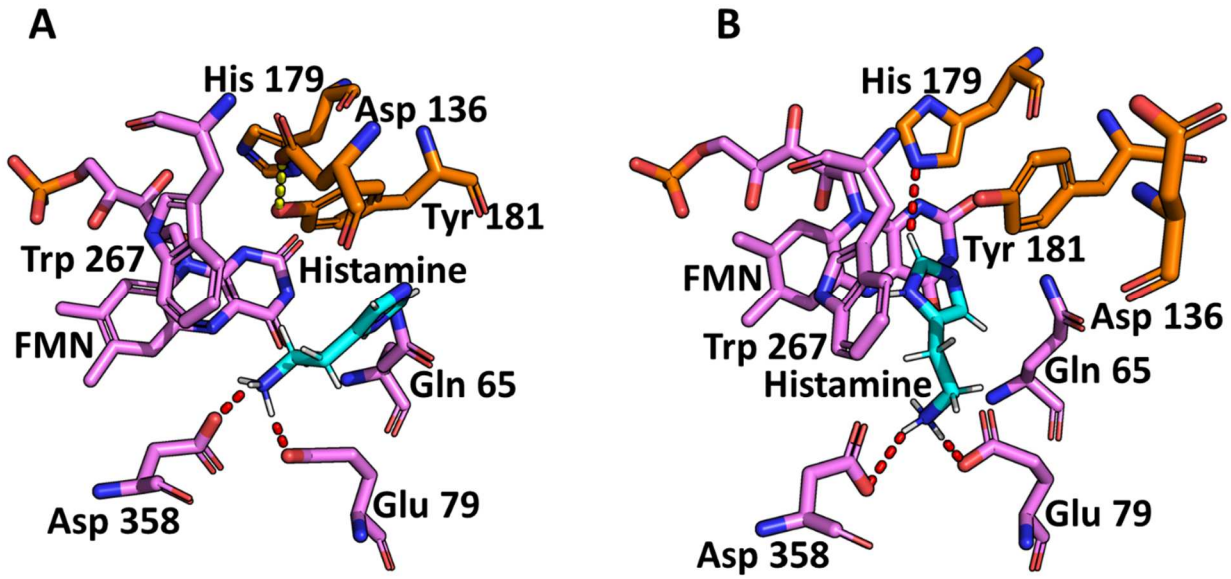

Figure 3-13 Molecular dynamic simulation of HaDHN in the presence of bound histamine. (A) The structural organization of the HaDHN active site at the beginning of the simulation with docked histamine and relaxation as described in the *Materials and Methods*. (B) The same structure after 10 ns of MD simulation.

As discussed earlier, the crystallographically observed hydrogen bond between Asp136-Tyr181 is an important structural feature of HaDHN that might contribute to substrate inhibition. This hydrogen bond remained intact during histamine docking into the HaDHN active site. Interestingly, the molecular dynamic simulations of HaDHN did not reproduce this observed structural feature. In particular, the disposition of the hydrogen bond between Asp136-Tyr181 changes over the simulation time course.

During the 10 ns simulation of HaDHN with histamine present in the active site, the hydrogen bond between Tyr181 and Asp136 was broken. This allowed the Tyr181 sidechain to reorient into a position similar to that observed for Phe176 in HaDHR. The reorientation of Tyr181 allows His179 to approach the bound histamine (Figure 3-13B) and form a hydrogen bond with the imidazole ring of histamine. The imidazole ring also repositions to allow for π-stacking interactions with Trp267. This π-stacking interaction with Trp263 is also observed in the HaDHR simulations. However, in HaDHN the imidazole ring of histamine could not undergo further π-stacking interactions with the isoalloxazine ring of the FMN, indicating that further "induced fit" of the substrate in the active site was required. Hydrogen bonds were also formed between the sidechain carboxyl oxygen of Glu74 and Asp358 and the α-N of histamine. No changes in these hydrogen bonds were observed after 10 ns, presumably due to the relatively short simulation.

The time dependent trajectories for reorientation of the HaDHN residues at Asp136 and Tyr181 as a function of the distance between the center of mass of the carboxyl oxygen atoms in the absence and presence of substrate is illustrated in Figures 3-14A and 3-14B. Without substrate, this hydrogen bond is rapidly broken within the first few picoseconds of the simulation resulting in a change in the distance between the Tyr181 hydroxyl and the carboxyl group of Asp136 of ~15 Å (Figure 3-14A). This is presumably due to the ready accessibility of water at this site. By contrast,

in the presence of the histamine substrate the simulation suggests that the bond is considerably more stable, taking several ns for it to break with the ensuing movement of Tyr181 toward a more favorable position for catalysis (Figure 3-14B).

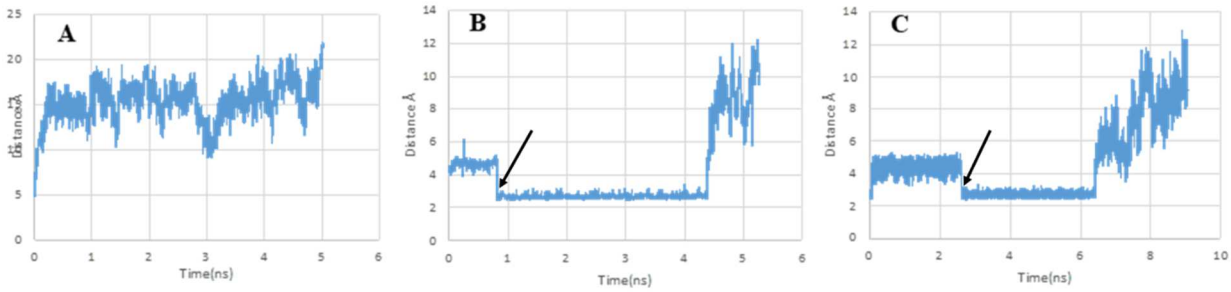

Figure 3-14 The effect of bound substrate on stabilizing the Tyr-Asp hydrogen bonding interaction.

Molecular dynamic simulations indicate changes in the distance between the center of mass of carboxyl oxygen atoms on Asp136 and the hydroxyl oxygen of Tyr181 in HaDHN as a function of time in ns in the absence (A) and presence (B) of histamine**. (**C) Trajectory for the equivalent residues at positions 131 and 176 in the HaDHR F131D/F176Y double mutant in the presence of histamine. The arrows indicate a sharp transition resulting from rotation of the oxygen atoms of the Asp residues around the C-Cα bond of the amino acid while maintaining the bonding interaction with the hydroxyl hydrogen of Tyr181/176. The data indicate a stabilizing effect of substrate on the hydrogen bonding interaction during the 10 ns simulation.

3.5 Discussion

HaDHR is the only member of a small family of flavin-dependent oxidoreductases that does not exhibit substrate inhibition. In Chapter 2 of this dissertation, we disclosed the high-resolution crystal structure of HaDHR that allowed us to undertake this current study to better characterize the origin of substrate inhibition in the family.

HaDHN, the closest homolog to HaDHR, shows a pH and concentration dependent substrate inhibition profile, which can be overcome by "HaDHR-like" mutations to the wildtype HaDHN enzyme (17). Substrate inhibition in TMADH, another family member, can also be eliminated by similar strategy (21). An important observation in the current study is that "HaDHN-like" mutations in HaDHR do not cause substrate inhibition and in some cases render the enzyme catalytically inactive. The immediate consequence of this observation is that while substrate inhibition can be eliminated (HaDHN to HaDHR-like mutations), the reverse process (HaDHR to HaDHN-like mutations) is more complicated and not all changes in structure and function between the two enzymes are reciprocal.

The origin of substrate inhibition in HaDHN has been proposed by Tsutsumi *et al.* (40) to be due to the formation and stabilization of the semiquinone form of the flavin when the second substrate binds to the enzyme. In addition to the hypothesis put forth by Tsutsumi, we believe that the cause of substrate inhibition in HaDHN must also consider these additional factors: the presence of a Tyr181-Asp136 hydrogen bond that restricts the movement of residues near the flavin, and π-stacking interactions between histamine and aromatic sidechains that stabilize the bound substrate conformation.

Although these enzymes have very similar backbone structures, there are several key differences within the catalytic pocket that likely contribute to substrate inhibition. The most conspicuous of

these is the orientation of the aromatic sidechain of Phe176 of HaDHR. In the crystal structure of HaDHN, the homologous residue, Tyr181, is positioned to enable a π-stacking interaction with the histamine imidazole ring which would be expected to stabilize the histamine in its bound conformation. Docking studies suggested that this is the lowest energy conformation, confirming similar studies by Reed *et al.* (19). The orientation of Tyr181 is also stabilized by hydrogen bonding to Asp136 which would promote this interaction. The importance of the hydrogen bond between Tyr181 and Asp136 in HaDHN was not previously identified. The crystal structure of HaDHR (disclosed and discussed in Chapter 2 of this dissertation) confirms that these interactions are absent in HaDHR as the equivalent residues are both phenylalanine (Phe176 and Phe131). The lack of a corresponding hydrogen bond in HaDHR to Phe176 in HaDHR helps contribute to the differences in side-chain orientation at the active site between the two enzymes. We postulate that this orientational difference and increased sidechain flexibility may likely be contributing to the lack of substrate inhibition in HaDHR.

We hypothesized that the F176Y single mutant, F176Y/F131D double mutant, and a F176Y/D265G/C266D triple mutant corresponding to "HaDHN-like" residues might induce substrate inhibition in HaDHR (Figure 3-1). Interestingly, we did not observe substrate inhibition in any of these mutants with histamine, although as might be expected, these mutations did influence catalytic activity. The enzyme kinetic data for the F176Y/F131D double mutant suggested that introduction of a hydrogen bond in the active site of HaDHR only resulted in decreased affinity for the substrate but did not restrict substrate orientation to the isoalloxazine ring of FMN. The kinetic data for the F176Y/D265G/C266D triple mutant also did not show any substrate inhibition, however the catalytic activity decreased significantly (Table 3-1, Figure 3-6). Since all other family members show substrate inhibition, we expected this mutant to behave in a

similar manner. Our result suggests that while it is possible to remove substrate inhibition in HaDHN by making the enzyme “HaDHR-like”, the reverse mutations in HaDHR do not cause a “HaDHN-like” substrate inhibition.

Tsutsumi *et al.* performed a detailed investigation of the flavin oxidation state and the corresponding UV-vis spectra of HaDHN and its mutants with histamine (17). Their work showed that the oxidized form of *wt*-HaDHN has a distinct peak at 450 nm whereas in the substrate-reduced form a distinct peak at 365 nm is observed. The peak at 365 nm was suggested to be the one electron reduced form of flavin, i.e., the semiquinone form (See Figure 3-2 (17)). Tsutsumi *et al.* in their UV-vis spectral studies on *wt*-HaDHN showed that with the increase in histamine concentration the peak at 365 nm increased thereby suggesting the stabilization of the semiquinone form (17). In their UV-vis spectra for the substrate-reduced form of single and triple mutations that showed 50-80% reduction or did not show any substrate inhibition, they observed a flat region at 365 nm. By contrast, a distinct peak at 365 nm similar to *wt*-HaDHN was observed in their double mutant that showed substrate inhibition, suggesting that the change in geometry or the oxidation state of the flavin is playing a role in contributing to substrate inhibition. In subsequent studies performed using stopped-flow kinetic analyses and EPR studies on *wt*-HaDHN, they concluded that this histamine concentration dependent stabilization of the semiquinone form of flavin is responsible for substrate inhibition in HaDHN (40,41)

To further understand the possible role of semiquinone stabilization in HaDHR, UV-vis spectroscopic analysis of *wt*-HaDHR, *wt*-HaDHN and some HaDHR mutants were performed (Figures 3-7 and 3-8). Interestingly, *wt*-HaDHR is flat in the rgion of 365 nm in its substrate-reduced form.The spectral signature at 365 nm for *wt*-HaDHR is similar to that observed by Tsutsumi *et al*. in their single and triple mutants of HaDHN that did not show substrate inhibition,

i.e., a flat region at 365 nm (17). The lack of absorbance at 365 nm signifies only a transient presence of the semiquinone form of the flavin, as the semiquinone must occur on the pathway to the fully reduced flavin. Our *wt*-HaDHN UV-vis spectra showed a distinct peak at 365 nm similar to that observed by Tsutsumi *et al.* (17). Interestingly, the UV-vis spectra for our single HaDHR mutant were similar to that observed for *wt*-HaDHR whereas our double HaDHR mutant showed a further flattening at 365 nm. The triple HaDHR mutant prepared to mimic HaDHN-like substrate inhibition also showed a spectral signature at 365 similar to that observed for double HaDHR mutant. A lower intensity or the complete absence of a peak at 365 nm is indicative of the fully reduced from of the flavin being thermodynamically favorable. This might suggest that the flavin in HaDHR is more stable in the reduced form unlike in HaDHN where the semiquinone form is stabilized as histamine concentration increases.

We further analyzed the surface model of both the enzymes and observed that Thr130 in HaDHR is present at the substrate entry site, whereas Pro135 in HaDHN is at the same position (Figure 3-9). We speculated that Pro135 in HaDHN might be functioning as a switch regulating the entry of the substrate at the active site. If so, we believed that the T130P mutation in the background of the F176Y/F131D double mutant would induce substrate inhibition. The T130P/F176Y/F131D triple mutant when analyzed was observed to be catalytically inactive. The UV-vis spectrum for this triple mutant did not show any difference between the oxidized and the substrate-reduced forms, further suggesting that the mutant is inactive (Figure 3-10). This lack of activity could be due to the occlusion of the substrate entry channel thereby restricting the entry of the substrate to the active site in HaDHR, or complete misalignment of the catalytic site due to the presence of the proline. This also suggested that Pro135 in HaDHN might be acting as a switch regulating substrate

entry, thereby causing substrate inhibition in HaDHN at high substrate concentration. Regardless, this switch is not transferrable to HaDHR.

Overall, the UV-vis studies suggested that the electronic state of flavin in the substrate-reduced form in HaDHR is somewhere between the semiquinone (FMN_{sq}) and the fully reduced (FMN_R) state. Tsutsumi studies benefitted from EPR experiments, confirming the presence of the semiquinone state of the FMN. The degree of semiquinone formation in the absence of EPR studies is difficult to quantitate in HaDHR. Nonetheless, the flavin states in the substrate-reduced form of the double and triple mutants of HaDHR were more like FMN_R, thereby suggesting that the electronic state of the flavin in HaDHR is quite different from HaDHN. Said alternatively, the addition of histamine is sufficient to reduce the oxidized FMN to the fully reduced form if there is sufficient bending of the flavin ring or other structural modification which result in more favorable reduction to the fully reduced form. Otherwise, the partial reduction to the semiquinone would occur, suggesting that the process is driven by thermodynamics.

Thermodynamic stability in a mixed-valence dinuclear complexes are denoted as a combination of reduced (Red) and oxidized (Ox) sites, which is exhibited as a difference in redox potentials $\Delta E°=E°(Ox\text{-}Ox)/Red\text{-}Ox)-E°(Red\text{-}Ox/Red\text{-}Red)$. This difference is related to the comproportionation constant, K_c, defined as $K_c= \exp(\Delta E°F/RT)$. The bending of the flavin molecule along with other structural modifications around the flavin favors more facile reduction to FMN_R. For a flavin to be fully reduced, it has to undergo a one electron-reduction from a FMN_O to FMN_{sq}, and then the second reduction of FMN_{sq} to FMN_R. When the formal potentials for the first reduction, FMN_o to $FMN_{sq,}$ and the reduction from FMN_{sq} to FMN_R gets closer to each other, the comproportionation constant becomes very small. This suggests that at equilibrium only small amounts of FMN_{sq} exist, thereby thermodynamically favoring the reduction all the way to FMN_R.

Based on our UV-vis studies where the distict peak at 365 nm corresponding to FMN_{sq} is absent (Figure 3-7A) and a ~1° greater bend in isoalloxazine ring of flavin in HaDHR compared to HaDHN, we speculate that the comproportionation constant for HaDHR is very small. These studies suggest that the initial reduction of the flavin in HaDHR is favored towards FMN_R and only transient amounts of FMN_{sq} exists at equilibrium.

Interestingly, substrate inhibition in this family of enzymes is only observed with its own specific substrate (17,42), whereas with other substrates no substrate inhibition has been observed so far (43). To gain further insights into this issue and to understand the mode of substrate binding and its influence on substrate inhibition, histamine docking studies (Figure 3-11) were performed. Short molecular dynamic simulations on both enzymes were also performed (Figures 3-12 and 3-13). These studies suggested that the mode of histamine binding in both HaDHR and HaDHN is very different. In HaDHR, due to the absence of hydrogen bonding, histamine was found to be better placed for catalysis and was sandwiched between two aromatic residues Trp263 and Phe176. In HaDHN a stacked histamine-tyrosine complex was observed which was found to be further stabilized due to the presence of Asp136-Tyr181 hydrogen bonding. This was confirmed from the short molecular dynamic simulations of HaDHN in the presence of histamine. In the absence of histamine, the simulations under fully hydrated conditions indicated that the Asp136-Tyr181 bond in HaDHN is labile to attack by water. When this bond breaks, Tyr181 moves into a position similar to that of Phe176 in HaDHR. A similar result was observed for the F176Y/F131D double mutant of HaDHR, although the bond kept breaking initially and was only stable for few nanoseconds.

There are several observations that support the hypothesis that the stacked histamine-tyrosine complex predicted for HaDHN (19) represents a form of bound substrate that is not catalytically viable. Most obvious is that the orientation of histamine in this conformation is incompatible with

a catalytic mechanism that requires a closer approach of the Cα of histamine to the site of catalysis (N5 or C4 carbonyl oxygen) on the isoalloxazine ring of the FMN (36-38). The hypothesis is also supported by the observed reduction in substrate inhibition resulting from Y181F substitution in HaDHN (17). Thirdly, the MD simulations indicated that, due to ready access of water to the active site, this conformation is short-lived whereupon several amino acid sidechains reorient toward a more compatible conformation for catalysis. Further, simulation of the HaDHR enzyme predicted that the substrate undergoes an "induced fit" that brings the Cα of the histamine substrate into direct contact with the N5 of the isoalloxazine ring. The simulation also indicated that the bulky Cys30 that is covalently attached to the isoalloxazine ring does not interfere with the interaction between the Cα atom of histamine and the N5 of FMN (Figure 3-12 D), suggesting that this is the likely site of catalysis rather than the nearby carbonyl oxygen on C4 which has been suggested as an alternate site (19). Thus, in both HaDHR and HaDHN, an "induced fit" would be required to bring the histamine into similar catalytically favorable positions, *e.g.* ~3 Å from N5. The typical distance observed in flavoprotein crystals range between 2.8 and 3.4 Å (36).

Classical substrate inhibition is assumed to result from a non-competitive binding of substrate to a second, usually non-catalytic site in an enzyme. (44,45). The possibility of more than one substrate molecule binding within an active site is supported, for example, by studies of acetylcholinesterase (46,47). In TMADH, the best studied member of this family of dehydrogenases, an alternative model for substrate inhibition was hypothesized (16,42). The presence of two alternate catalytic cycles was proposed which were dependent upon the distribution of electrons between the FMN and Fe_4S_4 cofactors. Based on the number of reducing equivalents present in the oxidized/reduced enzyme encountered in each cycle, the terms 0/2 or 1/3 cycles were introduced. These terms represent catalytic cycles that predominantly feature

either the oxidized and two-electron reduced forms of the enzyme (0/2 cycle), or the one-and three-electron reduced forms of the enzyme (1/3 cycle).

The cycle in which the enzyme operates depends on the fate of the two-equivalent reduced enzyme formed after the initial reaction of oxidized enzyme with one equivalent of substrate. The two-equivalnet reduced enzyme species can react either with the electron acceptor to give oxidized enzyme, or with the substrate to give rise to a spin-interacting state. This unusual circumstance arises when the substrate can donate two electrons, but the external electron acceptor can only accept one electron at a time and the full reduction of the enzyme requires three electrons. The third electron required for full enzyme reduction is derived from a second molecule of substrate. Therefore, the complete oxidation of three molecules of substrate requires two full redox-cylces of the enzyme.

Ultimately which cycle predominates under steady-state conditions depends primarily on the relative concentrations of the substrate and the external electron acceptor. Said alternatively, when the 0/2 cycle predominates, the substrate reduces FMNo all the way to FMN_R with a very short-lived or transient FMN_{sq} state, whereas when the 1/3 cycle predominates, the substrate reduces FMNo to FMN_{sq} in the first step and then FMN_{sq} to FMN_R in the second step. It has been demonstrated previously that product release and the binding of the second substrate molecule to the two-electron reduced enzyme is the rate-limiting step (43). At high substrate concentrations, the binding of the substrate to the one-electron reduced enzyme form (FMN_{sq}) at steady-state conditions stabilizes the semiquinone form, thereby slowing the enzymatic turnover in the 1/3 cycle compared to the 0/2 cycle. This binding of the substrate to the stabilized semiquinone form demonstrates a kinetic effect that is equivalent to substrate inhibition effect (42).

At low substrate and/or high acceptor concentration, the 0/2 cycle dominates the internal electron transfer pathway of TMADH, whereas, the 1/3 cycle dominates at high substrate concentrations where substrate inhibition is observed (16,42). In both cases, the two electrons from the initial reduction of the FMN are rapidly distributed between the two cofactors resulting in the $FMN_{sq}FeS_R$ state. In Chapter 2 of this dissertation, we performed preliminary investigations on the electron transfer pathway from the FMN to Fe_4S_4 cluster. These current studies are by no means comprehensive because our focus was understanding the initial electron transfer between the substrate and the flavin which are part of the initial steps of the catalytic process. These studies also suggest the internal electron transfer processes are highly tuned and will require further investigation.

Stopped-flow kinetic analysis with HaDHN (40), in which the reductive half reaction was examined based on spectral changes related to redox states of the flavin, identified three rate constants representing three sequential first order reactions (40) similar to those identified for TMADH (42). An initial fast phase was assigned to the two-electron reduction of FMN, a second moderate phase was assigned to the intramolecular transfer of an electron from FMN to the Fe_4S_4 center producing the semiquinone form of the flavin and reduced iron sulfur center, $FMN_{sq}FeS_R$. A third, slow phase, occurred in the presence of excess substrate and was attributed to the inhibitory binding of substrate (40). Interestingly, adding a large excess of histamine to HaDHN in the absence of an electron acceptor resulted in stabilization of the $FMN_{sq}FeS_R$ state as determined spectrophotometrically (17). Significantly, mutation of Y181F in HaDHN blocked formation of the $FMN_{sq}FeS_R$ state, instead favoring the FMN_RFeS_O state under either low or high substrate concentrations (17). The investigations on HaDHN did not consider the 0/2 or 1/3 cycles, although it is expected that the 1/3 cycle would also predominate at high substrate concentration.

The Michaelis-Menten kinetics and UV-vis spectra of HaDHR and the mutants examined in this dissertation are consistent with the model that only the FMN_RFeS_O state is present in HaDHR or perhaps FMNsq has a very transient existence which is therefore not observed spectrally at both low and high substrate concentration, suggesting only the 0/2 cycle is relevant. This is also consistent with the result that in TAMDH, when a non-inhibiting substrate is used, only the 0/2 cycle is observed (16). These observations would also suggest that the hydrogen bond between Asp136-Tyr181 in HaDHN may be a requirement for stabilizing the $FMN_{sq}FeS_R$ state at high substrate concentration. This speculation is consistent with Tsutsumi et al.'s observation with the single Y181F mutant in HaDHN, that 50-80% of substrate inhibition was overcome (17). However, the F176Y/F131D double mutant of HaDHR, designed to mimic the hydrogen-bonded pair at the same position in HaDHN, and the F176Y/D265G/C266D triple mutant designed to mimic "HaDHN-like" mutations, did not induce formation of the $FMN_{sq}FeS_R$ state at high substrate concentration, indicating that FMN_RFeS_O is the favored equilibrium state in HaDHR in the two-electron reduced enzyme, even though the electrons are transferred one at a time.

Our surface model analysis and the T130P/F176Y/F131D triple mutant in HaDHR suggested that Pro135 in HaDHN might be acting as a switch in controlling the concentration of substrate entering the active site. Overcoming of substrate inhibition in Y181F mutation in HaDHN observed by Tsutsumi *et al.* (17) might also be due to the regulation of the binding of the substrate at the active site by Pro135. These studies suggested that even though the two structures are quite similar, just a few key residues in the active site controls the environment around the FMN and the wider substrate entry channel in HaDHR. These modest changes abolish substrate inhibition, which is further confirmed by making "HaDHR-like" mutations to remove substrate inhibition in HaDHN. The reciprocal process of inducing substrate inhibition in HaDHR is difficult.

The structural comparison of HaDHR and HaDHN coupled with docking and simulation studies supports the idea that the substrate can bind to the enzyme forming a substrate-enzyme complex that is maximally catalytically productive (S^p), but that the substrate can also bind to the enzyme forming an unproductive complex (S^u). The existence of these two states can be readily reconciled with the two-cycle model of TMADH and the $FMN_{sq}FeS_R/FMN_RFeS_O$ model of HaDHN substrate inhibition. In reality, these two models are effectively the same, as both relate the degree of substrate inhibition to the flow of electrons from the active site to the surface of the enzyme.

If the productive site has a higher affinity for substrate than the unproductive site and principally operates at low substrate concentration via the 0/2 cycle (TMADH) or FMN_RFeS_O (HaDHN) then at higher substrate concentration the unproductive site becomes occupied to a greater extent, directing the enzyme through the 1/3 cycle (TMADH) or $FMN_{sq}FeS_R$ (HaDHN). Substrate binding in the unproductive conformation stabilizes the flavin in the semiquinone form so that the intramolecular electron transfer between the FMN_{sq} and FeS_O, becomes rate-limiting, reducing the k_{cat}. Tsutsumi *et al.* (17,40) also proposed the existence of two binding sites for histamine or that the second histamine binds to a substrate-reduced enzyme in which the FMN_{sq} is the stabilized state and that the intramolecular electron transfer from the FMN_{sq} to FeS_O at high substrate concentration is unfavorable and rate-limiting. Assuming this is the case, the conversion of FMN_{sq} to FMN_R must be accompanied by a conformational change within the active site that destabilizes the unproductive state (S^u) enabling the substrate to assume the productive state (S^p) leading to product formation.

Our observations from the short molecular simulations strongly suggest that this conformational change results from breaking the Asp136-Tyr181 hydrogen bond accompanied by repositioning of histamine in the active site to adopt a similar position to that found in the “induced fit” structure

of HaDHR. We speculate that with *wt*-HaDHR and its double and triple mutants, the intramolecular electron transfer from FMN_R to FeS_O is instead the rate limiting step at both low and high substrate concentrations due to differences in the formal potentials of the cofactors of the two enzymes. How *wt*-HaDHR and its double and triple mutants are involved in modifying the formal potentials of the FMN and FeS cofactors is the subject of ongoing mutational and structural analysis.

In conclusion, side-by side comparison of the active site residues in two closely related flavin-dependent histamine dehydrogenases has provided, a high-resolution structural basis for understanding the absence of substrate inhibition in HaDHR and presence of substrate inhibition in HaDHN simultaneously. Molecular dynamic simulations have indicated that histamine and HaDHR undergo an "induced fit" as histamine binds within the active site of HaDHR, thereby providing novel mechanistic insight into how both the enzyme and substrate conform for optimal catalytic turnover. This is not evident by simply examining the crystal structure. Our observations also support the two-cycle model of substrate inhibition put forward by Roberts *et al.* (16) by providing structural evidence for how substrate can induce the switch between the two cycles in a concentration-dependent manner. Lastly, the unusually high specificity of HaDHR for histamine, the fact that it is not inhibited by tryptophan, its robust turnover and K_{50} that matches physiological concentrations of histamine in biological fluids (48,49) and spoiled foods (50,51) demonstrate essential properties of the biological recognition element for a biosensor. An important remaining issue is creating highly efficient direct electron transfer (DET) between the enzyme and the electrod that we and others (11,50,51) are actively pursuing.

3.6 References

1. Bakke, M., Sato, T., Ichikawa, K., and Nishimura, I. (2005) Histamine dehydrogenase from Rhizobium sp.: gene cloning, expression in Escherichia coli, characterization and application to histamine determination. *Journal of biotechnology* **119**, 260-271
2. Fujieda, N., Satoh, A., Tsuse, N., Kano, K., and Ikeda, T. (2004) 6-S-Cysteinyl flavin mononucleotide-containing histamine dehydrogenase from Nocardioides simplex: molecular cloning, sequencing, overexpression, and characterization of redox centers of enzyme. *Biochemistry* **43**, 10800-10808
3. Siddiqui, J. A., Shoeb, S. M., Takayama, S., Shimizu, E., and Yorifuji, T. (2000) Purification and characterization of histamine dehydrogenase from Nocardioides simplex IFO 12069. *FEMS microbiology letters* **189**, 183-187
4. Steenkamp, D. J., and Beinert, H. (1982) Mechanistic studies on the dehydrogenases of methylotrophic bacteria. 2. Kinetic studies on the intramolecular electron transfer in trimethylamine and dimethylamine dehydrogenase. *Biochemical Journal* **207**, 241-252
5. Steenkamp, D. J., and Mallinson, J. (1976) Trimethylamine dehydrogenase from a methylotrophic bacterium. I. Isolation and steady-state kinetics. *Biochimica et biophysica acta* **429**, 705-719
6. Yang, C. C., Packman, L. C., and Scrutton, N. S. (1995) The primary structure of Hyphomicrobium X dimethylamine dehydrogenase: relationship to trimethylamine dehydrogenase and implications for substrate recognition. *European journal of biochemistry* **232**, 264-271
7. Winkler, J. R., and Gray, H. B. (2014) Long-range electron tunneling. *Journal of the American Chemical Society* **136**, 2930-2939
8. Prabhulkar, S., Tian, H., Wang, X., Zhu, J.-J., and Li, C.-Z. (2012) Engineered proteins: redox properties and their applications. *Antioxidants & redox signaling* **17**, 1796-1822
9. Yoch, D. C., and Carithers, R. (1979) Bacterial iron-sulfur proteins. *Microbiological reviews* **43**, 384-421
10. Bím, D., Alonso-Gil, S., and Srnec, M. (2020) From Synthetic to Biological Fe4S4 Complexes: Redox Properties Correlated to Function of Radical S-Adenosylmethionine Enzymes. *ChemPlusChem* **85**, 2534-2541
11. Henao-Escobar, W., Del Torno-de Roman, L., Domínguez-Renedo, O., Alonso-Lomillo, M., and Arcos-Martínez, M. (2016) Dual enzymatic biosensor for simultaneous amperometric determination of histamine and putrescine. *Food chemistry* **190**, 818-823
12. Tsutsumi, M., Tsujimura, S., Shirai, O., and Kano, K. (2009) Direct electrochemistry of histamine dehydrogenase from Nocardioides simplex. *Journal of Electroanalytical Chemistry* **625**, 144-148
13. Loechel, C., Basran, A., Basran, J., Scrutton, N. S., and Hall, E. A. (2003) Using trimethylamine dehydrogenase in an enzyme linked amperometric electrode Part 1. Wild-type enzyme redox mediation. *Analyst* **128**, 166-172
14. Loechel, C., Basran, A., Basran, J., Scrutton, N. S., and Hall, E. A. (2003) Using trimethylamine dehydrogenase in an enzyme linked amperometric electrode Part 2. Rational design engineering of a ‘wired’mutant. *Analyst* **128**, 889-898

15. Sato, T., Horiuchi, T., and Nishimura, I. (2005) Simple and rapid determination of histamine in food using a new histamine dehydrogenase from Rhizobium sp. *Analytical biochemistry* **346**, 320-326
16. Roberts, P., Basran, J., Wilson, E. K., Hille, R., and Scrutton, N. S. (1999) Redox cycles in trimethylamine dehydrogenase and mechanism of substrate inhibition. *Biochemistry* **38**, 14927-14940
17. Tsutsumi, M., Tsuse, N., Fujieda, N., and Kano, K. (2010) Site-directed mutation at residues near the catalytic site of histamine dehydrogenase from Nocardioides simplex and its effects on substrate inhibition. *Journal of biochemistry* **147**, 257-264
18. Trickey, P., Basran, J., Lian, L.-Y., Chen, Z.-w., Barton, J. D., Sutcliffe, M. J., Scrutton, N. S., and Mathews, F. S. (2000) Structural and biochemical characterization of recombinant wild type and a C30A mutant of trimethylamine dehydrogenase from Methylophilus methylotrophus (sp. W3A1). *Biochemistry* **39**, 7678-7688
19. Reed, T., Lushington, G. H., Xia, Y., Hirakawa, H., Travis, D. M., Mure, M., Scott, E. E., and Limburg, J. (2010) Crystal structure of histamine dehydrogenase from Nocardioides simplex. *Journal of Biological Chemistry* **285**, 25782-25791
20. Lim, L., Shamala, N., Mathews, F., Steenkamp, D., Hamlin, R., and Xuong, N. H. (1986) Three-dimensional structure of the iron-sulfur flavoprotein trimethylamine dehydrogenase at 2.4-A resolution. *Journal of Biological Chemistry* **261**, 15140-15146
21. Basran, J., Jang, M.-H., Sutcliffe, M. J., Hille, R., and Scrutton, N. S. (1999) The role of Tyr-169 of trimethylamine dehydrogenase in substrate oxidation and magnetic interaction between FMN cofactor and the 4Fe/4S center. *Journal of Biological Chemistry* **274**, 13155-13161
22. Haynes, C. A., Koder, R. L., Miller, A.-F., and Rodgers, D. W. (2002) Structures of nitroreductase in three states: effects of inhibitor binding and reduction. *Journal of Biological Chemistry* **277**, 11513-11520
23. Lyubimov, A. Y., Heard, K., Tang, H., Sampson, N. S., and Vrielink, A. (2007) Distortion of flavin geometry is linked to ligand binding in cholesterol oxidase. *Protein Science* **16**, 2647-2656
24. McNaught, A. D., and Wilkinson, A. (1997) Compendium of chemical terminology. IUPAC recommendations. in *Compendium of chemical terminology. IUPAC recommendations*, Blackwell Scientific Publications, Oxford pp
25. Zhang, Y., and Skolnick, J. (2005) TM-align: a protein structure alignment algorithm based on the TM-score. *Nucleic acids research* **33**, 2302-2309
26. Stols, L., Gu, M., Dieckman, L., Raffen, R., Collart, F. R., and Donnelly, M. I. (2002) A new vector for high-throughput, ligation-independent cloning encoding a tobacco etch virus protease cleavage site. *Protein expression and purification* **25**, 8-15
27. Qin, H., Hu, J., Hua, Y., Challa, S. V., Cross, T. A., and Gao, F. P. (2008) Construction of a series of vectors for high throughput cloning and expression screening of membrane proteins from Mycobacterium tuberculosis. *BMC biotechnology* **8**, 51
28. Swearingen, C., Wu, J., Stucki, J., and Fitch, A. (2004) Use of ferrocenyl surfactants of varying chain lengths to study electron transfer reactions in native montmorillonite clay. *Environmental science & technology* **38**, 5598-5603

29. Bradford, M. M. (1976) A rapid and sensitive method for the quantitation of microgram quantities of protein utilizing the principle of protein-dye binding. *Analytical biochemistry* **72**, 248-254
30. ULC, C. C. G. Molecular Operating Environment (MOE). 2005.06 Ed.
31. Phillips, J. C., Braun, R., Wang, W., Gumbart, J., Tajkhorshid, E., Villa, E., Chipot, C., Skeel, R. D., Kale, L., and Schulten, K. (2005) Scalable molecular dynamics with NAMD. *Journal of computational chemistry* **26**, 1781-1802
32. Best, R. B., Zhu, X., Shim, J., Lopes, P. E., Mittal, J., Feig, M., and MacKerell Jr, A. D. (2012) Optimization of the additive CHARMM all-atom protein force field targeting improved sampling of the backbone φ, ψ and side-chain χ1 and χ2 dihedral angles. *Journal of chemical theory and computation* **8**, 3257-3273
33. Vanommeslaeghe, K., Hatcher, E., Acharya, C., Kundu, S., Zhong, S., Shim, J., Darian, E., Guvench, O., Lopes, P., and Vorobyov, I. (2010) CHARMM general force field: A force field for drug-like molecules compatible with the CHARMM all-atom additive biological force fields. *Journal of computational chemistry* **31**, 671-690
34. Freddolino, P. L., Gardner, K. H., and Schulten, K. (2013) Signaling mechanisms of LOV domains: new insights from molecular dynamics studies. *Photochemical & Photobiological Sciences* **12**, 1158-1170
35. Bellamy, H., Lim, L., Mathews, F., and Dunham, W. R. (1989) Studies of crystalline trimethylamine dehydrogenase in three oxidation states and in the presence of substrate and inhibitor. *Journal of Biological Chemistry* **264**, 11887-11892
36. Fraaije, M. W., and Mattevi, A. (2000) Flavoenzymes: diverse catalysts with recurrent features. *Trends in biochemical sciences* **25**, 126-132
37. Massey, V. (1995) Introduction: flavoprotein structure and mechanism. *The FASEB Journal* **9**, 473-475
38. Piano, V., Palfey, B. A., and Mattevi, A. (2017) Flavins as covalent catalysts: new mechanisms emerge. *Trends in biochemical sciences* **42**, 457-469
39. Yu, L.-J., Golden, E., Chen, N., Zhao, Y., Vrielink, A., and Karton, A. (2017) Computational insights for the hydride transfer and distinctive roles of key residues in cholesterol oxidase. *Scientific reports* **7**, 1-13
40. Tsutsumi, M., Tsujimura, S., Shirai, O., and Kano, K. (2010) Stopped flow kinetic studies on reductive half-reaction of histamine dehydrogenase from Nocardioides simplex with histamine. *The Journal of Biochemistry* **148**, 47-54
41. Tsutsumi, M., Fujieda, N., Tsujimura, S., Shirai, O., and Kano, K. (2008) Thermodynamic redox properties governing the half-reduction characteristics of histamine dehydrogenase from Nocardioides simplex. *Bioscience, biotechnology, and biochemistry* **72**, 786-796
42. Jang, M.-H., Basran, J., Scrutton, N. S., and Hille, R. (1999) The reaction of trimethylamine dehydrogenase with trimethylamine. *Journal of Biological Chemistry* **274**, 13147-13154
43. Rohlfs, R. J., and Hille, R. (1994) The reaction of trimethylamine dehydrogenase with diethylmethylamine. *Journal of Biological Chemistry* **269**, 30869-30879
44. Kaiser, P. M. (1980) Substrate inhibition as a problem of non-linear steady state kinetics with monomeric enzymes. *Journal of Molecular Catalysis* **8**, 431-442
45. Kühl, P. (1994) Excess-substrate inhibition in enzymology and high-dose inhibition in pharmacology: a reinterpretation. *Biochemical Journal* **298**, 171-180

46. Colletier, J. P., Fournier, D., Greenblatt, H. M., Stojan, J., Sussman, J. L., Zaccai, G., Silman, I., and Weik, M. (2006) Structural insights into substrate traffic and inhibition in acetylcholinesterase. *The EMBO journal* **25**, 2746-2756
47. Xu, Y., Colletier, J.-P., Weik, M., Qin, G., Jiang, H., Silman, I., and Sussman, J. L. (2010) Long route or shortcut? A molecular dynamics study of traffic of thiocholine within the active-site gorge of acetylcholinesterase. *Biophysical journal* **99**, 4003-4011
48. Alvarez, X. A., Franco, A., Fernández-Novoa, L., and Cacabelos, R. (1996) Blood levels of histamine, IL-1β, and TNF-α in patients with mild to moderate alzheimer disease. *Molecular and chemical neuropathology* **29**, 237-252
49. Cacabelos, R. (1990) Histaminergic system: Neuroendocrine function of brain histamine. *Methods Find Exp Clin Pharmacol* **12**, 341-376
50. Keow, C. M., Bakar, F. A., Salleh, A. B., Heng, L. Y., Wagiran, R., and Bean, L. S. (2007) An amperometric biosensor for the rapid assessment of histamine level in tiger prawn (Penaeus monodon) spoilage. *Food chemistry* **105**, 1636-1641
51. Young, J. A., Jiang, X., and Kirchhoff, J. R. (2013) Amperometric detection of histamine with a pyrroloquinoline-quinone modified electrode. *Electroanalysis* **25**, 1589-1593

Chapter 4. Engineering the HaDHR enzyme with gold and platinum metal affinity peptides for controlled orientation to develop a working amperometric biosensor

4.1 Abstract

Development of a working amperometric biosensor requires that the biorecognition element, i.e. the enzyme, be immobilized on the transduction element in a stable configuration and orientation. Genetically engineered metal affinity peptides have been described to orient an enzyme to a transduction element. Compared to traditional chemical methods, a single step bio-assembly process should show comparable binding affinity with improved orientational control. In this study, we engineered HaDHR with noble metal affinity peptides directed to gold or platinum to orient and immobilize the enzyme on the electrode surface. A six amino acid linker was used for gold binding peptide and a four amino acid linker was used for the platinum binding peptides. The engineered enzyme was characterized using multiple techniques, including surface plasmon resonance (SPR), atomic force microscopy (AFM), dynamic light scattering (DLS), and quartz crystal microbalance (QCM). Initial binding studies for the gold binding peptides were performed using SPR. The studies suggested that the ionic strength, e.g., the concentration of salts may play an important role in binding of the cAuBP peptides to the gold surface. The AFM studies showed more aggregates for the HaDHR-cAuBP-CT constructs, further emphasizing the importance of electrostatic interactions of the metal binding peptides with the surface when tethered to an enzyme. Preliminary studies with platinum binding peptides were performed using DLS and QCM. Both studies showed interaction of the platinum binding peptides to a platinum surface. In addition, QCM studies with the HaDHR-cAuBP-CT were also performed. The buffer conditions used in the QCM measurements were guided by our SPR studies. The HaDHR-cAuBP-CT construct showed significant binding to a gold surface as compared to the unmodified HaDHR,

consistent with the SPR binding isotherms. The HaDHR-PtBP-CT construct also showed binding to a platinum surface, however, over time delamination was observed. The importance of linker sequence in controlling the orientation, presentation, and direction of the enzyme tethered metal binding peptides to a surface was also highlighted in these studies.

4.2 Introduction

Enzyme based amperometric biosensors, that are often used in medical care, are divided into three broad classes or generations that reflect how electrons are delivered to the transduction element of the biosensor. The Generation 1/Gen 1 biosensor uses an oxidase enzyme, with ambient oxygen acting as the electron acceptor from the enzyme to generate hydrogen peroxide. The hydrogen peroxide is typically measured electrochemically at a noble metal surface where electrons are transferred from the peroxide to the transduction element generating a current and regenerating oxygen (1). Other measurement modalities not involving noble metal transduction elements have also been described (2-5). This process is stoichiometric with respect to substrate, where one molecule of substrate will generate one molecule of peroxide which will generate a current based upon the two-electron oxidation of the peroxide back to oxygen. This process has proven reproducible and has led to the development of commercial biosensors for a variety of substrates including glucose, lactate, ethanol, and glutamate (6,7).

Gen 1 biosensors are dependent on dissolved oxygen concentration in solution which is 18-20%, but in tissue it reduces to 5% or less (1,8). Also, the peroxide generated in this process is a reactive species and can degrade or react with other species. To overcome these problems, a Generation 2/Gen 2 biosensor was introduced that uses artificial mediators such as ferrocenes, osmium salts, organic dyes, quinones, and a variety of ferri/ferrocyanides to accept electrons. Thus, the mediator takes the place of oxygen in a Gen 1 biosensor (9-14). A significant advantage of using a Gen 2 biosensor is that the mediators are not dependent on oxygen concentration and by selecting a proper mediator, the working potential of the electrodes can be fine-tuned to remove any electrochemical interference from any unwanted species (12,15). One can also make the electrode pH insensitive by choosing a mediator with a low overpotential for regeneration. In some cases,

mediators can be more reactive and more stable than oxygen. While both artificial mediators and oxygen must first react with the enzyme before diffusion to the electrode, an artificial mediator may enjoy greater stability, result in more mediator at the electrode surface, which in turn results in a higher electrochemical signal (16-18).

A Generation 2.5/Gen 2.5 biosensor has been introduced wherein a dehydrogenase enzyme has a mediator directly tethered to the enzyme to support quasi-direct electron transfer (quasi-DET) to the electrode surface (19). This type of mediated modified enzyme was introduced in Chapter 2 of this dissertation (see Figure 2-10) where HaDHR was modified with Fc-maleimide to produce a construct that was capable of quasi-direct electron transfer in the absence of any other mediator. This type of modified enzyme can be free in solution or as disclosed in this Chapter potentially tethered directly to the electrode surface. As shown in Chapter 2 of this dissertation if the mediator modified enzyme is free in solution because diffusion to the electrode is required, which in turn is dependent upon the size of the enzyme. Larger enzymes will diffuse more slowly and give rise to a smaller signal.

A Generation 3/Gen 3 biosensor uses a dehydrogenase enzyme to directly transfer electrons from the enzyme to the electrode surface without the need for mediators or oxygen (20). A schematic representation of different generations of biosensors is shown in Figure 4-1.

The Gen 3 principle, employing dehydrogenase enzymes that can undergo direct electron transfer (DET), is the most elegant and ideal approach for use in an enzyme-based amperometric biosensors. This process must be optimized to properly orient the enzyme with respect to the electrode surface. Knowledge of the electron transfer pathway from the active site to the surface of the protein should be taken into consideration so that DET is facilitated. This is an area of active research, and several different strategies are being investigated.

Dehydrogenase enzymes have a redox cofactor (FAD or FMN) and an electron transfer subunit (an FeS cluster or heme group), that makes them capable of DET. There are several glucose dehydrogenase enzymes that exhibit this behavior (21-24). One of the most prominent and extensively studied glucose dehydrogenase enzyme that has shown a DET mechanism is the bacteria-derived flavin adenine dinucleotide dependent glucose dehydrogenase (bFADGDH) (21,23-25). Remarkable progress has been done in understanding the structure and functional relationship of bFADGDH by Sode *et al.* (26,27), who harnessed this enzyme system to construct a Gen 2.5 sensor (19).

The crystal structure of bFADGDH revealed three distinct subunits: a catalytic subunit (α) that consists of the FAD and 3Fe-4S cluster located at the surface, the electron-transfer subunit (β) which consists of three heme c cytochrome-like protein, and a small subunit (γ) respectively (28). The β-subunit showed the presence of three hemes and the α-subunit showed the presence of an 3Fe-4S cluster on the surface of bFADGDH in addition to an active site bound molecule of FAD. Sode *et al.* focused his studies on understanding the role of the γ-subunit and identified that co-expression of the γ-subunit is required for the functional expression of the α-subunit, thereby serving as a hitchhiker protein of the α-subunit (29). Based on these structural and functional analysis, several engineering strategies have been applied to understand the electron transfer pathway in bFADGDH to create an ideal enzyme for glucose sensing either using artificial electron mediators or to the electrode directly (30-33).

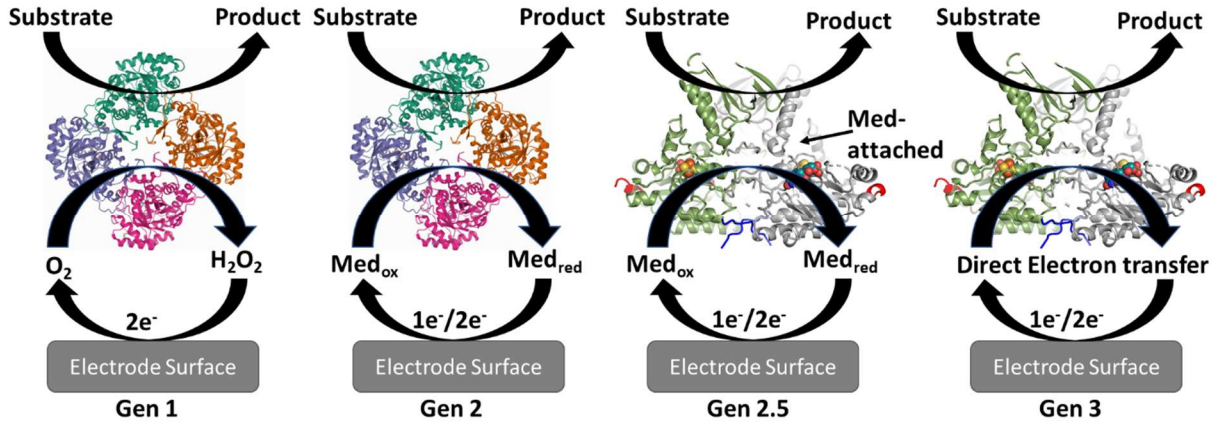

Figure 4-1 The evolution of amperometric biosensors

A Generation 1/Gen 1 biosensor uses an oxidase enzyme as a biorecognition element where oxygen acts as the electron acceptor. A Generation 2 /Gen 2 biosensor uses an oxidase or dehydrogenase enzyme coupled with an artificial mediator that serves as the electron acceptor. The artificial mediator can be either free in solution or immobilized on the electrode surface. A Generation 2.5/Gen 2.5 biosensor uses a dehydrogenase enzyme where the artificial mediator is covalently attached to the enzyme and displays quasi-DET. A Generation 3/Gen 3 biosensor uses a dehydrogenase enzyme and does not use an artificial mediator, but instead relies solely on DET to the electrode surface.

For an enzyme to be sensitive and responsive enough for DET biosensing applications, the orientation and immobilization of the biorecognition element to the electrode surface is an important design element. In addition, for long term *in vivo* biosensing applications, the enzyme should not desorb or diffuse away from the electrode surface and must achieve stable configuration. Studies with bFADGDH enzymes have shown that the electron transfer rate is highly dependent on the distance of the electron transfer between the redox site of the enzyme and the electrode (32). Current approaches fail to effectively address this problem, as enzyme inactivation or denaturation is often observed (34).

Traditional enzyme-immobilization methods utilize covalent attachment using chemical crosslinkers, such as glutaraldehyde, to attach the enzyme to the electrode surface. Chemical coupling methods using self-assembled monolayers (SAMs) of silanes and thiols which provide functional groups on the distal end of the reagent (e.g., carboxyl or amine groups) for protein binding have also been used (35,36). This method provides a strong anchor of an enzyme to the surface. However, this approach inevitably results in reduced enzyme activity. These approaches can result in loss of activity upto 90% (34,37,38). The chemical coupling method using SAMs rely on the availability and location of the surface groups on the protein for attachment. This often causes difficulty to control the protein orientation on the electrode surface due to heterogenous binding of the silane or thiol-functional group to the surface of the protein. This variation results in a mixture of active, inactive and partially active proteins on the surface and may often results in multilayer coverage depending on the protein used (39).

Over the last decade, the use of inorganic surface-recognition peptides has been introduced as an alternative to the more conventional chemical methods (40-44). The peptides are selected using combinatorial biology-based peptide phage or cell surface display libraries. The ease of genetic

fusion of these short peptide sequences into any permissive site, or to the C- or N-termini of an enzyme, offers an alternative and attractive approach for controlled enzyme orientation to support DET (40,41,44-47). In principle, this approach could provide much greater control over the assembly and the orientation process in a self-directed manner with a dissociation constant value ranging from nM to μM and has already achieved some success (40,41,44,47).

Despite considerable research, those surface-related parameters that control and define the binding of these peptides to a metal surface are still not completely understood (48-51). Studies to date are mostly related to structural or physico-chemical interactions (49,50,52-54). Ideally a set of metal binding peptides with the associated linkers would eventually be available for routine modification of enzymes for DET applications. Modification of an enzyme still requires considerable development, including optimization of the linker between the peptide and the enzyme to which the peptide is fused.

At this time, there is still no general approach to metal binding peptide modification of the enzyme that can be used in a "plug and play" fashion. This is due, in part, because a comprehensive understanding of the structure and physico-chemical contributions to metal peptide orientational control is still in its infancy. Parameters such as surface charge, buffer composition, linker sequence, and N vs C attachment of the peptide all contribute to the binding kinetics and thermodynamics of a modified enzyme. The most important contributing factor in binding of a peptide to a solid metal surface is currently believed to be electrostatic interactions (55-57). The overall contribution of these interactions to the binding of a peptides to a solid metal surface has yet to be fully investigated.

In this Chapter, we describe the engineering of HaDHR enzyme by genetic fusion to the gold (Au) or platinum (Pt) binding metal affinity peptides that have been described for other dehydrogenase

and oxidase enzymes (Table 4-1) (40,41,47,58). This study sought to leverage previously successful metal affinity peptide mediated orientational control to orient HaDHR on electrode surface for DET. The crystal structure reported in Chapter 2 of this dissertation was a necessary pre-requisite of this protein engineering effort.

HaDHR forms a homodimer with a covalently attached flavin mononucleotide (FMN) and an Fe_4S_4 cluster as two redox cofactors. The crystal structure of HaDHR, discussed in Chapter 2 of this dissertation, revealed that the homodimers are arranged in an asymmetric unit that are related by 2-fold symmetry making the C-terminals parallel to each other whereas the N-terminals are facing in opposite direction (Figure 4-2A). Based on this structural information, we engineered a fusion protein consisting of HaDHR and a C-terminal cyclic gold binding peptide (cAuBP) and a C-terminal linear three and/or five repeat platinum binding peptide (3xPtBP and/or 5xPtBP) (Figure 4-2B) (58,59). After successful engineering of these peptides with HaDHR, a variety of techniques were used to analyze the binding interactions of these fusion constructs on a metal surface. The fusion constructs were analyzed using surface plasmon resonance (SPR), atomic force microscopy (AFM), quartz crystal microbalance (QCM) and dynamic light scattering (DLS).

Table 4-1: Enzymes immobilized using metal affinity peptides

Protein Name	**Peptide Sequence**	**K_d**
Lactate dehydrogenase from *Bacillus stearothermophilus* (41)	NT-CGPWALRRSIRRQSYGPC-GGGS-bsLDH-CT	65 mM
Formate dehydrogenase from *Candida methylica* (40)	NT-CGPWALRRSIRRQSYGPC-GGGS-cmFDH-CT	64 mM
Putrescine oxidase (47)	NT-Putox-PGGG-CPGWALRRSIRRQSYGPC-CT	20 nM
MBP-Lactate Oxidase (unpublished data)	NT-SPTSTGQAPTSTGQAPTSTGQAS-GSSG-MBPLOx-CT	$<10^{-12}$
HaDHR with Au binding peptide (this study)	NT-HaDHR-SSGSSG-CPGWALRRSIRRQSYGPC-CT	$\sim10^{-6}$
HaDHR with Au binding peptide (this study)	NT-HaDHR-SGGG-CGPWALRRSIRRQSYGPC-CT	$\sim10^{-6}$
HaDHR with Pt binding peptide (this study)	NT-HaDHR-SGGG-$(PTSTGQA)_3$-CT	$\sim10^{-6}$
HaDHR with Pt binding peptide (this study)	NT-HaDHR-SGGG-$(PTSTGQA)_5$-CT	$\sim10^{-6}$

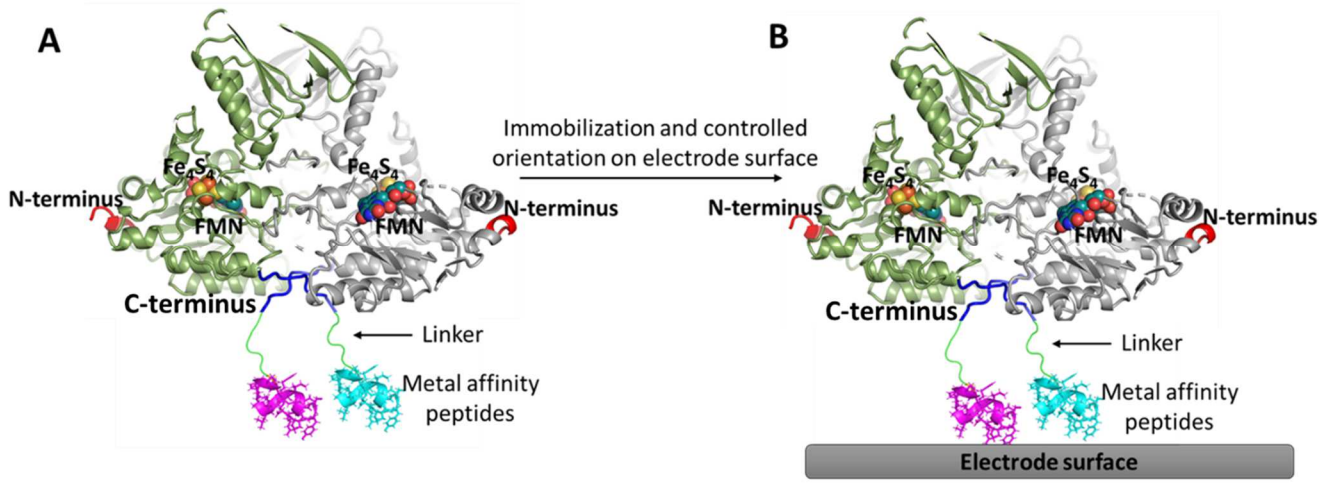

Figure 4-2 Engineering of HaDHR enzyme for controlled orientation
(A) The N-terminus (red) in an antiparallel orientation and the C-terminus (blue) in a parallel orientation of HaDHR are shown. The two redox cofactors FMN and Fe_4S_4 are also highlighted. (B) An engineered form of the enzyme where metal affinity peptides are attached to the C-terminus of HaDHR to direct the assembly to an electrode surface.

4.3 Experimental procedures

4.3.1 Materials.

Histamine, carbenicillin, chloramphenicol, Sephadex G-50 resin was purchased from Sigma Aldrich. Ni-NTA resin was purchased from Qiagen. DNaseI was purchased from Roche. The primers used in this study were obtained from Integrated DNA Technologies. DNA ligase and DpnI were purchased from Thermo Fisher Scientific. *E.coli* XL-10 Gold and BL21 (DE3) competent cells were purchased from Agilent Technologies. NuPAGE gel, 12% Bis-Tris, Invitrogen, and InstantBlue stain from Expedeon Ltd. Binding studies for cAuBP were performed on gold-coated SPR chips obtained from Cytiva Life Sciences. Binding studies for cAuBP and PtBP were performed on gold and platinum coated QCM chips obtained from Gamry Instruments. Synthetic platinum nanoparticles of various sizes were provided by Dr. Mary Beth Carter at Design-Zyme LLC.

4.3.2 Site directed mutagenesis

The surface exposed cysteine (Cys601) as informed from the crystal structure of HaDHR and highlighted in Chapter 2 were mutated to serine in *wt*-HaDHR expression plasmid ORF by using the Quick-change site directed mutagenesis kit (Agilent Technologies). Plasmid DNA was purified from mutant transformant colonies, and the mutations were validated by Sanger sequencing. This was done to avoid any non-specific binding of cysteines to either the Au or Pt surface. This will be denoted as HaDHR in this Chapter for simplicity.

4.3.3 Expression vector construction for cyclic gold binding peptide (cAuBP)

Construction of expression vectors to produce HaDHR-cAuBP-CT was performed using megaprimer insertion cloning into the pMCSG7 vector (60). The vector encoded the histamine

dehydrogenase from *Rhizobium sp. 4-9* (HaDHR) gene together with 6xHis tag on the N-terminus of the protein followed by a tobacco etch virus (TEV) cleavage site. A solubility tag GB1 was inserted in between the 6xHis tag and the TEV cleavage site to enhance protein production. Gene blocks targeted to the C terminus of the HaDHR gene were obtained commercially from Integrated DNA Technologies, as well as gene blocks encoding the cyclic AuBP (cAuBP) peptide (CPGWALRRSIRRQSYGPC) plus linker (SSGSSG) and (SGGG) sequences (40,41,47).

The megaprimer insertion cloning was performed using the T100 Thermal Cycler PCR machine and the PCR products were digested using DpnI and transformed into 50 µL of XL-10 Gold cells. Transformants were selected on 100 ug/mL carbenicillin LB agar plates that were incubated overnight at 37 °C. DNA from the transformant colonies were purified using a Qiagen miniprep kit. The DNA concentration was measured using a NanoDrop 200c spectrophotometer (Thermo Fisher Scientific) and the samples were sequenced and confirmed commercially (ACGT Inc.). The successfully sequenced constructs were then transformed into BL21 (DE3) pRARE cells for expression. The HaDHR enzyme was also transformed into BL21 (DE3) pRARE cells for side-by-side comparison and production.

4.3.4 Expression vector construction for linear platinum binding peptide (PtBP)

Construction of expression vectors to produce HaDHR-5xPtBP-CT was performed using megaprimer insertion cloning on the pMCSG7 vector (60). The gene block encoding the five repeats of the linear Pt binding peptide (PTSTGQA) plus linker (SGGG) sequence was prepared (58). The megaprimer insertion cloning was performed in the similar manner as above.

HaDHR-3xPtBP-CT construct was prepared by using non-overlapping PCR protocol and the PCR reaction was run using HaDHR-5xPtBP-CT as the template. PCR was performed and the PCR products were then ligated using KLD mix (New England Biolabs) and transformed into 50 µL of

XL-10 Gold cells. The transformants were treated the same way as above. The successfully sequenced constructs were transformed into BL21 (DE3) pRARE cells for expression.

4.3.5 Protein expression and purification

Transformant starter cultures of BL21 (DE3) pRARE were grown overnight at 30 °C in a shaker incubator in 10 mL Luria Bertani (LB) broth containing 100 µg/mL carbenicillin and 25 µg/mL chloramphenicol. Next day, a large-scale protein expression was performed by adding the overnight culture into 1L of enhanced LB medium (100 µg/mL carbenicillin, 0.8% (v/v) glycerol, 10 mM $MgCl_2$) and incubated at 37 °C until it reached an optical density (OD_{600}) of ~0.6-0.8 at a shaking speed of 300 rpm. The cultures were induced with 0.1 mM isopropyl β-D-1-thiogalactopyranoside (IPTG) and 0.5% (v/v) glycerol and were incubated overnight at 15 °C with constant shaking at 300 rpm. Cells were chilled to 4 °C and harvested by centrifugation at 5000 x g for 10 min. Cell pellets were resuspended in 100 mL lysis buffer (50 mM potassium phosphate, pH 7.4, 0.15 M NaCl and 5 mM imidazole) and frozen at -80 °C overnight. Cell suspensions were thawed, 5 U/mL DNaseI was added and incubated on ice for 10 min and then sonicated in an ice water bath for 4 min using an alternating 2 sec on/10 sec off duty cycle at 30% amplitude. Lysate was clarified by centrifugation at 20,000 x g for 60 min at 4 ºC. The soluble cell fraction was gently mixed with 3 mL of Qiagen Superflow Ni-NTA resin equilibrated with lysis buffer. The resin slurry was loaded onto a 1.6 cm x 30 cm column (Biorad) and washed with 10 column volumes of lysis buffer followed by 10 column volumes of lysis buffer containing 20 mM imidazole. The protein was eluted with 1.5 column volumes of lysis buffer containing 250 mM imidazole. The lysis buffer contained 250 µM TCEP for the cAuBP constructs to avoid any aggregation due to cross-linking of Cys residues present at the ends of the engineered construct.

The eluate from the Ni-NTA column was treated with tobacco etch virus (TEV) protease to remove the 6xHis and GB1 tag in the lysis buffer containing 5 mM Dithiothreitol (DTT) and 1 mM EDTA. The TEV protease was added to a 1:5 (TEV: protein) molar ratio. The reaction mixture was incubated for two days at 4 °C. Gel filtration on Sephadex G50 was performed to remove DTT and EDTA. The protein was then subjected to a Ni-NTA column. The tag-less protein that was collected in the flow through was >95% pure as judged by SDS-polyacrylamide gel electrophoresis (SDS-PAGE). The protein was concentrated by ultrafiltration (Amicon Ultra-15 concentrator) and loaded onto a 1.6 x 60 cm Superdex 200 Increase GL column at a flow rate of 1.0 mL/min. Peak fractions containing the HaDHR-cAuBP-CT, HaDHR-5xPtBP-CT, and HaDHR-3xPtBP-CT dimers were pooled. Glycerol was added to 20% (v/v) and the protein was snap frozen in liquid nitrogen and stored at -80 ^{o}C.

4.3.6 Surface Plasmon Resonance (SPR) measurements for cAuBP construct

The binding kinetics of HaDHR and HaDHR-cAuBP-CT were performed using a four channel Biacore T200 SPR instrument (GE Healthcare). The buffer solutions were degassed to avoid any bubble formation in the flow cell. A stable baseline was established by flowing 10 mM Tris-HCl buffer, pH=7.5 over the gold surface. HaDHR and HaDHR-cAuBP-CT enzyme solutions were flowed through the surface at different concentrations (0.1 μM - 5 μM) and their adsorption was monitored. The temperature within the flow cell of the SPR was kept constant at 25 °C. The solutions were introduced to the flow cell at a rate of 10 μL/min with association and dissociation phases ranging from 800s-1800s. The results were analyzed using one-site total binding model in Graph Pad Prism version 6.0 software and an estimate of K_d for the two enzymes were obtained (61). The binding kinetics of HaDHR and HaDHR-cAuBP-CT and the control protein PutOx and PutOx-cAuBP-CT were obtained at 1 μM concentration and the results were compared.

Additionally, buffer scouting experiments with 20 mM sodium phosphate buffer, pH=7.4 and 100 mM potassium phosphate buffer, pH=7.4 and kinetic measurements with 10 mM Tris-Cl, 100 mM NaCl, pH=7.5 were also performed.

4.3.7 AFM measurements for cAuBP construct

The material specificity of HaDHR and HaDHR-cAuBP-CT was studied using template-stripped gold (TSG) surfaces as substrates for protein adsorption. The surfaces were cleaned first with pH adjusted (pH=7.5) double distilled water for few seconds and then conditioned with 10 mM Tris-HCl buffer, pH=7.5. Surfaces were then dried completely under a stream of nitrogen. The enzyme concentrations were adjusted to 0.25 μM and 0.1 μM with the buffer and a volume of 100 μL of each protein sample was applied to the TSG surface, such that the surface was covered completely. This was then incubated for 1h. The surfaces were then washed with buffer for few seconds and then thoroughly with MilliQ water to remove any excess and unbound protein. The surfaces were then dried under a stream of nitrogen and imaged immediately using tapping mode AFM (Digital Instruments, NanoScope IIIa). The imaging in tapping mode was done using diamond-like carbon-coated tips (TAP300DLC, f = 300 kHz, k = 40 N/m). Typical scan rates were 1 Hz with a scan size of 1 × 1 μm or 500 nm. For high-resolution imaging, a cantilever with a 5 nm nominal radius was used to assess the topography of enzyme immobilized on the gold surface.

Dimensions of single molecules was determined using the samples that were prepared using low protein coverage (0.1 μM). Bruker-NanoScope analysis 1.5 software was used, and from each sample, 20 molecules were analyzed over three different spots (n=20 for each protein). The average length and width were measured by first identifying the “endpoint” of the protein by determining the vertical halfway point between the flat surface and the peak of the protein. The other endpoint was then determined by shifting the other measurement line until the vertical

distance was approximately zero. The horizontal distances were then recorded. The width was set as the larger values and the length as the smaller values for the cross-sections. The heights were measured by taking a cross-section of the protein and measuring the difference between the peak of the protein and a flat section adjacent to the protein. This was performed four times, twice for the length cross-section and twice for the width. The averages of these were used for the height of that protein.

4.3.8 Dynamic light scattering (DLS) measurements with Pt nanoparticles for PtBP constructs

The binding affinity of HaDHR, HaDHR-5xPtBP-CT, HaDHR-3xPtBP-CT, were measured using ~50 nm platinum (Pt) nanoparticles. The control proteins used were MBP-LOx and NT-3xPtBP-MBP-LOx (obtained from Design-Zyme LLC.). The protein concentration used was 5 μM for HaDHR and 1 μM for MBP-LOx. The appropriate protein concentrations were prepared in 1 mL of 10 mM citrate-tris buffer, pH=7.0 in a disposable plastic cuvette and the DLS measurements were recorded using a Malvern Zetasizer Nano ZS90. 50 μL of Pt nanoparticles were added in the solution and was incubated for 1h. The DLS measurements were recorded again after incubation and a shift in the Z-average and the peak size in presence of the nanoparticles was observed.

4.3.9 Quartz-crystal microbalance (QCM) measurements for cAuBP and PtBP constructs

HaDHR, HaDHR-cAuBP-CT, and HaDHR-3xPtBP-CT stock solutions were prepared for QCM analysis by desalting the protein using Sephadex G-50 fine gel filtration columns into 10 mM Tris-Cl, 100 mM NaCl, pH=7.4. The protein was then filtered through a 0.2 μm filters (Millipore, Ultrafree-MC, 0.5mL). The concentration of the protein samples was adjusted to ~1 μM with freshly degassed buffer. Au and Pt QCM sensors (5 MHz, Gamry Instruments) were rigorously cleaned, mounted in flow cell, and equilibrated with the same buffer for ~2h. A nominal sensitivity

of 5 MHz for these QCM sensors as supplied by Gamry was used. Gamry's eQCM 10M system was used and once the sensors achieved baseline stability the data was collected. Protein solutions were passed over the equilibrated sensors at a flow rate of 200 μL/min at room temperature. An Ismatec Reglo (SK-78018-14) digital 2-channel 12-roller pump with MasterflexLive, 115/230VAC perfusion pump was used to deposit the enzymes over the QCM chips.

4.4 Results

4.4.1 Fusion Protein constructs with cAuBP

Gold binding peptides that were previously characterized and has shown high specificity and affinity for binding to gold surfaces were chosen for this study (40,41,47). Cyclic gold binding peptides (cAuBP) were incorporated by using cysteinyl residues together with a short linker sequence attaching the peptide to the C-terminal. Fusion proteins were engineered into the pMCSG7 vector (Figure 4-3A), such that the cAuBP was attached with a linker to the C-terminal end of HaDHR. Previous studies had used a SGGG linker between the protein and the cAuBP, and this version of the linker was used for some initial control studies. Based on a molecular modelling study (62) an apparently more flexible six amino acid linker (SSGSSG) was also investigated in this study (Figure 4-3B).

HaDHR was engineered with an IgG B1 binding domain of Protein G (GB1) (63-65) solubility tag into the N-terminus, so that a soluble, recombinant form of the protein could be produced. The GB1 tag was introduced before the TEV (Tobacco etch virus) protease cleavage site so that the 6xHisGB1 tag could be cleaved from the protein following purification. The soluble fractions of the proteins were obtained during purification as shown in Figure 4-3C. The SDS-PAGE gel analysis showed that the proteins were ~>95% pure after affinity column purification and TEV cleavage. The multiple higher band before cleavage might be due to some aggregate or dimer formation. The proteins underwent a final size exclusion chromatography (SEC) purification step prior to characterization of the engineered construct by SPR, AFM and QCM.

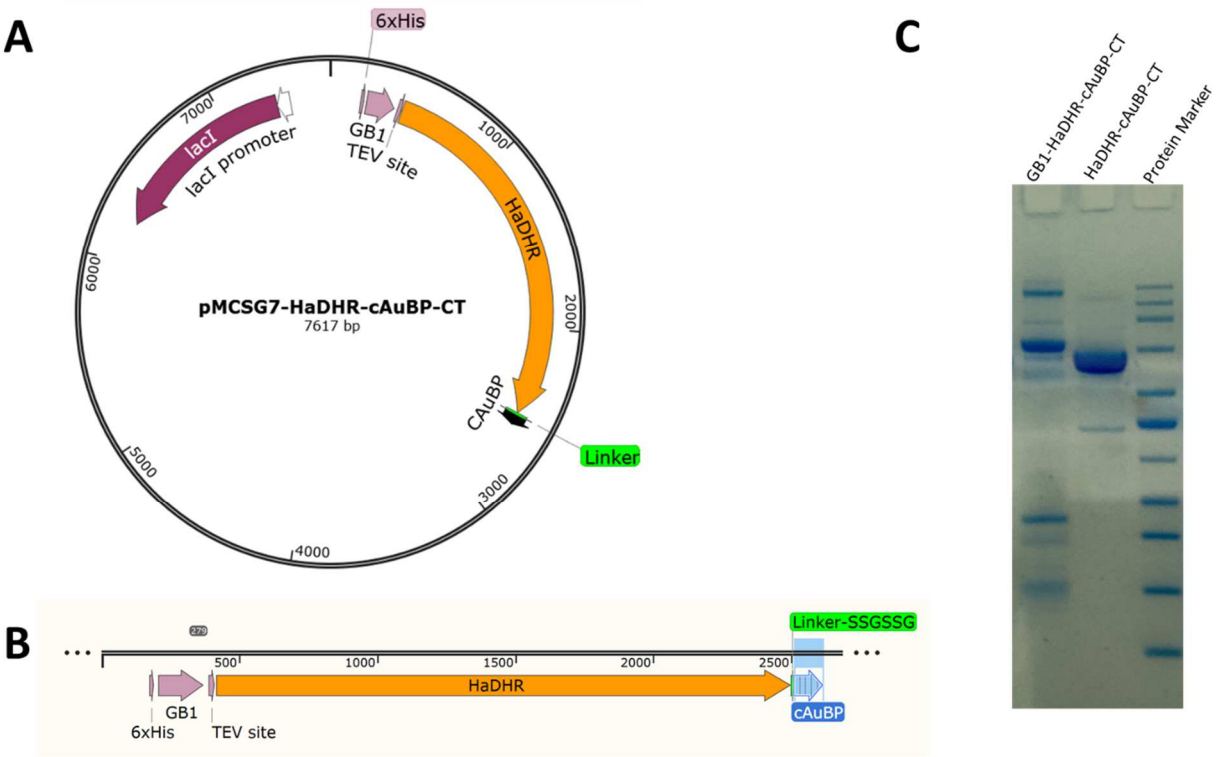

Figure 4-3 Vector map and SDS-PAGE gel images for cAuBP constructs
(A) A vector map showing the fusion protein construct in pMCSG7 vector, (B) A linear sequence map showing the fusion protein construct with cAuBP at the C-terminal attached through a linker, and (C) SDS-PAGE gel image after protein purification and cleavage of 6xHisGB1 tag. Molecular weight estimated for GB1-HaDHR-cAuBP-CT is ~79 kDa and for HaDHR-cAuBP-CT is ~78.3 kDa.

4.4.2 Fusion Protein constructs with PtBP

A high-affinity seven amino acid PtBP sequence (PTSTGQA) reported by Tamerler *et al.* was chosen for this study (58). This linear platinum binding peptide (PtBP) was identified via a phage display selection (58). Previous studies have suggested that repeats of this sequence may improve binding for some enzymes (66). Note that this sequence does not contain a cysteinyl residue.

A four amino acid linker (SGGG), described by Tamerler *et al.* was used for all platinum binding peptide constructs (40,41). Two constructs, one with a three repeat of the PtBP sequence (3xPtBP) and other with a five repeat of PtBP sequence (5xPtBP) were prepared by integrating the PtBP sequence with the linker onto the C terminus of HaDHR. Fusion proteins were cloned into the pMCSG7 vector as shown in Figure 4-4A.

The linear sequence map showing the final construct consisting of a 6xHis, a GB1 solubility tag, a TEV cleavage site, the HaDHR protein and, the C-terminal 3xPtBP/5xPtBP sequence attached to the protein via a four amino acid linker is shown in Figure 4-4B. The proteins were expressed and purified in the soluble form as shown in the SDS-PAGE gel image (Figure 4-4C). The SDS-PAGE gel analysis showed the proteins to be >95% pure after the affinity column purification. The fusion protein constructs were further purified using SEC. The engineered proteins were characterized via DLS with Pt nanoparticles and QCM on Pt sensor chips, to examine the binding interactions to Pt surfaces.

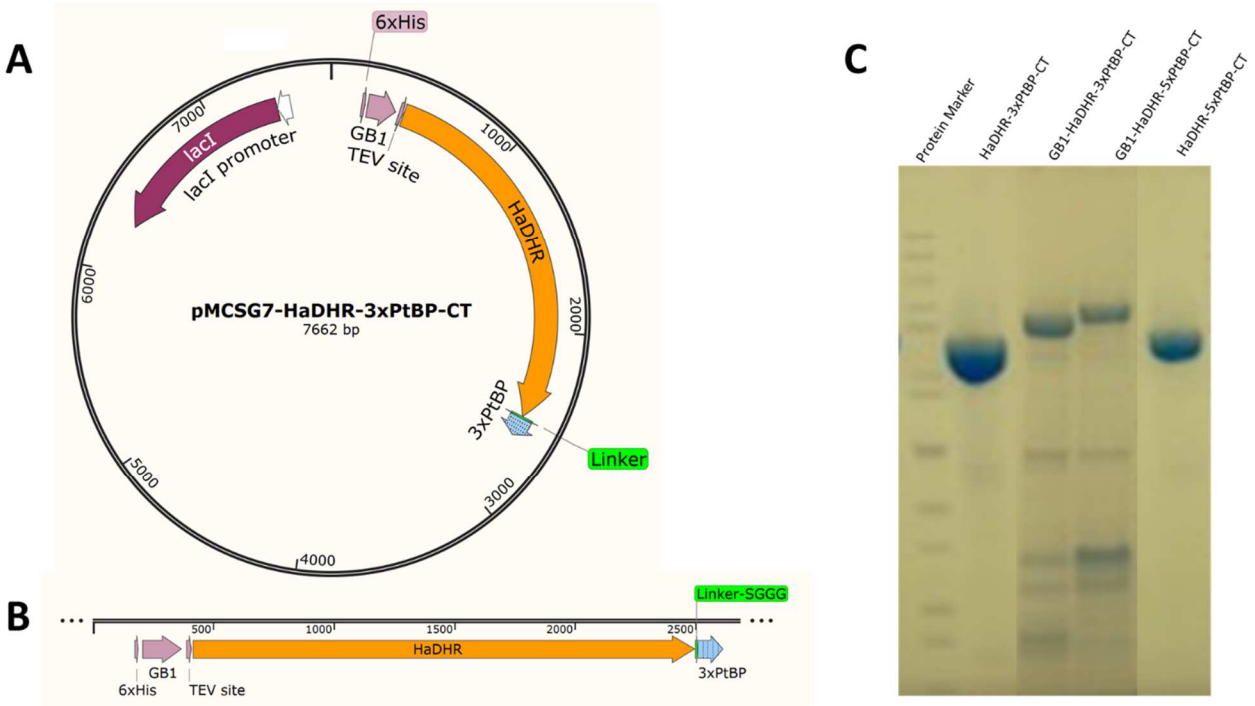

Figure 4-4 Vector map and SDS-PAGE gel images for PtBP constructs

(A) A vector map showing the fusion protein construct in pMCSG7 vector, (B) A linear sequence map showing the fusion protein construct with 3xPtBP at the C-terminal attached through a linker, (C) SDS-PAGE gel image after protein purification and cleavage of 6xHisGB1 tag for both the 3xPtBP and 5xPtBP constructs. Molecular weight estimated for GB1-HaDHR-3xPtBP-CT is ~87.8 kDa, GB1-HaDHR-5xPtBP-CT is ~89 kDa, HaDHR-3xPtBP-CT is ~78.9 kDa, and HaDHR-5xPtBP-CT is ~80.2 kDa

4.4.3 Binding analysis using SPR for cAuBP constructs

Binding interactions of HaDHR and HaDHR-cAuBP-CT on gold surface were analyzed by SPR using the buffer employed for previously described PutOx results (47). Two phosphate buffers, 20 mM sodium phosphate buffer, pH=7.4 and 100 mM potassium phosphate buffer, pH=7.4, were used for studying the binding interactions of HaDHR and HaDHR-cAuBP-CT at 1 μM concentration (Figures 4-5A and 4-5B). Neither buffer condition resulted in any improvement in gold surface binding of cAuBP tagged proteins compared to HaDHR. While the lower ionic strength buffer showed slight differences in binding between the HaDHR and HaDHR-cAuBP-CT protein, a significant decrease in binding of the cAuBP tagged proteins was observed at the higher ionic strength buffer on the gold surface.

Previous studies of cAuBP peptides attached to other dehydrogenase proteins used a buffer consisting of 10 mM Tris-Cl, pH=7.5 (41,44). The binding of the PutOx and PutOx-cAuBP-CT, two control proteins, were examined using this buffer, and the results are shown in Figure 4-5C. Consistent with the data published in a phosphate buffer system (47), at a concentration of 1 μM, the PutOx-cAuBP-CT showed better binding to a gold surface as measured by SPR compared to PutOx. The former was shown in a phosphate buffer to preferentially bind to a gold surface with a nM K_d. This binding preference is also shown in Tris-buffer, and these results verified the proper functioning of the SPR setup.

Kinetic measurements at different protein concentrations (0.1 μM- 5 μM) were examined for both the HaDHR and HaDHR-cAuBP-CT in 10 mM Tris-Cl, pH=7.5 buffer (Figure 4-5D) to calculate the equilibrium dissociation constant (K_d). No hyperbolic binding curve was observed for the HaDHR control, and only a partial hyperbolic curve for HaDHR-cAuBP-CT was obtained. K_d determined from the experimental binding isotherms were ambiguous for HaDHR, but a K_d of

~0.4 μM was obtained for the HaDHR-cAuBP-CT protein. The binding curves suggested that 1 μM might be a good concentration for detailed SPR studies. The dissociation results were not analyzed for any of these response curves because the association rate constants were too slow to warrant further analysis.

At a concentration of 1 μM, HaDHR and HaDHR-cAuBP-CT showed essentially the same response curves (Figure 4-5E). This might be because of protein aggregation, the metal affinity peptides may be interacting with the protein and therefore not available for binding, sterically shielded by the protein to prevent interactions with the gold surface or not properly aligned in a productive conformation to allow for binding to the gold surface. Since the Tris-buffer alone did not show any difference in binding between the two constructs, similar kinetic experiments were performed by adding 100 mM NaCl to the Tris-buffer (Figure 4-5F). The concentration dependent SPR binding curves showed a good hyperbolic response for both HaDHR and HaDHR-cAuBP-CT proteins with a saturation at ~5 μM. The K_d for binding was calculated to be ~1 μM for HaDHR whereas for HaDHR-cAuBP-CT it was found to be ~0.4 μM similar to that obtained using 10 mM Tris-Cl, pH=7.5. At this time, we were unable to continue with more detailed SPR studies as the access to the equipment was no longer available due to its failure and lack of funds to repair the system. While these studies are incomplete and potentially inconclusive, the preliminary suggestion is that binding may preferentially occur for the HaDHR-cAuBP-CT construct on a gold surface in a tris-buffer system with salts present. The importance of specific vs non-specific binding is considered more fully in the discussion section below (*vida infra*).

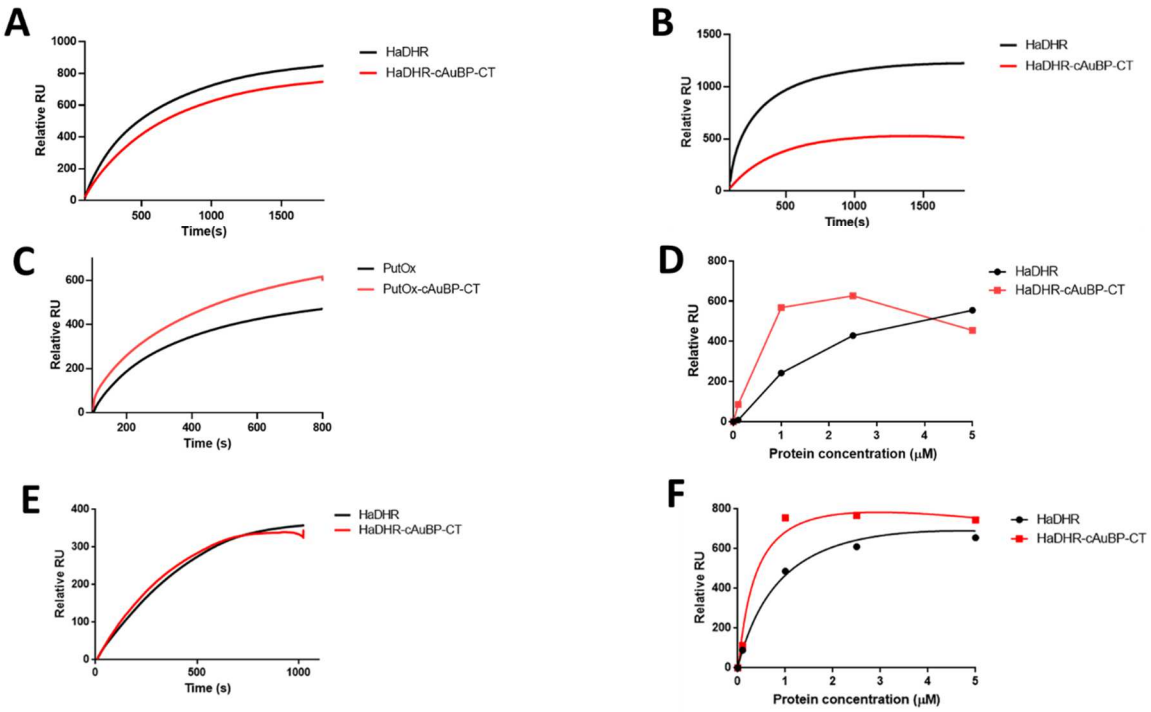

Figure 4-5 SPR response curves in phosphate and tris buffers

(A) Response Units (RU) vs time curves for HaDHR (black) and HaDHR-cAuBP-CT (red) at 1 μM concentration using 20 mM sodium phosphate buffer, pH=7.4, (B) RU vs time curves for HaDHR (black) and HaDHR-cAuBP-CT (red) at 1 μM concentration using 100 mM potassium phosphate buffer, pH=7.4. (C) RU vs time curves for PutOx (black) and PutOx-cAuBP-CT (red) at 1 μM concentration using 10 mM Tris-Cl, pH=7.5. (D) Response units (RU) vs concentration curve for the kinetic experiments using HaDHR (black) and HaDHR-cAuBP-CT (red) proteins at varying concentrations (0.1 μM- 5 μM) using 10 mM Tris-Cl, pH=7.5. (E) RU vs time curves for HaDHR(black) and HaDHR-cAuBP-CT (red) at 1 μM concentration using 10 mM Tris-Cl, pH=7.5. (F) RU vs concentration curve for the kinetic experiments using HaDHR (black) and HaDHR-cAuBP-CT (red) proteins at varying concentrations (0.1 μM- 5 μM), using 10 mM Tris-Cl and 100 mM NaCl, pH=7.5.

4.4.4 AFM measurements for cAuBP construct

Binding studies via SPR indicated that HaDHR and HaDHR-cAuBP-CT binds in a similar manner on the gold surfaces when performed using 10 mM Tris-Cl, pH=7.5 buffer. To further probe the interactions of these proteins with a gold surface, AFM studies were performed on template-stripped gold surfaces (TSG). Protein films were imaged in air after protein adsorption for 1h at a concentration of 0.25 μM. The images were collected in tapping mode as shown in Figures 4-6A and 4-6B. HaDHR (Figure 4-6A) showed a slightly lower surface coverage compared to HaDHR-cAuBP-CT (Figure 4-6B) as seen from AFM images. Higher aggregates and bigger protein particles were also observed in HaDHR-cAuBP-CT protein images. Individual protein particles are indicated by a white arrow.

Dimensions of single molecules of protein can be determined using AFM images from low-coverage conditions. Figure 4-6C shows single molecule of protein along with the cross-sectional profiles through the protein bound to the gold surface as indicated by white line. For each sample, 20 molecules were analyzed and the length, width (FWHM) and the height of the proteins were determined. As shown in Figure 4-6D, the length, width, and height of HaDHR and HaDHR-cAuBP-CT were very similar and no significant difference in dimensions were observed. These binding interaction studies strongly suggest that the presence of cAuBP tag is not showing any effect on the binding to the gold surface.

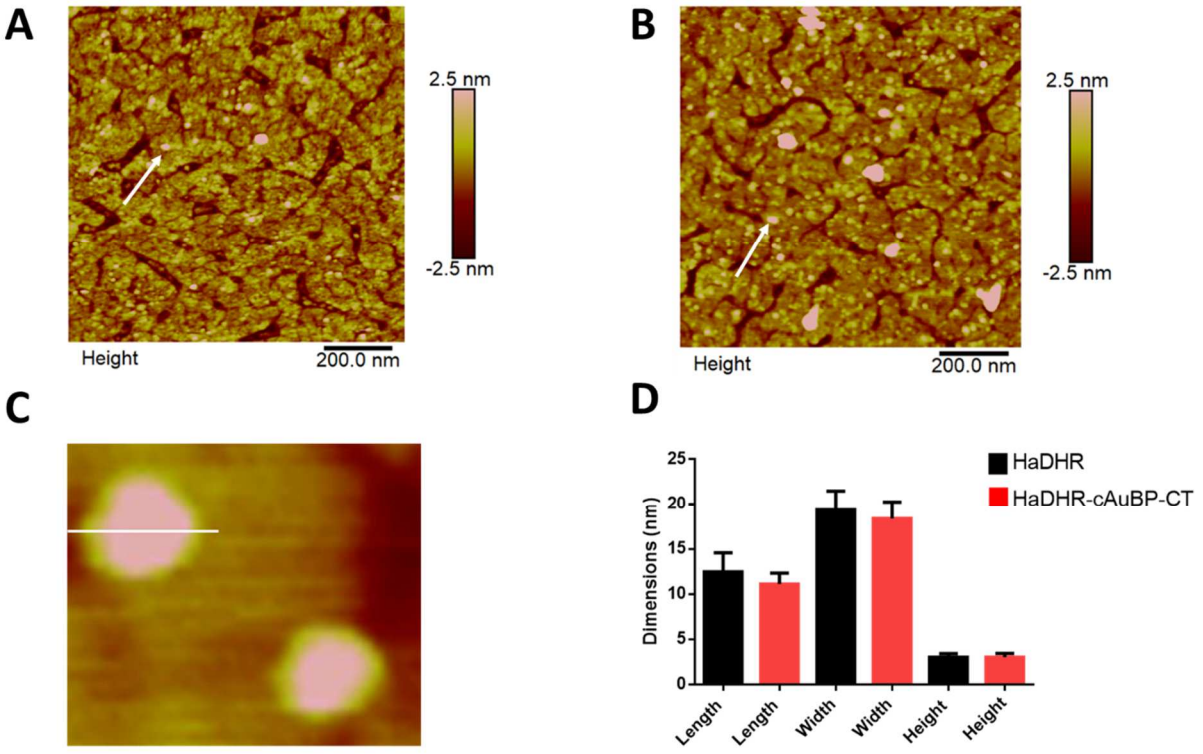

Figure 4-6 AFM images under ambient conditions
(A) HaDHR and (B) HaDHR-cAuBP-CT at 0.25 μM concentration on Au surfaces, respectively. White arrows show some individual molecules. (C) AFM images of individual molecules of protein along with the cross-sectional profiles as indicated by white line through the protein bound to the Au surface for HaDHR, (D) AFM-measured dimensions of HaDHR and HaDHR-cAuBP-CT on Au. The dimensions are from a single experiment taken at three different locations for n=20 individual protein molecules.

4.4.5 Dynamic light scattering (DLS) measurements with Pt nanoparticles for PtBP constructs

Given the complications with SPR studies, the use of a platinum binding peptide (PtBP) to target a platinum metal surface was also explored (58). The use of platinum in biosensor fabrication is established (67-71), and in some instances offers better *in vivo* lifetimes compared to biosensors based on gold surfaces (72,73). PtBP have been used to successfully modify enzymes for biosensing applications (58). During this study, access to a range of well-defined, well characterized, Pt nanoparticles became available, which facilitated the use of DLS to characterize platinum binding by a PtBP. These nanoparticles were synthesized by Design-Zyme LLC, in a variety of sizes and the 50 nm particles were made available for this study (66,74). The procedure to synthesize the nanoparticles is considered a trade secret by the company. Previous studies on a 3xPtBP version of MBP-LOx showed that the modified enzyme bound to platinum surfaces with an apparent $K_d < 10^{-12}$ (66).

Preliminary studies with HaDHR-PtBP constructs were performed using well defined ~50 nm Pt nanoparticles. For this study, MBP-LOx with and without PtBP tags were used as control proteins. After incubating the proteins with Pt nanoparticles for 1h, DLS measurements were performed and the change in the overall Z-average and individual peak size was reported (Table 4-2). The increase in overall Z-average for MBP-LOx without and with 3xPtBP tag was found to be ~9 nm and the shift in individual peak size was ~10 nm showing that the 3xPtBP-MBP-LOx is binding to the Pt nanoparticles (Figure 4-7A).

The overall Z-average for HaDHR without and with PtBP tags showed a decrease of ~1 nm. By contrast, the individual peak size showed a shift of ~3 nm between HaDHR and HaDHR with PtBP tags. The images showing the individual peak shift for the three proteins are shown in Figure 4-7.

The proteins in the absence of Pt nanoparticles do not show any significant size change as demonstrated by the overlapping peaks (green and red, Figure 4-7). The peaks for HaDHR without and with PtBP tags (black and pink, respectively), show a smaller shift as compared to the MBP-LOx proteins when incubated with the nanoparticles (Figures 4-7B and 4-7C). These DLS results were not as conclusive as hoped. The details of how the nanoparticle size changes on protein binding is considered more fully in the discussion section below (*vida infra*).

Table 4-2: DLS analysis showing Z-average and individual peak size

Construct bound with ~50 nm Pt nanoparticles	**Z-average (d.nm)**	**Δ Z-average (d.nm)**	**Peak size (d.nm)**	**Δ Peak size (d.nm)**
MBP-LOx (control)	73.58	-	62.90	-
3xPtBP-MBP-LOx (control)	82.68	9.1	73.16	~10
HaDHR	78.65	-	64.85	-
HaDHR-3xPtBP-CT	77.25	1.4	67.63	~3
HaDHR-5xPtBP-CT	77.48	1.2	67.35	~2.5

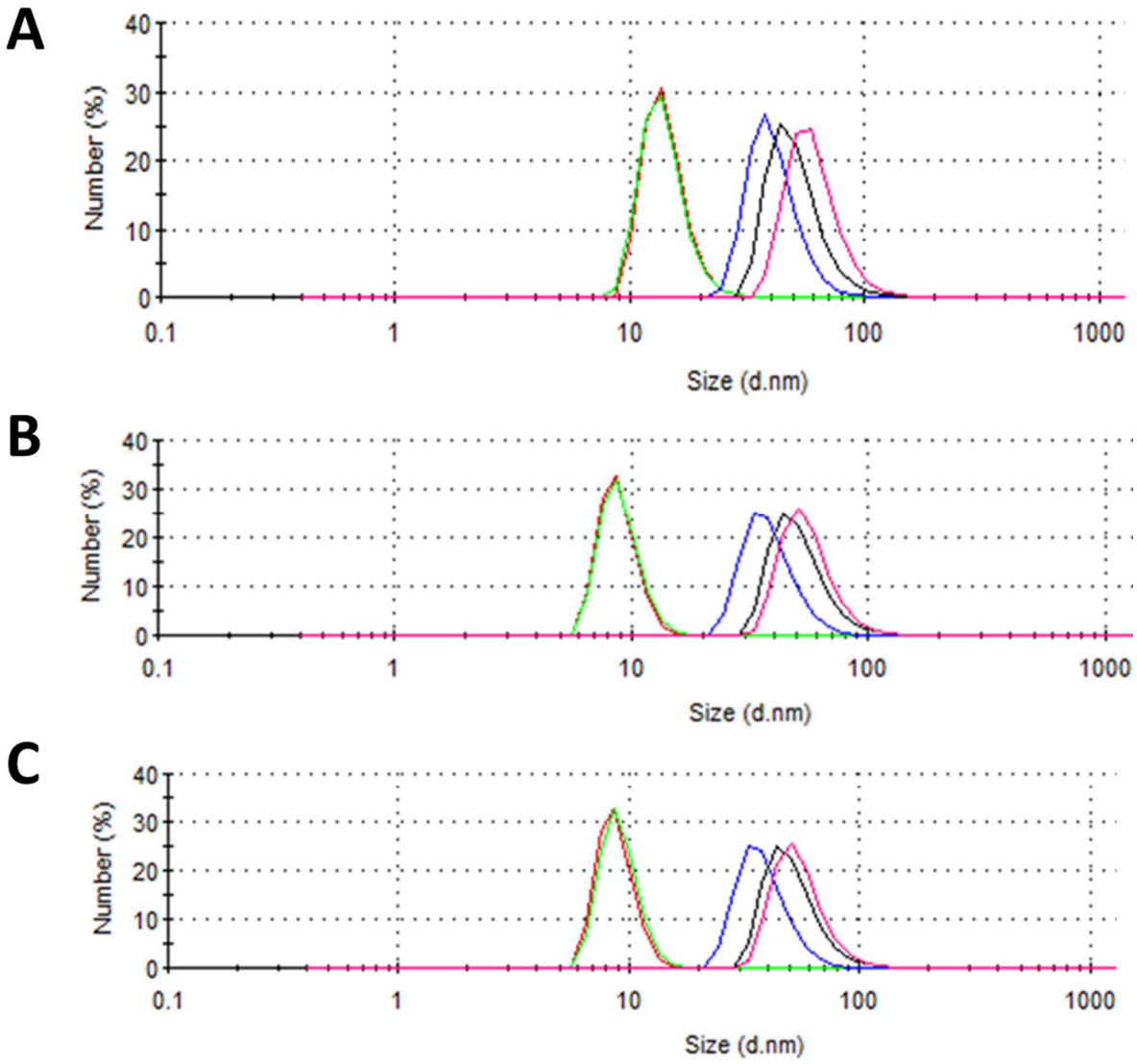

Figure 4-7 DLS response of PtBP modified enzymes
For all DLS traces, the following color-coding scheme was used: proteins without a PtBP tag are in red; proteins with a PtBP tag are in green; nanoparticles in the absence of protein are in blue; proteins without a PtBP tag incubated with nanoparticles are shown in black; proteins with a PtBP tag incubated with nanoparticles are shown in pink. Incubation time was 1 h. (A) MBP-LOx and NT-3xPtBP-MBP-LOx (1 µM concentration, respectively), (B) HaDHR and HaDHR-3xPtBP-CT (5 µM concentration, respectively), and (C) HaDHR and HaDHR-5xPtBP-CT (5 µM concentration, respectively).

4.4.6 Binding analysis using QCM for cAuBP and PtBP constructs

The SPR studies on the HaDHR-cAuBP-CT construct gave promising kinetic results using 100 mM NaCl in 10 mM Tris-Cl, pH=7.5 buffer. QCM experiments in this buffer were performed (Figure 4-8). Only the easier to obtain HaDHR-3xPtBP-CT construct was studied by QCM as both HaDHR-3xPtBP-CT and HaDHR-5xPtBP-CT showed similar peak shifts via DLS.

By QCM, the interactions between HaDHR and HaDHR-cAuBP-CT on a gold surface (Figure 4-8A) and between HaDHR and HaDHR-3xPtBP-CT on a platinum surface (Figure 4-8B) were investigated. The change in frequency was recorded as a function of time. Binding isotherms at a protein concentration of ~1 μM were collected for cAuBP and PtBP constructs.

The preliminary results showed that HaDHR-cAuBP-CT binds with higher affinity to a gold surface compared to HaDHR. The results also suggest that the HaDHR protein construct with cAuBP peptide tag might be binding in a targeted manner compared to what is seemingly non-specific binding of HaDHR on the gold surface. Note, the QCM experiments were done using 10 mM Tris-Cl, 100 mM NaCl, pH=7.5 buffer which was different from the buffer used in SPR and AFM studies. The primary difference is the ionic strength which is higher in Tris buffer used in the QCM studies.

QCM studies on HaDHR-3xPtBP-CT construct showed an initial targeted binding to a platinum surface as compared to HaDHR, which is seemingly lost over time as observed in Figure 4-8B after ~1500s, where the binding isotherm switches from a specific binding signature to a non-specific binding signature. In addition, NT-3xPtBP-MBP-LOx protein were also studied to ensure the proper functioning of the QCM setup (Figure 4-8C).

The HaDHR protein construct without any metal binding peptide to the gold and platinum surfaces showed a similar change in frequency as a function of time (Figures 4-8A and 4-8B). The results also suggested that the PtBP constructs may be binding more slowly and with lower affinity to the electrode surface in compared to cAuBP protein constructs in the buffer used for these experiments.

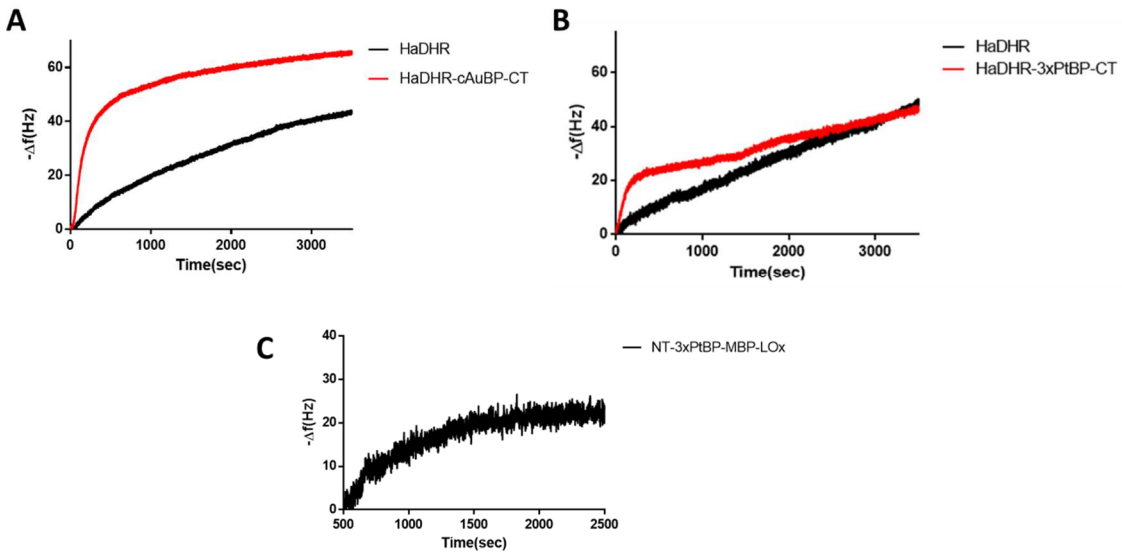

Figure 4-8 QCM measurements on cAuBP and PtBP constructs
All experiments were performed in 10 mM Tris-Cl, 100 mM NaCl, pH=7.5 buffer. (A) HaDHR (black) and HaDHR-cAuBP-CT (red) at ~1 μM protein concentration, (B) HaDHR (black) and HaDHR-3xPtBP-CT (red) at ~1μM protein concentration**.** All experiments were performed in 10 mM Tris-Cl, 100 mM NaCl, pH=7.5 buffer. (C) NT-3xPtBP-MBP-LOx were used as control proteins at a concentration of ~120 nM.

4.5 Discussion

Immobilization and orientation of the enzymes on a transduction element is an important criterion for development of an amperometric biosensor. This study describes the preliminary engineering of HaDHR enzyme with noble metal affinity peptides to achieve controlled orientation and immobilization on the electrode surface for *in vivo* histamine biosensing applications.

HaDHR enzyme was engineered with the noble metal affinity peptides that have been used earlier by Tamerler *et al*. The successful use of cyclic gold binding peptides (cAuBP) in different dehydrogenase and oxidase enzymes with high specificity and high affinity for gold surfaces have been shown previously by Tamerler *et al*. (Table 4-1). Based on these observations, two fusion protein constructs were prepared with two different linker lengths for HaDHR enzyme incorporating cAuBP peptides at the C-term (Figure 4-2). A simplistic explanation for this observation is as follows: since cAuBP-tag involves Cys residues at their ends for cyclization, two additional fusion constructs were prepared with linear platinum binding peptides (PtBP) to probe whether the length of the metal binding peptide and the absence of cysteine residues affects binding to a metal surface, ofcourse there are many more differences than those just described. More importantly, and for the purposes of enzyme engineering the use of metal binding peptide in one system should not be expected to readily work in another system.

The modified HaDHR enzymes were genetically engineered to incorporate either a gold or platinum binding peptide on the C-term with an expectation that these peptide tags will effectively interact with the metal surface. To ensure that these fusion enzymes express as soluble fractions, a solubility tag GB1 was incorporated at the N-term of the vector pMCSG7, and the enzymes were characterized using SDS-PAGE gel electrophoresis (Figures 4-3 and 4-4). Removal of the GB1 solubility tag was achieved via TEV cleavage.

Surface exposed cysteines are known to form gold-sulfur covalent bonds to a gold surface (75,76), whereas such covalent bonds are less universal for platinum surfaces. The surface exposed Cys601 residue that was identified in the crystal structure of HaDHR in Chapter 2 of this dissertation was mutated to a serine for these studies. All constructs, including the *wt*-HaDHR control, had this mutation present. This mutation ensured that non-specific binding of the metal binding peptide constructs was reduced, especially for gold surfaces.

Non-specific binding, where the binding of the protein can occur randomly on the surface without any fixed orientation or control, often has low binding affinity thereby resulting in delamination over time. Even though non-specific binding can show K_d's in μM range, the phenomenon cannot be controlled, nor can binding affinities be optimized. Also, non-specific binding usually results in multilayers of enzymes on the surface. This can result in low electrochemical signal, that is subject to change as the enzyme delaminates. By contrast, specific binding can control orientation and lead to higher binding affinities that can be nM or better. The problem of delamination can also be avoided via peptide mediated specific binding and the layering of enzymes on a surface can be better controlled.

The HaDHR-cAuBP-CT construct was engineered with a six amino acid linker (SSGSSG) between the C-terminus of the enzyme and the metal binding peptide. Most other metal binding peptide modified enzymes use a linker to allow for conformational mobility of the peptide, which in turn promotes better binding to the metal surface. This also reduces the propensity of the metal binding peptide to interact with the protein as opposed to the metal surface. Depending on the length of the linker used, the affinity of the metal binding peptide to the metal surface might also be affected.

Initial binding interactions of unmodified HaDHR and HaDHR-cAuBP-CT constructs were performed via SPR in both low and high ionic strength phosphate buffers. The latter buffer was similar to the buffer system used to investigate a PutOx-cAuBP enzyme system (47). In both buffer systems, HaDHR-cAuBP-CT showed no discernible improvement in gold binding affinity relative to the unmodified HaDHR protein (Figures 4-5A and 4-5B). The low ionic strength buffer showed slight decrease in binding of the HaDHR-cAuBP-CT construct on the gold surface compared to unmodified HaDHR (Figure 4-5A). By contrast, a significant decrease in binding of HaDHR-cAuBP-CT compared to the unmodified HaDHR was observed in the higher ionic strength buffer (Figure 4-5B). These studies suggest that ionic strength, e.g. salt concentration, may play an important role in mediating interactions of the cAuBP peptides to a gold surface.

HaDHR proteins with and without tags have a pI of ~6 and the pH of the buffers used were ~7.4, suggesting that overall net charge of the proteins is negative. The observed decrease in binding affinity as a function of ionic strength highlights the importance of attractive electrostatic interactions. The lack of productive electrostatic interactions between the cAuBP and the gold surface may be one explanation for the lack of gold affinity for the HaDHR-cAuBP-CT protein. Preliminary computational modelling studies and short simulations on the HaDHR-cAuBP-CT construct bound to a gold surface, also suggests that the construct has a propensity to bind to the surface. In the short simulations performed, the construct showed a tendency to orient towards the gold surface irrespective of the presence of a gold binding peptide, suggesting that non-specific binding may also play a role in the association to the gold surface.

SPR experiments in a 10 mM Tris-Cl, pH=7.5 buffer was also performed. This buffer system has been previously used to investigate other metal binding peptide mediated processes for dehydrogenase enzymes (40,41). For this buffer system, PutOx and PutOx-cAuBP-CT were used

as control proteins, which were readily available for this study. The behavior of these proteins in a phosphate buffer system showed that the PutOx-cAuBP-CT had higher specific affinity for a gold surface compared to the unmodified protein (47). PutOx-cAuBP-CT showed similar improvements in binding affinity compared to the unmodified protein in 10 mM Tris-Cl, pH=7.5 (Figure 4-5C). A preliminary K_d value of ~0.4 μM for HaDHR-cAuBP-CT construct was obtained via SPR, but a true K_d value was not determined (Figure 4-5D). The binding isotherms suggested 1 μM to be appropriate concentration for detailed SPR analysis.

At 1 μM concentration, the SPR measurements did not show any change in response as a function of time for HaDHR-cAuBP-CT construct compared to unmodified HaDHR in 10 mM Tris-Cl, pH=7.5 buffer (Figure 4-5E). This might be due to the protein aggregation on the surface, or more probably due to the metal binding peptides interacting with the protein itself. The metal binding peptides may also be self-interacting via intermolecular disulfide bond formation between cysteine residues, thereby not allowing formation of a productive conformation necessary for binding on the metal surface.

At any concentration of salt, salt ions provide charge or electrical double layer shielding to reduce aggregation and/or protein-protein interactions (77,78). Stoichiometric ion binding on charged proteins also regulates this process (79). Addition of salts at low concentration often reduces protein-protein interactions, thereby reducing aggregation and increasing solubility (80,81). To further optimize the SPR conditions, salts were added to the Tris-buffer system and kinetic experiments were performed (Figure 4-5F). A preliminary K_d value of ~0.4 μM for HaDHR-cAuBP-CT and ~1 μM for unmodified HaDHR construct were obtained via SPR in the presence of 100 mM NaCl. A hyperbolic response curve was observed for both HaDHR-cAuBP-CT and unmodified HaDHR. Comparing the binding isotherms in Figure 4-5D and Figure 4-5F, suggests

that with only Tris-buffer and at concentrations of about >2 μM, the HaDHR-cAuBP-CT proteins are aggregating. This is consistent with the AFM results (Figure 4-6, *vide infra*). We speculate that the addition of salts apparently increased the solubility of HaDHR-cAuBP-CT construct, thereby allowing the proteins to more efficiently interact with the gold surface.

At this juncture of the experimental studies, we were unable to conduct more detailed SPR studies because the system failed, and no funds were available to repair the instrument. While the SPR studies were incomplete and inconclusive, the preliminary binding isotherms of the kinetic experiments with Tris and salt buffer system suggested that HaDHR-cAuBP-CT could preferentially bind to the gold surface. We speculate that at ~1 μM concentration, a detailed SPR study would show enhanced binding of the HaDHR-cAuBP-CT in compared to unmodified HaHDR as a function of time. We further speculate this would be due to decreased protein-protein interactions and less aggregation in the presence of salt.

To further probe the interaction of the cAuBP construct on the gold surface, AFM studies were performed in Tris-buffer (Figure 4-6). While the HaDHR-cAuBP-CT construct showed more individual protein molecules bound to the gold surface, the image also suggested the presence of more aggregates compared to the unmodified HaDHR (Figures 4-6A and 4-6B). The AFM images showed that even though the surface coverage might be different, the binding of the two constructs is not dramatically different which is consistent with the SPR studies.

These observations may result from differences in local charge proximal to the metal binding peptides. This conjecture is further supported by the presence of more aggregates on the gold surface with the HaDHR-cAuBP-CT construct (Figure 4-6B). The SPR and AFM studies, both suggested that the presence of the salts might disrupt these protein-protein interactions and enhance binding of the HaDHR-cAuBP-CT constructs on the gold surface. Additionally, we show

the K_D for the cAuBP constructs were in the μM range which might show binding of these metal affinity peptides on the surface, but it is unlikely to support *in vivo* biosensing applications. While the SPR and AFM studies are admittedly incomplete, concerns regarding the *in vivo* viability of a gold peptide approach became an underlying concern.

A potential drawback of the cAuBP is the reliance on the cysteine residue to facilitate creation of the cyclic peptide and targeting of the gold surface. Sulfhydryl based targeting of a gold surface could reduce *in vivo* longevity when the enzyme system is based on this approach due to release of the gold-sulfur bond. After implantation, in addition to reactive oxygen species, the presence of glutathione, and other oxidative species due to foreign body response could compromise this approach. Platinum binding tags (PtBP) that have been described in the literature (58), offer an alternative to gold surfaces for biosensor fabrication. For the above-mentioned reasons, studies with gold binding peptides were switched to platinum binding peptides.

A distinct advantage of a PtBP approach is that the peptides do not contain a cysteinyl residue and could potentially be less susceptible to oxidative events. The absence of cysteine residues might also allow less propensity for intermolecular interactions in PtBP constructs thereby allowing better binding to the metal surface. Finally, biosensors designed using platinum have shown better biocompatibility than gold surfaces thereby increasing their *in vivo* lifetimes (72).

Binding interactions of the HaDHR-PtBP-CT constructs were studied by using platinum nanoparticles of ~50 nm that were readily available during the course of this project. The availability of these well characterized and well-behaved nanoparticles facilitated the use of DLS to determine if the PtBP tags were binding to a platinum surface. A control protein, NT-3xPtBP-MBP-LOx, has a well characterized DLS signature indicating binding to a platinum nanoparticle with a $K_D > 10^{-12}$. In the presence of 50 nm platinum nanoparticles, NT-3xPtBP-MBP-LOx shows

a ~10 nm shift and an overall Z-average of ~9 nm via DLS (Table 4-2, Figure 4-7A) compared to the unmodified MBP-LOx. These data were consistent with the previous findings that showed unambiguous binding to the platinum nanoparticles. HaDHR-PtBP-CT constructs showed a slight peak shift ~3 nm (Table 4-2, Figures 4-7B and 4-7C), and showed a decrease in the overall Z-average of ~1 nm compared to the unmodified HaDHR. These results suggested that the PtBP tags are preferentially binding to the platinum surface.

The DLS results for the HaDHR proteins were less pronounced as compared to the MBP-LOx control protein. MBP-LOx is tetrameric in solution, which allows the protein to present four metal affinity peptides to the platinum surface. Studies with MBP-LOx has suggested that the four metal affinity peptides can bind to the nanoparticles in potentially two ways. The four metal binding peptides can either bind to one nanoparticle or can bind to two individual nanoparticles by presenting two metal binding peptides to each nanoparticle (Figure 4-9A). These two binding modalities leads to a mixed population observed by DLS-one that is about the same in diameter as the HaDHR protein, and one is significantly longer by virtue of binding to two 50 nm Pt nanoparticles. This combination of populations give rise to a larger peak shift compared to HaDHR. This is also reflected in the larger Z-average for the NT-3xPtBP-MBP-LOx protein.

HaDHR is dimeric in solution, and only presents two metal binding peptides to the platinum surface (Figure 4-9B). Therefore, the DLS signature only shows one binding modality to the 50 nm Pt nanoparticles. This is also reflected in the lower Z-average compared to NT-3xPtBP-MBP-LOx.

DLS showed that the size of MBP-LOx in solution is ~13 nm (Figure 4-7A), which is consistent with other tetrameric proteins. DLS also showed that the size of HaDHR observed in solution is ~8 nm (Figure 4-7B), which is consistent with other dimeric proteins. The choice of a 50 nm

nanoparticle for DLS studies is based on two factors. First, a 50 nm nanoparticle is significantly bigger compared to the proteins. Second, the 50 nm nanoparticle is the smallest nanoparticle that offers a significant amount of surface area. Unlike smaller nanoparticles (Table 4-3), the surface area to volume ratio for 50 nm nanoparticle is small, so the curvature is not very large, and the nanoparticle should be a reasonable approximation of a transduction element. This is known from the previous studies from NT-3xPtBP-MBP-LOx protein (66).

Table 4-3: Relationship of a nanoparticle to nanoparticle surface area and volume

Nanoparticle Diameter (nm)	Nanoparticle Radius (nm)	Surface-Area[A] (nm^2)	Volume[B] (nm^3)	Surface-Area to Volume ratio
10	5	314	524	0.60
20	10	1257	4189	0.30
30	15	2827	14137	0.20
40	20	5027	33510	0.15
50	25	7854	65450	0.12
60	30	11310	113097	0.10
70	35	15394	179594	0.09
80	40	20106	268082	0.08
90	45	25447	381703	0.07
100	50	31416	523598	0.06

[A]Surface area of a sphere is calculated using the formula $4\pi r^2$
[B]Volume of a sphere is calculated using the formula $4/3\pi r^3$

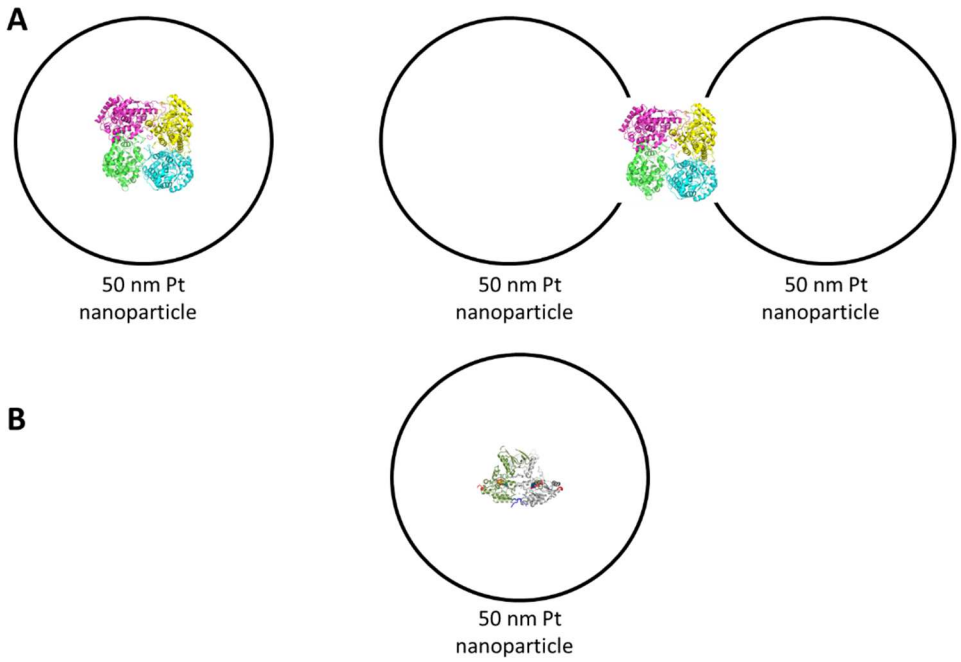

Figure 4-9 Potential binding modes of the Pt binding peptides to nanoparticles
(A) MBP-LOx has two potential binding modes: four metal binding peptides can bind to individual nanoparticles, or two metal binding peptides that interact with one nanoparticle and the other two metal binding peptides interacting with a second nanoparticle. This mixed population is observed by DLS, (B) Cartoon of HaDHR protein showing a single binding modality with Pt nanoparticles.

The cAuBP and PtBP constructs were further probed via QCM. Based on the findings from SPR measurements, surface-binding interaction studies via QCM were performed in 10 mM Tris-Cl, 100 mM NaCl, pH=7.5 buffer system. Only QCM studies on the easier to obtain HaDHR-3xPtBP-CT construct were performed. Both HaDHR-3xPtBP-CT and HaDHR-5xPtBP-CT constructs gave similar results via DLS. As shown in Figure 4-8A, QCM confirmed a better binding interaction of the HaDHR-cAuBP-CT construct as compared to the unmodified HaDHR. These results are consistent with those obtained via SPR, where the best binding isotherm was observed in the presence of 100 mM NaCl. This emphasizes the important role of electrostatics in mediating the binding process. The addition of salts is also likely maintaining the solubility and a low aggregation state of the modified enzymes. Together, these effects allow the cAuBP metal binding peptides to adopt a productive conformation for binding to the gold surface.

Under similar buffer conditions, the HaDHR-3xPtBP-CT construct initially showed what appears to be a metal binding peptide binding event with the platinum surface (Figure 4-8B). The interaction, while specific, also seemed to delaminate over time. The unmodified HaDHR showed a more nonspecific association that curiously showed no delamination over time. PtBP tags are known to bind slowly on a platinum surface (58). A protein engineered with a PtBP tag might show even slower binding to a platinum surface due to protein induced steric and the linker used between the metal binding peptide and the protein. The results suggest that these PtBP tag constructs might need more time to bind on the surface and may require further optimization of buffer conditions. If slow association is relevant, then better binding may be observed by allowing the protein to incubate longer with the platinum surface.

A major difficulty in working with these metal binding peptides is that there is no consensus in understanding how the peptides bind to the surface when tethered with an enzyme. The

effectiveness of a metal binding peptide to associate with a metal surface is a combination of the following enzyme-system attributes: (1) the innate affinity of the peptide to bind to the metal surface of interest, (2) the aggregation state of the enzyme in solution, (3) the proper presentation of the metal binding peptide to the surface when tethered to an enzyme, (4) the absence of association between the peptide and the enzyme, (5) the linker used to connect the metal binding peptide to the enzyme to promote points 3 and 4, and, (6) the ability of the metal binding peptide to freely form the proper conformation for binding to the surface. The proper presentation is no doubt related to the affinity of the unmodified protein for the surface, e.g., the non-specific binding discussed earlier. The above-mentioned attributes are regulated by one or more factors, which together play a profound role in mediating the K_d of the ensemble. This explains why a metal binding peptide successfully employed with one enzyme may not work well with other enzymes, especially those in another family.

The linker that tethers metal binding peptides to an enzyme plays a significant role in regulating the interaction of the peptides with the metal surface. To date, no universal linker has been described, and the most common are four amino acid linkers based on a GGG sequence with either a serine or a proline capping the sequence (Table 4-1). Furthermore, it is unclear how to predict the binding affinities of a metal binding peptide and linker combination, especially for proteins with different aggregation states in solution and for proteins from different families. For example, a single amino acid change in the linker that results in nM affinity for an oxidase enzyme (Table 4-1, entry 3) only results in mM affinity when used with a dehydrogenase enzyme (Table 4-1, entries 1 and 2). This same linker also results in μM binding affinities for other dehydrogenases (Table 4-1, entries 4-7) simply by switching the order of the residues in the linker-e.g., GGGS to

SGGG. Because of the limited number of systems that show productive targeted binding, the design criteria of a well-functioning linker are still unknown.

The conformational requirements of a metal binding peptide are unknown and no high- resolution atomic structure of a peptide on a metal surface has been reported. Also unknown is whether the metal binding peptides need to adopt some form of a secondary structure to bind to a metal surface. Furthermore, if a secondary structure is required for the metal binding peptide, it is unknown if that secondary structure must form prior to binding or is the consequence of the binding event. The formation of secondary structures is almost certainly affected by the peptide's proximity to the enzyme, which in turn is affected by the nature of the linker.

In this study, a six amino acid linker (SSGSSG) for HaDHR-cAuBP-CT construct and a four amino acid linker (SGGG) for HaDHR-3xPtBP-CT construct was used. The apparent K_D observed for both the constructs were in the μM range. It is interesting to consider the differences in interactions of metal binding peptides on different metal surfaces in similar buffer conditions on the same protein (Figure 4-8). While the HaDHR-cAuBP-CT showed significant binding to a gold surface, the HaDHR-PtBP-CT construct showed only an initial specific binding event on a platinum surface followed by delamination over time. This is further evidence that (1) the linker sequence plays a significant role in orienting, directing, and presenting the enzyme tethered metal binding peptides to a metal surface for binding, and (2) the metal binding peptides mediated binding events are multiparametric, and the rules dictating these interactions are still not completely understood.

Platinum binding peptides were used for the first time in this study to direct HaDHR to a platinum binding surface. Preliminary QCM studies showed the successful engineering of HaDHR enzyme with the platinum binding peptides to direct and orient the enzyme on the metal surface. However, further studies are required to optimize this system for *in vivo* applications. The apparent binding

affinity of the platinum binding peptides were still lower as compared to the MBP-LOx protein control, that showed nM binding to a platinum surface. Our preliminary data also suggest that two-point binding may not be sufficient. Engineering of the HaDHR proteins with platinum binding peptides at both the N- and C-termini, or at some other position in the protein, with or without a different linker will be required to increase the binding affinity of the enzyme. These are all prerequisites for the use of metal binding peptides *in vivo* applications.

For an enzyme to be used for *in vivo* biosensing applications, a binding affinity in the nM range is most suitable. A high binding affinity is required to prevent delamination over time. An advantage of using metal binding peptides attached to the surface with higher binding affinities is that there will be less dissociation from abrasion over time, thereby increasing the *in vivo* lifetime of the biosensor. Also, most of the studies done by using these metal binding peptides is on gold, which often has issue of oxidation due to its gold-sulfur bond formation and might not be suitable for *in vivo* applications. To date, no report exists that uses platinum binding peptides to successfully direct an enzyme to a platinum surface that generates a useable amperometric signal for *in vivo* or in any biological medium.

In conclusion, this study investigated the engineering of HaDHR enzymes with metal binding peptides to direct the enzyme to a metal surface in an oriented manner and showed partial proof of concept. This study also highlighted the experimental hurdles to universally use metal binding peptides in biosensor fabrication. The factors that need to be considered include, linker length, buffer conditions, ionic strength of the sensing medium and the orientation of the enzyme on the transduction element. For the purposes of HaDHR and the development of a histamine biosensor, the key question that remains unanswered is whether a metal binding peptide can orient the enzyme to enable direct electron transfer to the electrode surface.

4.6 References

1. Guilbault, G., and Lubrano, G. (1973) An enzyme electrode for the amperometric determination of glucose. *Analytica chimica acta* **64**, 439-455
2. Gričar, E., Kalcher, K., Genorio, B., and Kolar, M. (2021) Highly Sensitive Amperometric Detection of Hydrogen Peroxide in Saliva Based on N-Doped Graphene Nanoribbons and MnO2 Modified Carbon Paste Electrodes. *Sensors* **21**, 8301
3. Zhang, Y., Bai, X., Wang, X., Shiu, K.-K., Zhu, Y., and Jiang, H. (2014) Highly sensitive graphene–Pt nanocomposites amperometric biosensor and its application in living cell H2O2 detection. *Analytical chemistry* **86**, 9459-9465
4. Karatekin, R. S., Kaplan, S., Ozmen, S. I., and Dudukcu, M. K. (2022) N-doped reduced graphene oxide/ZnO/nano-Pt composites for hydrogen peroxide sensing. *Materials Chemistry and Physics* **280**, 125792
5. Ullah, R., Rasheed, M. A., Abbas, S., Rehman, K.-u., Shah, A., Ullah, K., Khan, Y., Bibi, M., Ahmad, M., and Ali, G. (2022) Electrochemical sensing of H2O2 using cobalt oxide modified TiO2 nanotubes. *Current Applied Physics* **38**, 40-48
6. Mandpe, P., Prabhakar, B., Gupta, H., and Shende, P. (2020) Glucose oxidase-based biosensor for glucose detection from biological fluids. *Sensor Review* **40**, 497-511
7. Komkova, M. A., Eliseev, A. A., Poyarkov, A. A., Daboss, E. V., Evdokimov, P. V., Eliseev, A. A., and Karyakin, A. A. (2022) Simultaneous monitoring of sweat lactate content and sweat secretion rate by wearable remote biosensors. *Biosensors and Bioelectronics*, 113970
8. Updike, S. J., and Hicks, G. P. (1967) The enzyme electrode. *Nature* **214**, 986-988
9. Yamaoka, H., and Sode, K. (2007) SPCE based glucose sensor employing novel thermostable glucose dehydrogenase, FADGDH: Blood glucose measurement with 150nL sample in one second. *Journal of Diabetes Science and Technology* **1**, 28-35
10. Sode, K., Loew, N., Ohnishi, Y., Tsuruta, H., Mori, K., Kojima, K., Tsugawa, W., LaBelle, J. T., and Klonoff, D. C. (2017) Novel fungal FAD glucose dehydrogenase derived from Aspergillus niger for glucose enzyme sensor strips. *Biosensors and Bioelectronics* **87**, 305-311
11. Kajiya, Y., Sugai, H., Iwakura, C., and Yoneyama, H. (1991) Glucose sensitivity of polypyrrole films containing immobilized glucose oxidase and hydroquinonesulfonate ions. *Analytical chemistry* **63**, 49-54
12. Cass, A. E., Davis, G., Francis, G. D., Hill, H. A. O., Aston, W. J., Higgins, I. J., Plotkin, E. V., Scott, L. D., and Turner, A. P. (1984) Ferrocene-mediated enzyme electrode for amperometric determination of glucose. *Analytical chemistry* **56**, 667-671
13. Garjonyte, R., Yigzaw, Y., Meskys, R., Malinauskas, A., and Gorton, L. (2001) Prussian Blue-and lactate oxidase-based amperometric biosensor for lactic acid. *Sensors and Actuators B: Chemical* **79**, 33-38
14. Turner, A., Hendry, S., and Cardosi, M. (1987) Tetrathiafulvalene: a new mediator for amperometric biosensors. in *Biosensors, Instrumentation & Processing .* Linköping University Electronic Press The World Biotech Report 1987. pp
15. Chaubey, A., and Malhotra, B. (2002) Mediated biosensors. *Biosensors and bioelectronics* **17**, 441-456

16. Gortan, L., Karan, H., Hale, P., Inagaki, T., Okamoto, Y., and Skotheim, T. (1990) A glucose electrode based on carbon chemically modified with a ferrocene-containing silioxane polymer and glucose oxidase, coated with a poly (ester sulfonic acid) cation exchanger. *Analytica chimica acta* **228**, 23-30
17. Inagaki, T., Lee, H., Skotheim, T., and Okamoto, Y. (1989) Syntheses and electrochemical properties of siloxane polymers containing ferrocene and dimethylferrocene. *Journal of the Chemical Society, Chemical Communications*, 1181-1183
18. Hale, P. D., Inagaki, T., Karan, H. I., Okamoto, Y., and Skotheim, T. A. (1989) A new class of amperometric biosensor incorporating a polymeric electron-transfer mediator. *Journal of the American Chemical Society* **111**, 3482-3484
19. Hatada, M., Loew, N., Inose-Takahashi, Y., Okuda-Shimazaki, J., Tsugawa, W., Mulchandani, A., and Sode, K. (2018) Development of a glucose sensor employing quick and easy modification method with mediator for altering electron acceptor preference. *Bioelectrochemistry* **121**, 185-190
20. Yamashita, Y., Ferri, S., Huynh, M. L., Shimizu, H., Yamaoka, H., and Sode, K. (2013) Direct electron transfer type disposable sensor strip for glucose sensing employing an engineered FAD glucose dehydrogenase. *Enzyme and microbial technology* **52**, 123-128
21. Okuda-Shimazaki, J., Yoshida, H., and Sode, K. (2020) FAD dependent glucose dehydrogenases–Discovery and engineering of representative glucose sensing enzymes. *Bioelectrochemistry* **132**, 107414
22. Zafar, M. N., Beden, N., Leech, D., Sygmund, C., Ludwig, R., and Gorton, L. (2012) Characterization of different FAD-dependent glucose dehydrogenases for possible use in glucose-based biosensors and biofuel cells. *Analytical and bioanalytical chemistry* **402**, 2069-2077
23. Takeda, K., and Nakamura, N. (2021) Direct electron transfer process of pyrroloquinoline quinone–dependent and flavin adenine dinucleotide–dependent dehydrogenases: Fundamentals and applications. *Current Opinion in Electrochemistry* **29**, 100747
24. Yamashita, Y., Lee, I., Loew, N., and Sode, K. (2018) Direct electron transfer (DET) mechanism of FAD dependent dehydrogenase complexes∼ from the elucidation of intra- and inter-molecular electron transfer pathway to the construction of engineered DET enzyme complexes∼. *Current Opinion in Electrochemistry* **12**, 92-100
25. Sode, K., Tsugawa, W., Yamazaki, T., Watanabe, M., Ogasawara, N., and Tanaka, M. (1996) A novel thermostable glucose dehydrogenase varying temperature properties by altering its quaternary structures. *Enzyme and microbial technology* **19**, 82-85
26. Inose, K., Fujikawa, M., Yamazaki, T., Kojima, K., and Sode, K. (2003) Cloning and expression of the gene encoding catalytic subunit of thermostable glucose dehydrogenase from Burkholderia cepacia in Escherichia coli. *Biochimica et Biophysica Acta (BBA)-Proteins and Proteomics* **1645**, 133-138
27. Tsuya, T., Ferri, S., Fujikawa, M., Yamaoka, H., and Sode, K. (2006) Cloning and functional expression of glucose dehydrogenase complex of Burkholderia cepacia in Escherichia coli. *Journal of biotechnology* **123**, 127-136
28. Yoshida, H., Kojima, K., Shiota, M., Yoshimatsu, K., Yamazaki, T., Ferri, S., Tsugawa, W., Kamitori, S., and Sode, K. (2019) X-ray structure of the direct electron transfer-type FAD

glucose dehydrogenase catalytic subunit complexed with a hitchhiker protein. *Acta Crystallographica Section D: Structural Biology* **75**, 841-851
29. Yamaoka, H., Ferri, S., and Sode, M. F. K. (2004) Essential role of the small subunit of thermostable glucose dehydrogenase from Burkholderia cepacia. *Biotechnology letters* **26**, 1757-1761
30. Okuda-Shimazaki, J., Loew, N., Hirose, N., Kojima, K., Mori, K., Tsugawa, W., and Sode, K. (2018) Construction and characterization of flavin adenine dinucleotide glucose dehydrogenase complex harboring a truncated electron transfer subunit. *Electrochimica Acta* **277**, 276-286
31. Algov, I., Grushka, J., Zarivach, R., and Alfonta, L. (2017) Highly efficient flavin–adenine dinucleotide glucose dehydrogenase fused to a minimal cytochrome c domain. *Journal of the American Chemical Society* **139**, 17217-17220
32. Lee, I., Loew, N., Tsugawa, W., Lin, C.-E., Probst, D., La Belle, J. T., and Sode, K. (2018) The electrochemical behavior of a FAD dependent glucose dehydrogenase with direct electron transfer subunit by immobilization on self-assembled monolayers. *Bioelectrochemistry* **121**, 1-6
33. Nakazawa, Y., Yamazaki, T., Tsugawa, W., Ikebukuro, K., and Sode, K. (2003) Amperometric glucose sensor using thermostable co-factor binding glucose dehydrogenase. *IEEJ Transactions on Sensors and Micromachines* **123**, 185-189
34. Sassolas, A., Blum, L. J., and Leca-Bouvier, B. D. (2012) Immobilization strategies to develop enzymatic biosensors. *Biotechnology advances* **30**, 489-511
35. Wink, T., Van Zuilen, S., Bult, A., and Van Bennekom, W. (1997) Self-assembled monolayers for biosensors. *Analyst* **122**, 43R-50R
36. Vericat, C., Vela, M., Benitez, G., Carro, P., and Salvarezza, R. (2010) Self-assembled monolayers of thiols and dithiols on gold: new challenges for a well-known system. *Chemical Society Reviews* **39**, 1805-1834
37. Chen, C., Xie, Q., Yang, D., Xiao, H., Fu, Y., Tan, Y., and Yao, S. (2013) Recent advances in electrochemical glucose biosensors: a review. *Rsc Advances* **3**, 4473-4491
38. Nguyen, H. H., Lee, S. H., Lee, U. J., Fermin, C. D., and Kim, M. (2019) Immobilized enzymes in biosensor applications. *Materials* **12**, 121
39. Sarikaya, M., Tamerler, C., Schwartz, D. T., and Baneyx, F. (2004) Materials assembly and formation using engineered polypeptides. *Annu. Rev. Mater. Res.* **34**, 373-408
40. Yucesoy, D. T., Karaca, B. T., Cetinel, S., Caliskan, H. B., Adali, E., Gul-Karaguler, N., and Tamerler, C. (2015) Direct bioelectrocatalysis at the interfaces by genetically engineered dehydrogenase. *Bioinspired, Biomimetic and Nanobiomaterials* **4**, 79-89
41. Cetinel, S., Caliskan, H. B., Yucesoy, D. T., Donatan, A. S., Yuca, E., Urgen, M., Karaguler, N. G., and Tamerler, C. (2013) Addressable self-immobilization of lactate dehydrogenase across multiple length scales. *Biotechnology journal* **8**, 262-272
42. So, C. R., Hayamizu, Y., Yazici, H., Gresswell, C., Khatayevich, D., Tamerler, C., and Sarikaya, M. (2012) Controlling self-assembly of engineered peptides on graphite by rational mutation. *Acs Nano* **6**, 1648-1656
43. Wu, J., Park, J. P., Dooley, K., Cropek, D. M., West, A. C., and Banta, S. (2011) Rapid development of new protein biosensors utilizing peptides obtained via phage display. *PLoS One* **6**, e24948

44. Lee, Y. S., Baek, S., Lee, H., Reginald, S. S., Kim, Y., Kang, H., Choi, I.-G., and Chang, I. S. (2018) Construction of uniform monolayer-and orientation-tunable enzyme electrode by a synthetic glucose dehydrogenase without electron-transfer subunit via optimized site-specific gold-binding peptide capable of direct electron transfer. *ACS applied materials & interfaces* **10**, 28615-28626
45. Lee, H., Lee, Y. S., Lee, S. K., Baek, S., Choi, I.-G., Jang, J.-H., and Chang, I. S. (2019) Significant enhancement of direct electric communication across enzyme-electrode interface via nano-patterning of synthetic glucose dehydrogenase on spatially tunable gold nanoparticle (AuNP)-modified electrode. *Biosensors and Bioelectronics* **126**, 170-177
46. Lee, H., Lee, Y. S., Reginald, S. S., Baek, S., Lee, E. M., Choi, I.-G., and Chang, I. S. (2020) Biosensing and electrochemical properties of flavin adenine dinucleotide (FAD)-Dependent glucose dehydrogenase (GDH) fused to a gold binding peptide. *Biosensors and Bioelectronics* **165**, 112427
47. Kamathewatta, N. J., Deay III, D. O., Karaca, B. T., Seibold, S., Nguyen, T. M., Tomas, B., Richter, M. L., Berrie, C. L., and Tamerler, C. (2020) Self-immobilized putrescine oxidase biocatalyst system engineered with a metal binding peptide. *Langmuir* **36**, 11908-11917
48. Hwang, L., Chen, C.-L., and Rosi, N. L. (2010) Preparation of 1-D nanoparticle superstructures with tailorable thicknesses using gold-binding peptide conjugates. *Chemical Communications* **47**, 185-187
49. So, C. R., Kulp III, J. L., Oren, E. E., Zareie, H., Tamerler, C., Evans, J. S., and Sarikaya, M. (2009) Molecular recognition and supramolecular self-assembly of a genetically engineered gold binding peptide on Au {111}. *Acs Nano* **3**, 1525-1531
50. Evans, J. S. (2008) "Tuning in" to mollusk shell nacre-and prismatic-associated protein terminal sequences. Implications for biomineralization and the construction of high performance inorganic− organic composites. *Chemical reviews* **108**, 4455-4462
51. Diamanti, S., Elsen, A., Naik, R., and Vaia, R. (2009) Relative functionality of buffer and peptide in gold nanoparticle formation. *The Journal of Physical Chemistry C* **113**, 9993-9997
52. Evans, J. S., Samudrala, R., Walsh, T. R., Oren, E. E., and Tamerler, C. (2008) Molecular design of inorganic-binding polypeptides. *Mrs Bulletin* **33**, 514-518
53. Feng, J., Pandey, R. B., Berry, R. J., Farmer, B. L., Naik, R. R., and Heinz, H. (2011) Adsorption mechanism of single amino acid and surfactant molecules to Au {111} surfaces in aqueous solution: design rules for metal-binding molecules. *Soft Matter* **7**, 2113-2120
54. Skelton, A. A., Liang, T., and Walsh, T. R. (2009) Interplay of sequence, conformation, and binding at the peptide− titania interface as mediated by water. *ACS applied materials & interfaces* **1**, 1482-1491
55. Heinz, H., Jha, K. C., Luettmer-Strathmann, J., Farmer, B. L., and Naik, R. R. (2011) Polarization at metal–biomolecular interfaces in solution. *Journal of the Royal Society Interface* **8**, 220-232
56. Oren, E. E., Notman, R., Kim, I. W., Evans, J. S., Walsh, T. R., Samudrala, R., Tamerler, C., and Sarikaya, M. (2010) Probing the molecular mechanisms of quartz-binding peptides. *Langmuir* **26**, 11003-11009
57. Baneyx, F., and Schwartz, D. T. (2007) Selection and analysis of solid-binding peptides. *Current opinion in biotechnology* **18**, 312-317

58. Seker, U. O. S., Wilson, B., Dincer, S., Kim, I. W., Oren, E. E., Evans, J. S., Tamerler, C., and Sarikaya, M. (2007) Adsorption behavior of linear and cyclic genetically engineered platinum binding peptides. *Langmuir* **23**, 7895-7900
59. Hnilova, M., Oren, E. E., Seker, U. O., Wilson, B. R., Collino, S., Evans, J. S., Tamerler, C., and Sarikaya, M. (2008) Effect of molecular conformations on the adsorption behavior of gold-binding peptides. *Langmuir* **24**, 12440-12445
60. Stols, L., Gu, M., Dieckman, L., Raffen, R., Collart, F. R., and Donnelly, M. I. (2002) A new vector for high-throughput, ligation-independent cloning encoding a tobacco etch virus protease cleavage site. *Protein expression and purification* **25**, 8-15
61. Motulsky, H., and Christopoulos, A. (2004) *Fitting models to biological data using linear and nonlinear regression: a practical guide to curve fitting*, Oxford University Press
62. Seibold, S., A. (2019).
63. Zhou, P., Lugovskoy, A. A., and Wagner, G. (2001) A solubility-enhancement tag (SET) for NMR studies of poorly behaving proteins. *Journal of biomolecular NMR* **20**, 11-14
64. Cheng, Y., and Patel, D. J. (2004) An efficient system for small protein expression and refolding. *Biochemical and biophysical research communications* **317**, 401-405
65. Costa, S., Almeida, A., Castro, A., and Domingues, L. (2014) Fusion tags for protein solubility, purification and immunogenicity in Escherichia coli: the novel Fh8 system. *Frontiers in microbiology* **5**, 63
66. Petillo, P., A. (2021).
67. Wilson, G. S., Chen, X., Matsumoto, N., and Hu, Y. (2004) Method for depositing an enzyme on an electrically conductive substrate. Google Patents
68. Wilson, G. S., Bindra, D. S., Hill, B. S., Thevenot, D. R., Sternberg, R., Reach, G., and Zhang, Y. (1992) Implantable glucose sensor. Google Patents
69. Wilson, G. S., and Gifford, R. (2005) Biosensors for real-time in vivo measurements. *Biosensors and Bioelectronics* **20**, 2388-2403
70. Wilson, G. S., and Hu, Y. (2000) Enzyme-based biosensors for in vivo measurements. *Chemical reviews* **100**, 2693-2704
71. Wilson, G. S., and Johnson, M. A. (2008) In-vivo electrochemistry: what can we learn about living systems? *Chemical reviews* **108**, 2462-2481
72. Gulino, M., Santos, S. D., and Pêgo, A. P. (2021) Biocompatibility of Platinum Nanoparticles in Brain ex vivo Models in Physiological and Pathological Conditions. *Frontiers in Neuroscience* **15**
73. O'Neill, R. D., and Chang, S.-C. (2004) Lowry JP McNeil CJ Biosens. *Bioelectron* **19**, 1521-1528
74. Carter, M. B. (2021) Synthesis of Nanoparticles.
75. Nie, H.-Y., Romanovskaia, E., Romanovski, V., Hedberg, J., and Hedberg, Y. S. (2021) Detection of gold cysteine thiolate complexes on gold nanoparticles with time-of-flight secondary ion mass spectrometry. *Biointerphases* **16**, 021005
76. Petean, I., Tomoaia, G., Horovitz, O., Mocanu, A., and Tomoaia-Cotisel, M. (2008) Cysteine mediated assembly of gold nanoparticles. *J Optoelectron Adv M* **10**, 2289-2292
77. Von Hippel, P., and Schleich, T. (1969) Structure and stability of biological macromolecules. *Marcel Dekker, New York* **2**, 417

78. Staahlberg, J., Joensson, B., and Horvath, C. (1991) Theory for electrostatic interaction chromatography of proteins. *Analytical chemistry* **63**, 1867-1874
79. Boardman, N., and Partridge, S. (1955) Separation of neutral proteins on ion-exchange resins. *Biochemical Journal* **59**, 543
80. Zhang, J. (2012) Protein-protein interactions in salt solutions. in *Protein-protein interactions-computational and experimental tools*. pp 359-376
81. Tsumoto, K., Ejima, D., Senczuk, A. M., Kita, Y., and Arakawa, T. (2007) Effects of salts on protein–surface interactions: applications for column chromatography. *Journal of pharmaceutical sciences* **96**, 1677-1690

Chapter 5. Summary and future directions

Enzyme-based biosensors continue to be the subject of extensive research, with one goal being the increase in the range of analytes that can be used for practical applications. While there are numerous examples of oxidase enzyme-based biosensors (1-3), only a handful of dehydrogenases have been successfully utilized in biosensing applications (4-6). An advantage of engineering dehydrogenases for biosensing applications is their ability to undergo direct electron transfer, which eliminates oxygen dependence. The commercial success of glucose oxidase-based enzyme biosensors for treatment of diabetes, has shown the benefits that continuous real time monitoring of analytes in tissue can provide for the treatment and understanding of disease. An impediment to using dehydrogenases for *in vivo* applications is a lack of understanding of the structure and the mechanism of electron transfer from the active site to the electrode surface. Engineering and characterization of flavin dependent dehydrogenases (FDD) will yield a promising family of proteins for fabricating biosensors. FDDs are amenable to structural studies, protein engineering, and rational design, creating an obvious path forward to a successful biosensor.

This Dissertation focuses on one such FDD enzyme - histamine dehydrogenase from *Rhizobium sp. 4-9* (HaDHR). The focus of this research was to understand the criteria for engineering a dehydrogenase enzyme for use in *in vivo* biosensing applications. The goal was to provide insights and improve upon the current toolbox that is available to the developers of biosensors.

5.1 Structure of *Rhizobium sp. 4-9* Histamine Dehydrogenase and Analysis of the Electron Transfer Pathway to Fc^+

HaDHR is a unique member of a small family of dehydrogenases that contains covalently attached FMN and an Fe_4S_4 as the redox cofactors. HaDHR converts histamine to imidazole acetaldehyde

and ammonia with a release of two electrons and is the only member of this family that does not show substrate inhibition. The absence of substrate inhibition makes this a potential enzyme for fabricating biosensors for *in vivo* applications.

In Chapter 2 the crystal structure of histamine dehydrogenase from gram negative bacteria *Rhizobium sp. 4-9* was solved at a resolution of 2.1 Å. The structure helped to understand the electron transfer pathway from the interior of the protein to the surface. This study identified a surface residue Ala437 that is putatively involved in the transfer of electrons from the Fe_4S_4 cluster to an external artificial mediator ferricenium (Fc^+). A surface serine residue proximal to the Ala437 was identified and the HaDHR was mutated to facilitate attachment of ferrocene (Fc). The attachment of Fc to HaDHR was successful as determined from mass spectrometric analysis. The Fc-tethered HaDHR was shown to be sufficient to support electron transfer from the enzyme to a gold electrode surface. Electrochemical studies with histamine showed a dose-dependent response without the need for any additional artificial mediator in solution.

Based on our findings, we believe that a reasonable set of experiments would include the synthesis of Fc-constructs with either a flexible PEG linker or a short amino acid linker to attach maleimide on one end and the ferrocene on the other (Figure 5-1). Synthesizing Fc-constructs with different linker lengths will allow the ferrocene to diffuse more freely to the electrode surface when tethered to the protein. This Fc-tethered HaDHR might show an increase in current against titration with histamine in the absence of a free mediator in solution. Additionally, when the Fc-tethered HaDHR is immobilized on a surface, the flexible linker might allow the ferrocene to more readily interact with the electrode surface. This might aid to further increase the current and allow for a more efficient electron transfer process between the mediator and the electrode.

We also hypothesize that the Fc-maleimide could be attached to Cys601 in the *wt*-HaDHR. This site is quite distal from the surface residue identified as the exit point of electrons from Fe_4S_4 center, as mentioned in Chapter 2. Solution electrochemical studies in the presence of histamine should also be performed for this construct to see if any change in current is observed. If no change in current is observed, then this will further confirm our findings that the exit point of electrons, from the Fe_4S_4 to the protein surface, is proximal to the Ala437 residue.

Additionally, more detailed mutagenesis studies could be performed to investigate the intramolecular transfer of electrons from the flavin to the Fe_4S_4, and from the Fe_4S_4 to the surface of the protein. This will further aid in elucidating the complete electron transfer pathway in HaDHR and the family members. These studies are expected to help in designing a more robust Gen 3 biosensor for histamine biosensing applications.

An alternative approach in studying the electron transfer pathway in HaDHR would be to utilize quantum-mechanical and semi-classical models and perform theoretical studies to identify the electron transfer pathway in this family of dehydrogenases. In addition, the natural electron acceptor for HaDHR enzyme is still unknown. Based on TMADH studies, it might be useful to see if electron transfer flavoproteins could also act as a natural acceptor for HaDHR enzyme. This would allow us to identify the direct electron transfer from the flavin to the electrode surface which seems to occur in the case of some glucose dehydrogenases (7). Also, other types of cytochromes or heme proteins can be surveyed as a potential electron acceptor for HaDHR Additionally, hitchhiker protein suggested by Sode *et al.* (8) for glucose dehydrogenases could also be surveyed as potential electron acceptors for HaDHR.

Recently, we became aware of the eMap suite of programs that is designed to computationally determine internal electron transfer pathways in proteins (9). The program suggested that the exit

point of electrons to the surface of the protein from the Fe_4S_4 is Trp438. The problem with this analysis is that this Trp is not on the surface but is buried under the surface residue Ala437. More broadly, this computational result reflects the problem with determining electron transfer pathways in proteins, wherein no clear consensus exists as to the best method for such analyses. While mutagenesis studies such as those presented in Chapter 2 can be performed, in the absence of crystal structures of the mutants, it is impossible to assess the effects of a mutation on the overall fold of the protein. More importantly, changes in side-chain orientation and changes in local packing resulting from these mutations, almost certainly effect electron transfer, that could only be accessed with high-resolution crystal structures. The less conservative a mutation the more important that additional crystallographic analysis is needed to understand the overall electron transfer pathway. To date, the prediction of the electron transfer pathway through a protein remains imperfect.

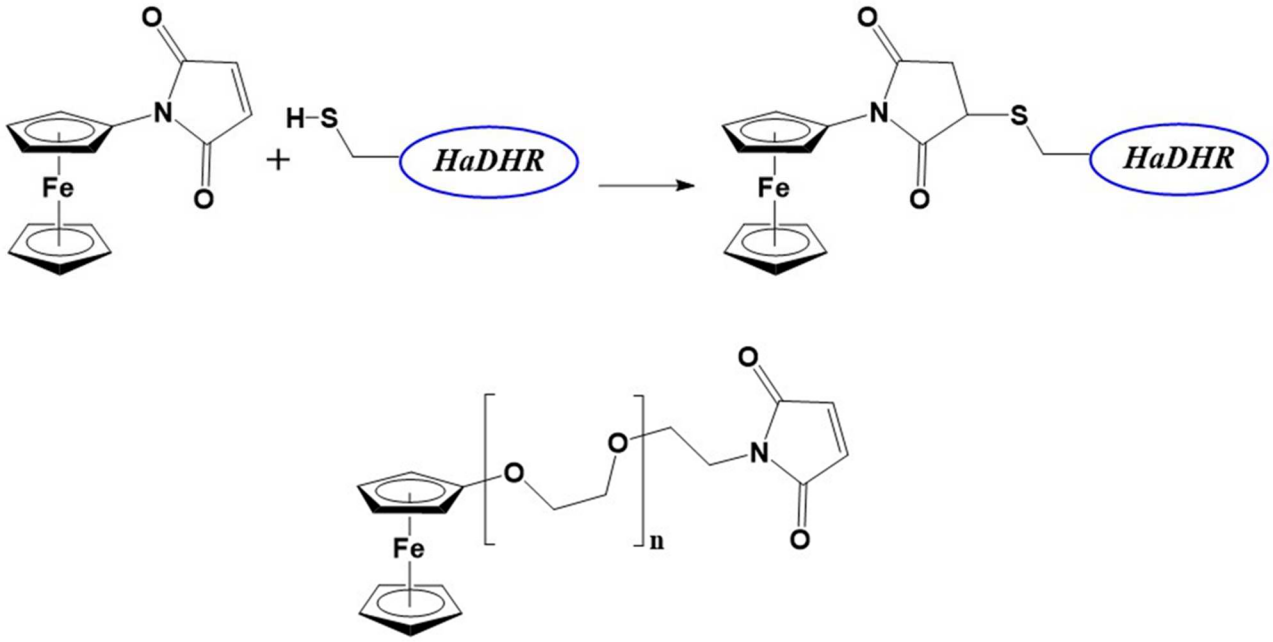

Figure 5-1 Synthetic Fc-construct with a flexible linker
A flexible PEG-linker of different chain lengths can be used to attach ferrocene moiety to a protein using functional maleimide to conjugate to the protein.

5.2 Active Site Residues Critical in Substrate Inhibition of Bacterial Histamine Dehydrogenase

In Chapter 3, the lack of substrate inhibition in HaDHR as compared to other bacterial histamine dehydrogenase, HaDHN, was investigated. These studies were undertaken to understand the substrate inhibition and to establish the structural changes leading to the lack of substrate inhibition in HaDHR. This work provides new insights as to why HaDHR is a superior choice for the use in histamine biosensing applications.

High-resolution crystal structure of HaDHR described in Chapter 2 aided in performing a structural comparison between HaDHR and HaDHN. The structural comparison provided us with the insights that differences in the orientation of an active site residue Phe176 in HaDHR and Tyr181 in HaDHN that might be regulating substrate inhibition in these enzymes. In HaDHN, both the crystal structure and the docking studies with histamine indicated the presence of a hydrogen bond between the hydroxyl of Tyr181 and Asp136. In HaDHR, this hydrogen bond is absent as both positions are occupied by Phe residues (Phe 176 and Phe 131, respectively). In the histamine docking studies of HaDHN, a π-stacking interaction between the tyrosine aromatic ring and the imidazole ring of histamine was observed. This was observed most probably due to the presence of this hydrogen bonding, thereby adopting a conformation unfavorable for catalysis. While in HaDHR, due to the absence of this hydrogen bonding, a more favorable conformation for catalysis is observed. Additionally, our UV-vis studies showed differences in the flavin oxidation state in the presence of histamine in both HaDHR and HaDHN enzyme, suggesting that the geometry of isoalloxazine ring has some bearing on substrate binding and might be involved in the substrate inhibition process.

Our preliminary results on reductive titration of histamine with HaDHR suggested a stochiometry of n=1 for histamine at pH=7.4 whereas for HaDHN the stochiometry with histamine was observed to be n=2 at pH=7.4 (10). Said alternatively, for each HaDHR monomer, the histamine stochiometry is one per catalytic cycle. By contrast, for each HaDHN monomer, the histamine stochiometry is two per catalytic cycle. The histamine titration results obtained for HaDHR were similar to the results observed for HaDHN at pH=9.0, where no substrate inhibition was observed. The histamine titration results suggest that at physiological pH HaDHR and HaDHN show differences in the binding of histamine at the active site which influences the flavin state. For HaDHN, the stabilization of the semiquinone state (peak at 365 nm) and binding of the second substrate to the semiquinone is considered to be responsible for substrate inhibition (11). In HaDHR, the peak at 365 nm is minimal to non-existent as observed in our UV-vis studies. Therefore, our structural comparison studies, along with UV-vis, histamine docking and histamine titration studies suggested that the mode of binding of histamine to the active site for both HaDHR and HaDHN is quite different thereby influencing the absence or presence of substrate inhibition process.

Based on our findings, future studies could include obtaining a substrate bound crystal structure for both HaDHR and HaDHN. For these studies a highly resolved crystal structure is preferred. A high-resolution structure will show the subtle changes in the geometry of the flavin and the Fe_4S_4 cluster in presence of histamine for HaDHR and HaDHN enzymes. The histamine bound crystal structure will also help in understanding the changes in the active site residues around the flavin of both enzymes. This could further verify our findings from the docking and molecular simulation studies highlighted in Chapter 3 and help in understanding the lack of substrate inhibition in HaDHR. Additionally, a more advanced technique like electron paramagnetic resonance

spectroscopy could be performed to study the redox state of FMN for the HaDHR and HaDHN enzyme in the presence of histamine to establish the presence and role of the semiquinone state. This will help us in further understanding the differences in redox state distribution in the flavin in HaDHR and HaDHN in the presence of histamine as was observed in our UV-vis spectroscopic studies.

Kinetic studies using stopped flow techniques could be performed. This study will allow monitoring of the enzymatic reaction in real time with increasing concentrations of histamine. These studies will further provide us with insights of the enzyme-substrate mechanism and its relationship with the oxidation-reduction state of flavin. In addition, a more detailed reductive titration with histamine could be performed for HaDHR as was done with HaDHN (10). This will allow us to investigate the differences in stoichiometry with histamine between the two enzymes and further help us in understanding the histamine-dependence kinetics for HaDHR and HaDHN.

Additionally, UV-vis spectroelectrochemistry could also be performed to determine the redox potentials of the FMN and the Fe_4S_4 cofactor in the presence of histamine. The redox potentials of the Fe_4S_4 cluster could also be calculated using one of the other advanced techniques, such as, EPR spectroelectrochemistry or a combination of UV-vis/EPR-redox titration (12). While measuring the redox potentials for Fe_4S_4 cluster experimentally using above mentioned techniques is complicated, an alternative approach would be to measure the potentials theoretically using density functional theory geometry optimizations or by performing CV measurements using an indium tin oxide electrode as suggested by Kano *et al* (10). These studies will give insights into the redox potential changes of the FMN and Fe_4S_4 in the absence and presence of histamine thereby, helping to further understand the differences in the redox chemistry of the two bacterial histamine dehydrogenases HaDHR and HaDHN. All these studies are expected to aid in our

understanding of the substrate inhibition mechanism in this family of dehydrogenases, thereby further explaining the lack of substrate inhibition in HaDHR.

5.3 Engineering the HaDHR enzyme with gold and platinum metal affinity peptides for controlled orientation to develop a working amperometric biosensor

In Chapter 4, HaDHR was engineered with noble metal affinity peptides to achieve oriented and controlled immobilization on a surface to form a working biosensor. Compared to traditional chemical immobilization methods, noble affinity peptides were used as these have been described previously to orient the enzyme on a metal surface with significant binding affinities. Both gold binding peptides and platinum binding peptides previously described were used for this study. The study successfully showed the binding of both the gold and platinum binding peptides on a metal surface, but the binding affinities were only in the micromolar range. This study also highlighted the importance of ionic strength e.g., the concentration of salts, in regulating the binding, thereby indicating the importance of electrostatic interactions of the metal binding peptides with a metal surface. In addition, the importance of linker sequence in controlling the orientation, presentation, and direction of the enzyme tethered metal binding peptides to a metal surface was also highlighted. The study also showed that the linker sequence plays a profound role in mediating the binding affinity of the ensemble, one protein showing nM binding affinity while with another protein the same linker showed μM/mM binding affinity. The study therefore emphasized that a metal binding peptide successfully employed with one enzyme may not work well with other enzymes. The study performed in Chapter 4 also emphasized that the unmodified protein may have significant, although non-specific, affinity for the electrode surface such that it competes with the metal binding peptides. Note that non-specific binding can and does compete with specific binding mediated by a metal binding peptide. It is therefore desirable to minimize non-specific binding

events to promote metal binding peptide mediated binding. We speculate that by reducing non-specific binding we would be able to reduce some delamination processes, especially those where loss of non-specifically bound protein can promote loss of peptide mediated bound protein.

Based on our current understanding of peptide-mediated surface interaction, a reasonable direction for future studies would be, optimization of the linker sequence for HaDHR so that nM binding affinity could be achieved for the purposes of *in vivo* biosensing applications. In addition to optimizing the linker sequence, one can attach the metal binding peptide to both N- and C-termini or at any point on the protein to increase the binding affinity further by having a multiple attachment point. Multiple attachment points on a metal surface are more advantageous than just a two-point attachment. This was observed in MBP-LOx, a tetrameric enzyme that has a four-point attachment on a metal surface (13). We speculate having more metal binding peptides available for attachment to a metal surface allows the protein to bind tightly with nM to pM affinity and the problem of protein delamination can be avoided. However, it might be possible that all the metal binding peptides available for binding might not bind to the surface efficiently. This might be due to the distance between the metal binding peptides attached to the protein that are available for attachment to a metal surface.

In our QCM studies of the gold metal binding peptides modified HaDHR (Figure 4-8A), we observed a frequency change of ~50 Hz, which corresponds to a mass change of 1363 ng on a metal surface. The sensitivity for the chips were ~27Hz/ng. For platinum metal binding peptides modified HaDHR (Figure 4-8B) an initial frequency change of ~20Hz was observed which may correspond to specific, peptide-mediated binding to a metal surface. This frequency change is similar to that observed for MBP-LOx (Figure 4-8C). The QCM trace also shows a second process after the initial binding event that appears to be non-specific, as the trace at higher frequencies

looks like the control protein. Thus, despite the observation of a peptide-mediated binding event, the system still requires further optimization so that the only modality is the peptide-mediated binding. This is what is observed for MBP-LOx (PtBP) and Put-Ox (cAuBP), where delamination is also not problematic. Delamination is almost certainly due to the weaker binding of the modified HaDHR proteins on a metal surface (~μM range compared to pM binding affinity for MBP-LOx) combined with the propensity of the unmodified HaDHR to bind to a metal surface, thereby forming enzyme aggregates.

The surface area for a gold and platinum QCM wafers are essentially the same. The mass of material on a QCM wafer corresponding to a monolayer of HaDHR is expected to be ~750 ng, where the mass of the water molecules and the ions associated with the protein have not been corrected for. For platinum binding peptides, the initial specific binding corresponds to a mass change of ~545 ng. This value is corresponds to a partial monolayer, further emphasizing the need to further optimize the system. Future experiments related to Figure 4-8B would be to probe the effect of washing the metal surface after binding with buffer to remove any non-specific bound protein. The expectation would be to observe a frequency change that is stabilized at ~20Hz - 30 Hz corresponding to a complete monolayer of enzyme.

Additional studies should be performed using the electrochemical feature of the quartz crystal microbalance system (eQCM) to simultaneously determine the activity of the immobilized enzyme. eQCM studies will also prove important to optimize the attachment of the metal binding peptides to the metal surface to promote direct electron transfer. The optimal point of attachment for high affinity binding may conflict with the orientation of the enzyme for highly efficient direct electron transfer. This could be overcome by rational design approaches where the metal binding peptides could be attached on the protein closer to the exit point of electrons from the Fe_4S_4 center.

Such a study is expected to bring the Fe_4S_4 center closer to the electrode surface to allow for a direct electron transfer. It has been reported earlier that for direct "electron tunneling" to occur the electron transfer must be within 14 Å as the electron transfer rate decreases logarithmically with increasing distance (14-16). These studies will require a combination of computational and experimental methods to rationally design the modified HaDHR construct for an efficient direct electron transfer process.

In addition to the future project studies proposed above there are some programmatic studies, i.e., development of a functioning histamine biosensor, that should also be considered in the future. For example, once the metal binding peptide driven immobilization strategy is optimized with at least nM binding affinity, the *in vitro* electrochemical studies of the modified enzyme system should be performed to measure current for the direct electron transfer process (Gen 3 biosensor). The initial studies should be performed with bovine serum albumin or some well defined protein medium to optimize the experimental process. In addition, biogenic amines that can typically act as interferences need to be tested, i.e., dopamine, serotonin, epinephrine, norepinephrine. If HaDHR has oxidase activity that needs to be determined as well *in vitro*. The stability of the immobilized enzyme on the electrode surface should be tested *in vitro* initially.

Alternatively, the Fc-tethered enzyme system can be immobilized on a transduction element using these metal binding peptides and *in vitro* electrochemical studies can be performed for a quasi-direct electron transfer process (Gen 2.5 biosensor). Additionally, to increase the electrochemical current, the surface area of the electrode can be increased by using nanoparticles which will allow a greater number of protein molecules to bind to the surface. Note, that bridging the nanoparticles can be achieved by levraging a geometry of a protein multimer such that each dimer can bind to a different nanaoparticle.

After developing a successful biosensor design, the stability of the sensor or long-term *in vivo* studies must be established. Ultimately, the response and the long-term stability of these sensors should be tested in biological fluids of animal models. These clinically approved biosensors can be used in the future as a diagnostic tool in humans to aid in the treatment and understanding of various histamine related disorders.

5.4 References

1. Mandpe, P., Prabhakar, B., Gupta, H., and Shende, P. (2020) Glucose oxidase-based biosensor for glucose detection from biological fluids. *Sensor Review* **40**, 497-511
2. Gul, I., Ahmad, M. S., Naqvi, S. S., Hussain, A., Wali, R., Farooqi, A. A., and Ahmed, I. (2017) Polyphenol oxidase (PPO) based biosensors for detection of phenolic compounds: A Review. *Journal of Applied Biology and Biotechnology* **5**, 0-8
3. Cremisini, C., Di Sario, S., Mela, J., Pilloton, R., and Palleschi, G. (1995) Evaluation of the use of free and immobilised acetylcholinesterase for paraoxon detection with an amperometric choline oxidase based biosensor. *Analytica Chimica Acta* **311**, 273-280
4. Scheiblbrandner, S., Csarman, F., and Ludwig, R. (2022) Cellobiose dehydrogenase in biofuel cells. *Current Opinion in Biotechnology* **73**, 205-212
5. Guo, Z., Smutok, O., Johnston, W. A., Ayva, C. E., Walden, P., McWhinney, B., Ungerer, J. P., Melman, A., Katz, E., and Alexandrov, K. (2022) Circular Permutated PQQ-Glucose Dehydrogenase as an Ultrasensitive Electrochemical Biosensor. *Angewandte Chemie International Edition* **61**, e202109005
6. Kyslova, O., and Monko, A. (2022) Substituted benzoic acid amides as the modifiers of the ethanol bioelectrooxidation using NAD+-dependent alcohol dehydrogenase. *Materials Today: Proceedings* **50**, 483-486
7. Adachi, T., Fujii, T., Honda, M., Kitazumi, Y., Shirai, O., and Kano, K. (2020) Direct electron transfer-type bioelectrocatalysis of FAD-dependent glucose dehydrogenase using porous gold electrodes and enzymatically implanted platinum nanoclusters. *Bioelectrochemistry* **133**, 107457
8. Yoshida, H., Kojima, K., Shiota, M., Yoshimatsu, K., Yamazaki, T., Ferri, S., Tsugawa, W., Kamitori, S., and Sode, K. (2019) X-ray structure of the direct electron transfer-type FAD glucose dehydrogenase catalytic subunit complexed with a hitchhiker protein. *Acta Crystallographica Section D: Structural Biology* **75**, 841-851
9. Tazhigulov, R. N., Gayvert, J. R., Wei, M., and Bravaya, K. B. (2019) eMap: a web application for identifying and visualizing electron or hole hopping pathways in proteins. *The Journal of Physical Chemistry B* **123**, 6946-6951
10. Tsutsumi, M., Fujieda, N., Tsujimura, S., Shirai, O., and Kano, K. (2008) Thermodynamic redox properties governing the half-reduction characteristics of histamine dehydrogenase from Nocardioides simplex. *Bioscience, biotechnology, and biochemistry* **72**, 786-796
11. Tsutsumi, M., Tsujimura, S., Shirai, O., and Kano, K. (2010) Stopped flow kinetic studies on reductive half-reaction of histamine dehydrogenase from Nocardioides simplex with histamine. *The Journal of Biochemistry* **148**, 47-54
12. Spangler, N. J., Lindahl, P. A., Bandarian, V., and Ludden, P. W. (1996) Spectroelectrochemical characterization of the metal centers in carbon monoxide dehydrogenase (CODH) and nickel-deficient CODH from Rhodospirillum rubrum. *Journal of Biological Chemistry* **271**, 7973-7977
13. Petillo, P., A. (2021).
14. Page, C. C., Moser, C. C., Chen, X., and Dutton, P. L. (1999) Natural engineering principles of electron tunnelling in biological oxidation–reduction. *Nature* **402**, 47-52

15. Vazquez-Duhalt, R., Aguila, S. A., Arrocha, A. A., and Ayala, M. (2014) QM/MM molecular modeling and Marcus theory in the molecular design of electrodes for enzymatic fuel cells. *ChemElectroChem* **1**, 496-513
16. Yates, N. D., Fascione, M. A., and Parkin, A. (2018) Methodologies for “wiring” redox proteins/enzymes to electrode surfaces. *Chemistry–A European Journal* **24**, 12164-12182